



Partnership for Air Transportation
Noise and Emissions Reduction
An FAA/NASA/Transport Canada-
sponsored Center of Excellence



Vibration and Rattle Mitigation

PARTNER Project 1.6 report

prepared by
Daniel H. Robinson, Robert J. Bernhard, Luc
G. Mongeau

January 2008

VIBRATION AND RATTLE MITIGATION

PARTNER Project 1.6 Report

January 2008

Prepared by:
Daniel Robinson

Robert Bernhard, Luc G. Mongeau
Purdue University

PARTNER Report No.: PARTNER-COE-2008-004

Any opinions, findings, and conclusions or recommendations expressed in this material are of the authors and do not necessarily reflect the views of the FAA, NASA, or Transport Canada.

The Partnership for AiR Transportation Noise and Emissions Reduction — PARTNER — is a leading aviation cooperative research organization, and an FAA/NASA/Transport Canada-sponsored Center of Excellence. PARTNER fosters breakthrough technological, operational, policy, and workforce advances for the betterment of mobility, economy, national security, and the environment. The organization's operational headquarters is at the Massachusetts Institute of Technology.

The Partnership for AiR Transportation Noise and Emissions Reduction
Massachusetts Institute of Technology, 77 Massachusetts Avenue, 37-395
Cambridge, MA 02139 USA
<http://www.partner.aero>
info@partner.aero

PARTNER Project 1.6 Report: Vibration and Rattle Mitigation

Daniel H. Robinson

Dr. Robert J. Bernhard and Dr. Luc G. Mongeau

Purdue University

TABLE OF CONTENTS

	Page
1 INTRODUCTION	3
2 ANALYTICAL RATTLE MODELS	5
2.1 Non-Resonant Rattle Systems.....	5
2.1.a Case 1: Object on a Vibrating Floor	7
2.1.b Case 2: Beam Leaning on the Corner of Vibrating Floor	9
2.1.c Case 3: Beam Leaning on the Corner of Vibrating Wall.....	10
2.1.d Summary of Rattle Thresholds for Non-Resonant Systems	12
2.2 Resonant Rattle Systems.....	12
2.2.a Case 4: Object on a Flexible Floor	15
2.2.b Case 5: Effects of Preload.....	20
2.2.c Case 6: Effects of Preload and Flexible Floor	25
3 EXPERIMENTAL RATTLE STUDY	40
3.1 Objective.....	40
3.2 Test Method	40
3.3 Mobility Analysis of Rattle-Prone Windows.....	43
3.4 Experimental Results	46
3.4.a Swept Sine Excitation.....	48
3.4.b Aircraft Take-Off Excitation.....	53
3.4.c Random Excitation.....	56
4 SUMMARY AND CONCLUSIONS	59
5 LIST OF REFERENCES.....	63
6 APPENDICES	64
6.1 Appendix A: Experimental plots of rattle study	65
6.1.a Plots of Lower East (LE) window	65
6.1.b Plots of Lower West (LW) window.....	78
6.1.c Plots of Upper East (UE) window	91
6.1.d Plots of Upper West (UW) window.....	104
6.2 Appendix B: Measured Window Rattle Thresholds	117

1 INTRODUCTION

High levels of low frequency noise are created by aircraft during take-off and landing. A by-product of low frequency sound incident on a building façade is the excitation of structures within the building into vibrations. Such acoustically-induced structural vibrations may be imperceptible, but they may cause rattle. Rattle is caused by the intermittent loss of contact between two bodies due to vibration [1]. Rattle causes secondary noise emissions, which are often perceived as annoying [2]. Investigation of the mechanisms leading to rattle onset and the development of rattle mitigation strategies are needed to reduce rattle emissions, and the associated annoyance.

Analytical models of idealized systems which have the potential to rattle were developed in this investigation. Comparisons were made between model predictions and results from experiments. From the analytical models, rattle onset thresholds were determined for simple models of various household components such as: window systems, wall hangings, door latches and bric-a-brac. The analytical rattle onset models provide guidelines for design to mitigate rattle.

The analytical models are lumped-parameter, single-degree-of-freedom models of elements typically found in homes. The models are divided into two classes: resonant and non-resonant systems. Previous research conducted by others [3]-[8] have used non-resonant models to describe rattle. These models describe some practical systems. However, many systems rattle because of resonant properties. It is assumed that the response of multi-degree-of-freedom systems may be modeled as a superposition of single-degree-of-freedom systems. This investigation will focus only on single degree of freedom systems. Rattle criterion are developed for various excitation sources including harmonic base motion and forced excitation. These criteria include the rattle onset threshold and the rattle bandwidth, which is a feature of resonant systems.

An *in-situ* experiment was conducted at the Ray W. Herrick Laboratories. Four windows known to be susceptible to rattle were excited via high-fidelity playback of three high-amplitude, low-frequency noise signals. The signals included pre-recorded aircraft take-off noise, a swept sine signal, and random noise. The vibration and acoustic response of each of the windows was measured to determine the relationship between frequency and acceleration level for onset of rattle and qualitatively validate the behavior predicted by the analytical models.

2 ANALYTICAL RATTLE MODELS

Six simple models were developed which include cases with and without preload. Rattle criteria were developed for various excitation mechanisms, including harmonic base motion and harmonic forced excitation. For harmonic base motion, the rattle onset threshold was established in terms of base acceleration magnitude. For an acoustically forced excitation, the rattle onset threshold was expressed in terms of the incident sound pressure amplitude. The criteria considered included the rattle onset threshold and the rattle bandwidth, the latter being a feature that is unique to resonant systems.

To determine rattle onset, the linear Newtonian equations of motion are solved to find the condition where the contact force between the rattle object and the vibrating base becomes zero at an extrema of harmonic excitation. When the contact force becomes zero, contact will be lost between the rattling object and the vibrating base for a short period of time. For excitation amplitudes in excess of the rattle onset threshold loss of contact will occur for a greater time. The repeated re-establishment of contact is the cause for rattle noise. Rattle duration, intensity, or motion was not investigated; these phenomena involve the use of non-linear models. The prediction of the first loss of contact using a linear model was deemed indicative of repeated loss of contact, and thus of the rattle onset threshold.

2.1 *Non-Resonant Rattle Systems*

Schematics of the non-resonant rattle systems are shown in Table 2.1. Three non-resonant models, Cases 1 through 3, were considered. Each involves one rigid body in contact with a vibrating base. Case 1 is an idealization of an object lying on a vibrating floor or shelf. Case 1 is similar to Hubbard's normal excitation model [1]. The excitation is assumed to be in

the direction normal to the base of the rigid object. Cases 2 and 3 describe objects leaning against a wall. Cases 2 and 3 are similar to the models of Carden/Mayes [6] and Sutherland [47-48] for objects that lean at an angle against a vibrating surface. For Case 2, the rattling system is excited vertically through the base, while in Case 3, the rattling system is excited horizontally through the wall.

For each case the rattle onset threshold was defined as the acceleration amplitude, A_b , at which contact was lost between the mass and the vibrating surface.

Table 2.1: Non-resonant rattle systems.

Case	Description <i>Example</i>	Schematic
1	Object on a vibrating floor <i>Alarm clock, lamp, decorative element,...</i>	
2	Beam leaning on corner of vibrating floor <i>Picture frame, bric-a-brac,...</i>	
3	Beam leaning on corner of vibrating wall <i>Picture frame, bric-a-brac,...</i>	

2.1.a Case 1: Object on a Vibrating Floor

For Case 1, an object rests on a vibrating surface with normal contact. This single-degree-of-freedom model can represent any rigid object (i.e. lamp, radio, decorative element, etc.) resting on a vibrating table, shelf, or floor which moves with vertical motion. The system is modeled as a mass resting on a massless, moving base, as shown in Figure 2.1. Base motion excitation was considered.

The magnitude of the base acceleration is A_b . When the mass and the plate move together with the same velocity, there is no rattle. For the no-rattle condition, the contact force between the mass and plate is positive. The system rattles when there is a loss of contact between the mass and the floor, which occurs initially when the contact force becomes zero. The rattle onset thresholds are determined by finding the condition for which the contact force becomes zero.

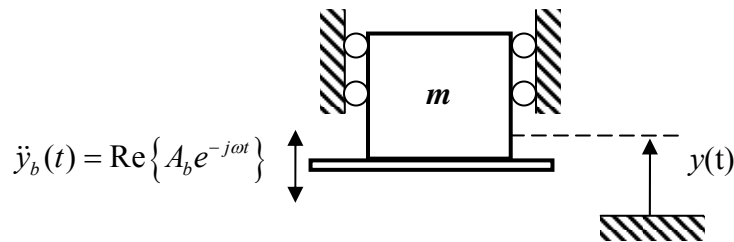


Figure 2.1: Schematic of the model for Case 1. Lumped mass resting on a harmonically excited base.

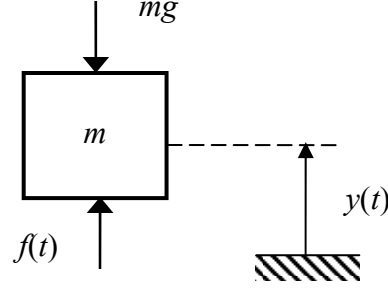


Figure 2.2: Free-body-diagram of the model for Case 1. Lumped mass resting on a harmonically excited base.

The equation of motion for the system in terms of the mass, m , the contact force, f , and the gravitational acceleration, g , is:

$$m\ddot{y}(t) = f(t) - mg, \quad (2.1)$$

where $\ddot{y}_b(t)$ is the base acceleration and $\ddot{y}(t)$ is the mass acceleration. For the case where there is no rattle, the mass displacement is equal to the plate displacement, $y_b = y$. The simple harmonic excitation is denoted by acceleration $\ddot{y}_b(t) = \text{Re}\{A_b e^{-j\omega t}\}$. The solution for the contact force is:

$$f(t) = m\left(g + \text{Re}\{A_b e^{-j\omega t}\}\right). \quad (2.2)$$

The contact force is always be positive when $A_b < g$. The condition for rattle onset can be expressed as

$$A_b > g. \quad (2.3)$$

The system rattles when the magnitude of base acceleration is larger than the gravitational acceleration, g . Note that rattle onset in this case is independent of frequency. To mitigate rattle, the base excitation must be decreased.

2.1.b Case 2: Beam Leaning on the Corner of Vibrating Floor

Case 2 represents a picture or bric-a-brac leaning against a wall with the base undergoing vertical vibration. Case 2 is modeled as a rigid beam leaning on the corner of a vibrating floor as shown in Figure 2.3. It is assumed that there is no slip between the beam and the vertical wall, and that the wall and floor move as a rigid body. The free body diagram of the beam is shown in Figure 2.4.

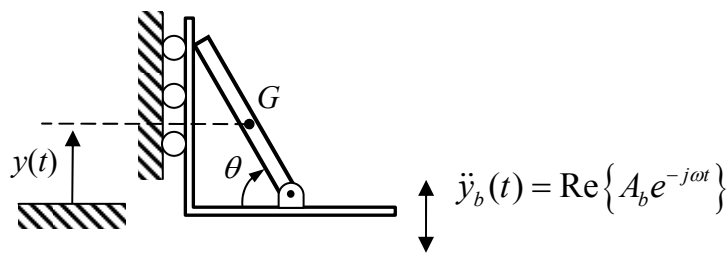


Figure 2.3: Schematic of model for Case 2, beam pinned at one end and resting against a vertically moving base.

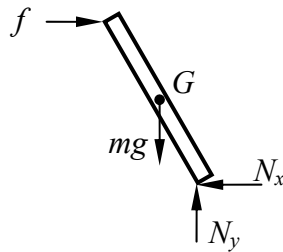


Figure 2.4: Free-body-diagram of model for Case 2.

From the free-body-diagram of the beam of length L shown in Figure 2.4 with no rotation or slip to the right, the equations of motion are:

$$\sum M_G = f \left(\frac{L}{2} \right) \sin \theta + N_x \left(\frac{L}{2} \right) \sin \theta - N_y \left(\frac{L}{2} \right) \cos \theta = 0, \quad (2.4)$$

$$\sum F_x = f - N_x = 0, \quad (2.5)$$

$$\sum F_y = N_y - mg = m\ddot{y}_G. \quad (2.6)$$

The vertical acceleration of the object when rattle does not occur is

$$\ddot{y}_G = \text{Re}\{A_b e^{-j\omega t}\}. \quad (2.7)$$

From equation (2.6) and (2.7),

$$N_y = m\left(g + \text{Re}\{A_b e^{-j\omega t}\}\right). \quad (2.8)$$

After substitution of equation (2.4) into (2.5),

$$2f \sin \theta - N_y \cos \theta = 0, \quad (2.9)$$

where,

$$N_y = 2f \frac{\sin \theta}{\cos \theta} = 2f \tan \theta. \quad (2.10)$$

From equation (2.8), the following equation is obtained,

$$f(t) = \frac{m\left(g + \text{Re}\{A_b e^{-j\omega t}\}\right)}{2 \tan \theta}. \quad (2.11)$$

The contact force is always positive for $A_b < g$. Thus, rattle will occur when:

$$A_b > g. \quad (2.12)$$

The rattle onset threshold is independent of frequency and angle, θ . To mitigate rattle, the magnitude of the base excitation must be decreased.

2.1.c Case 3: Beam Leaning on the Corner of Vibrating Wall

Case 3 is similar to Case 2. However, for case 3 the system is vibrating in the horizontal direction as shown in Figure 2.5.

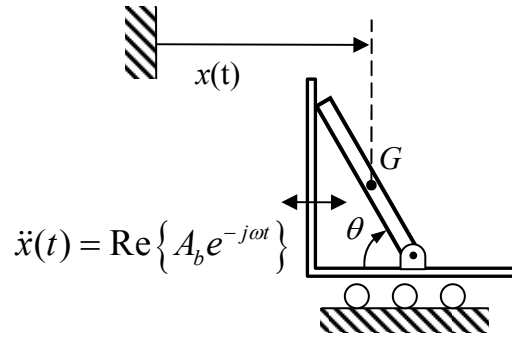


Figure 2.5: Schematic of model for Case 3, beam pinned at one end and resting against a horizontally moving base.

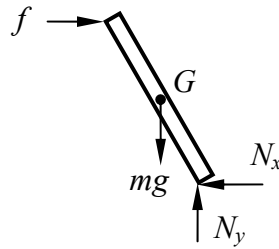


Figure 2.6: Free body diagram of model for Case 3.

The equations of motions are derived from the free-body-diagram of the object of length L shown in Figure 2.6. As with Case 2 there is no rotation or slip at the contact between the base and beam.

$$\sum M_f = LN_x \sin \theta + \left(\frac{L}{2}\right) mg \cos \theta - LN_y \cos \theta = 0, \quad (2.13)$$

$$\sum F_x = f - N_x = m\ddot{x}_G, \quad (2.14)$$

$$\sum F_y = N_y - mg = 0. \quad (2.15)$$

The horizontal acceleration of the object when rattle does not occur is

$$\ddot{x}_G = \text{Re}\{A_b e^{-j\omega t}\}. \quad (2.16)$$

Substitution of equation (2.15) into (2.13) yields:

$$N_x = \frac{mg}{2 \tan \theta}. \quad (2.17)$$

From equation (2.14), (2.16) and (2.17),

$$f(t) = m \left(\operatorname{Re} \{ A_b e^{-j\omega t} \} + \frac{g}{2 \tan \theta} \right). \quad (2.18)$$

Thus, rattle occurs when:

$$A_b > \frac{g}{2 \tan \theta}. \quad (2.19)$$

For increasing θ , less base excitation, A_b , is needed to cause rattle. Therefore, to mitigate rattle, the angle with respect to the floor should be minimized.

2.1.d Summary of Rattle Thresholds for Non-Resonant Systems

Hubbard predicted that an object resting on a vibrating floor rattles when the floor acceleration amplitudes exceeded gravity [3]. Case 1 illustrates this behavior. However, from experimental data Hubbard noticed that rattle can occur for acceleration amplitudes less than gravity. Resonant rattle systems may explain this behavior. In both the Clevenson [5] and the Carden/Mayes studies [6], it was found that the rattle onset threshold is inversely proportional to the angle of the leaning object. The analysis of Case 3 supports this conclusion for horizontal excitation of the base. However, if the base is excited vertically, the lean angle does not affect the rattle onset threshold, as shown in equation (2.12).

2.2 Resonant Rattle Systems

The resonant rattle system models are extensions of the non-resonant system models, accounting for the added effects of stiffness, damping and preload. Resonant systems are frequency dependent. The rattle onset threshold is related to both the base excitation amplitude

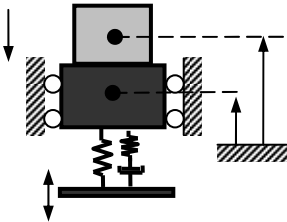
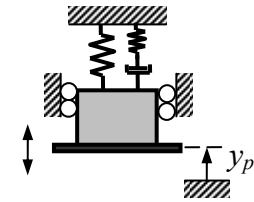
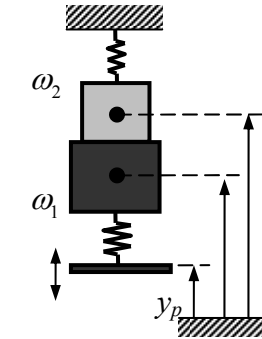
and frequency. Dissipative elements were treated as structural damping with complex stiffness, $k(1+j\gamma)$, where γ is the structural damping coefficient. Structural damping coefficients for typical solid structures (wood, glass, metal, etc...) are small (γ ranges from 0.0001 to 0.03).

A steady-state harmonic base acceleration excitation of amplitude, A_b , was considered for Case 4, and a harmonic base displacement excitation of amplitude, Y_b , was considered for Cases 5 and 6. The motion of the system was assumed to respond linearly as long as the contact force is positive. Rattle onset thresholds were determined analytically by solving for the conditions for which the contact force, f , between the two objects first goes to zero, $f \rightarrow 0$. It was assumed that this condition occurs at a peak acceleration condition. Expressions for the complex contact force coefficient were obtained in terms of complex displacement amplitudes. The complex coefficients were restated into a time factor of the form $e^{-j(\omega t - \phi)}$. The real part of this term oscillates between 1 and -1. Rattle onset thresholds were derived for steady-state motion by making the complex time factor equal to 1 or -1. The results were verified by performing time-marching simulations of the contact force for each resonant system to validate that the rattle thresholds established by this procedure occur as expected for transient conditions.

For the time-marching simulations, the Runge-Kutta method was used to numerically approximate the ordinary differential equations that describe the contact force equation. For a given set of mass, stiffness, and damping parameters, the response was calculated for a range of excitation amplitudes and frequencies above and below the predicted rattle onset threshold. The time-marching simulations were evaluated at extremes of typical parameter values. The values of the parameters were selected to bound the range of typical properties of housing components. Natural frequency, ω_n , values of 0.001 rad/s and 100 rad/s were evaluated, representing the bounds of mass and stiffness combinations for mass values of 0.001 kg and 100 kg; and stiffness values of 0.01 N/m and 1000 N/m. Structural damping, γ , was evaluated for values of 0.0001 and 0.1. Preload was a parameter for Case 5 and 6 resonant rattle systems. The preload values evaluated for these systems was $y_{p,min}$ and $y_{p,min}+10$, where $y_{p,min}$ is the minimum preload required to maintain contact between two objects at rest. The excitation acceleration amplitude, A_b , was evaluated for three values; 0 m/s², 1 m/s², and 10 m/s² for Case 4. The excitation displacement amplitude, Y_b , was evaluated for three values; 0 m, 0.001 m, and 0.01 m for Cases 5 and 6. The time-marching simulation were evaluated at five excitation frequency, ω , values;

$0.1\omega_n$, $0.9\omega_n$, ω_n , $1.1\omega_n$, and $10\omega_n$. The time marching simulations were evaluated for a combination of all selected parameter values for each of the three resonant rattle systems. A total of 41 time-marching simulations were evaluated for Case 4 and 81 simulations each for Cases 5 and 6. It was found that the contact force for each of the simulations first went to zero near the instant of peak amplitude motion. While in principle this may not always be the case, the simulations demonstrated that for the small damping values considered, the rattle onset thresholds could accurately be determined from steady-state solutions and that rattle first occurs when $e^{-j(\omega t - \phi)} = \pm 1$. The time-marching simulations also showed that the excitation amplitude necessary to cause the loss of contact was identical to the amplitude predicted by analytical derivation. Schematics of the three resonant rattle systems are shown in Table 2.2.

Table 2.2: Resonant rattle systems.

Case	Description <i>Example</i>	Schematic
4	Object on a flexible floor <i>vibration through the floor from the foundation or floor joists</i>	
5	Effects of pre-load <i>lighting fixtures or door latches which are held against a surface by a spring</i>	
6	Effects of pre-load & flexible floor <i>window system with pre-loaded gaskets or a door in a door frame</i>	

2.2.a Case 4: Object on a Flexible Floor

Case 4 is a modification of Case 1. It represents an object resting freely on a flexible floor, such as a block resting on a floor board between joists or bric-a-brac resting on a flexible shelf. For this case, the inertial force due to gravity, g , holds the object in contact with the base. The flexible floor is modeled as a mass-spring-damper system with masses, m_1 and m_2 , and

complex stiffness, $k(1 + j\gamma)$, where γ is the structural damping coefficient. The rattling object is modeled as a single lumped mass, m_2 resting on m_1 .

2.2.a.i Case 4: Base Motion Excitation – Normal Damping Levels

For a harmonic base excitation, $\ddot{y}_b = \text{Re}\{A_b e^{-j\omega t}\}$, rattle onset occurs when the contact force between the floor and the object is zero. The schematic and free body diagram for Case 4 are shown in Figure 2.7 and Figure 2.8, respectively.

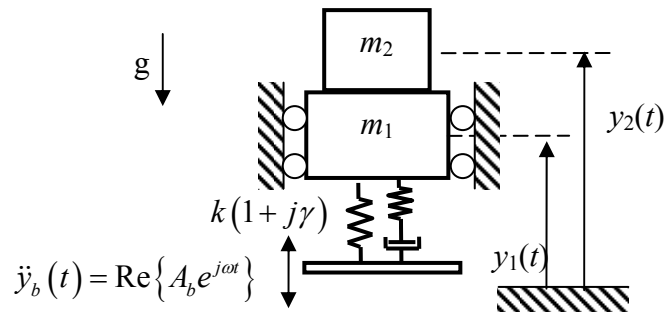


Figure 2.7: Schematic of the model for Case 4, lumped mass resting on a harmonically excited flexible floor.

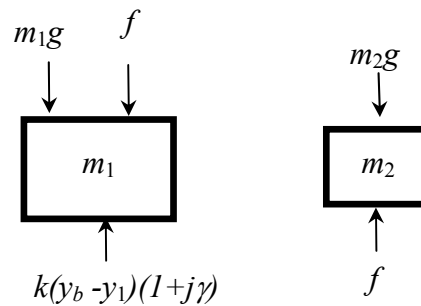


Figure 2.8: Free body diagram of elements in Case 4.

The steady-state harmonic motion of the masses m_1 and m_2 is described in the complex notation form using $\ddot{y}_1(t) = \text{Re}\{A_1 e^{-j\omega t}\}$, $y_1(t) = -\frac{1}{\omega^2} \text{Re}\{A_1 e^{-j\omega t}\}$, $\ddot{y}_2(t) = \text{Re}\{A_2 e^{-j\omega t}\}$ and $y_2(t) = -\frac{1}{\omega^2} \text{Re}\{A_2 e^{-j\omega t}\}$. The motion of the vibrating base is described by $\ddot{y}_b(t) = \text{Re}\{A_b e^{-j\omega t}\}$ and $y_b(t) = -\frac{1}{\omega^2} \text{Re}\{A_b e^{-j\omega t}\}$. The equations of motion are:

$$\text{Re}\left\{\left[m_1 - \frac{k}{\omega^2}(1 + j\gamma)\right]A_1 e^{-j\omega t}\right\} = \text{Re}\left\{-\frac{k}{\omega^2}(1 + j\gamma)A_b e^{-j\omega t}\right\} + ky_o - f(t) - m_1 g, \quad (2.20)$$

$$m_2 \text{Re}\{A_2 e^{j\omega t}\} = f(t) - m_2 g, \quad (2.21)$$

where $f(t)$ is the contact force between masses. Here, y_o is the static displacement of the suspended system induced by the weight,

$$y_o = Mg/k = g/\omega_n^2, \quad (2.22)$$

where $M = m_1 + m_2$, and $\omega_n = \sqrt{k/M}$ is the natural frequency of the system. For motion when rattle does not occur, the masses move together with the same acceleration (i.e., $A_1 = A_2 = A$) and the contact force is positive. The solution for $A_1 = A_2 = A$, is:

$$A(j\omega) = \frac{A_b(1 + j\gamma)}{\left[1 - (\omega/\omega_n)^2 + j\gamma\right]}. \quad (2.23)$$

or,

$$A(\omega) = A_b \left\{ \frac{1 + \gamma^2}{\left[1 - (\omega/\omega_n)^2\right]^2 + \gamma^2} \right\}^{1/2} \text{Re}\{e^{-j\phi}\}, \quad (2.24)$$

where ϕ is the phase angle of the response with respect to the force. The acceleration of the masses is

$$\ddot{y}(t) = A_b \left\{ \frac{1 + \gamma^2}{\left[1 - (\omega/\omega_n)^2\right]^2 + \gamma^2} \right\}^{1/2} \text{Re}\{e^{-j(\omega t + \phi)}\}. \quad (2.25)$$

Substitution of equation (2.25) into (2.21) yields, for contact force, $f(t)$

$$\begin{aligned} f(t) &= m_2 (g + \ddot{y}(t)) \\ &= m_2 \left(g + A_b \left\{ \frac{1 + \gamma^2}{\left[1 - (\omega/\omega_n)^2 \right]^2 + \gamma^2} \right\}^{1/2} \operatorname{Re} \left\{ e^{-j(\omega t + \phi)} \right\} \right). \end{aligned} \quad (2.26)$$

Rattle onset occurs when the contact force becomes zero ($f = 0$), which will occur at peak acceleration amplitudes when $e^{-j(\omega t + \phi)} = -1$. Thus,

$$0 = 1 - \frac{A_b}{g} \left\{ \frac{1 + \gamma^2}{\left[1 - (\omega/\omega_n)^2 \right]^2 + \gamma^2} \right\}^{1/2}. \quad (2.27)$$

Solving equation (2.27) in terms of (ω/ω_n) , rattle occurs in a frequency band defined by,

$$\sqrt{1 - \sqrt{(A_b/g)^2 (1 + \gamma^2) - \gamma^2}} < (\omega/\omega_n) < \sqrt{1 + \sqrt{(A_b/g)^2 (1 + \gamma^2) - \gamma^2}}. \quad (2.28)$$

For Case 4, rattle occurs in a band around the natural frequency of the system, which will be referred to as the rattle band. A non-dimensional rattle band parameter, λ , is defined such that $\lambda = \Delta\omega/\omega_n = (\omega_U - \omega_L)/\omega_n$, where ω_U and ω_L are the upper and lower rattle onset thresholds, respectively. The lower rattle threshold, ω_L , must be greater than 0 Hz. For a larger non-dimensional rattle bandwidth, rattle occurs over a broader range of frequencies. Thus, one design objective would be to keep the rattle bandwidth as small as possible.

The rattle bandwidth dependence on base excitation, A_b , and structural damping, γ , is shown in Figure 2.9. The contour labels indicate the magnitude of the rattle bandwidth, λ . The influence of damping is not significant until the structural damping factor is greater than approximately 0.1. Thus for typical structures the effects of damping are negligible for rattle onset. For cases where damping is negligible, equation (2.28) can be rewritten as:

$$\sqrt{1 - A_b/g} < (\omega/\omega_n) < \sqrt{1 + A_b/g}. \quad (2.29)$$

For configurations for which Case 4 is a reasonable model, the only strategy to minimize the rattle bandwidth is by keeping the magnitude of the excitation small.

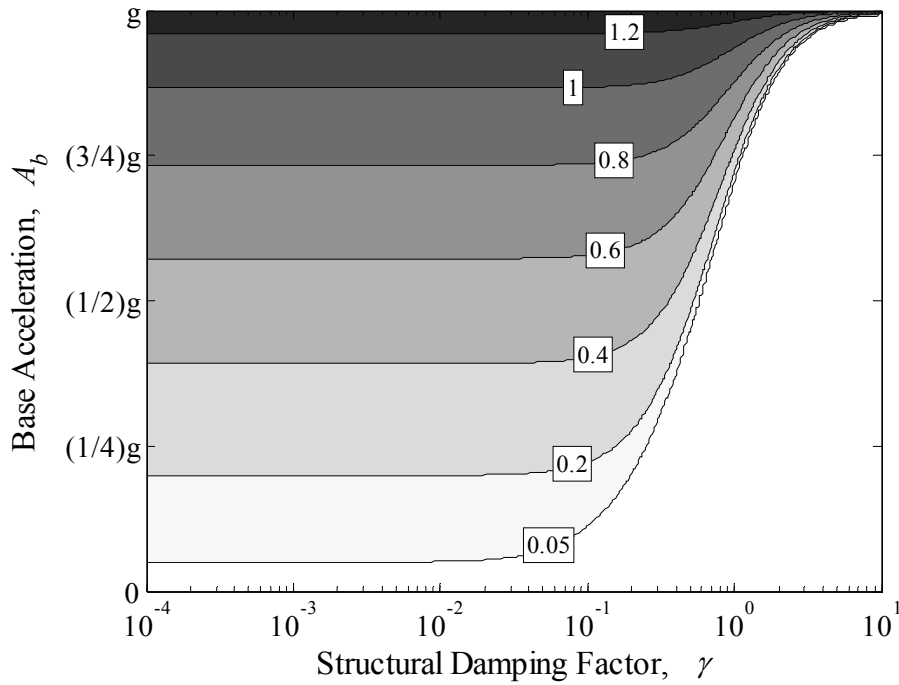


Figure 2.9: Contours of equal non-dimensional rattle bandwidth, λ , (vs. structural damping factor, γ , and base acceleration, A_b).

2.2.a.ii Case 4: Base Motion Excitation – High Damping Levels

It is of interest to determine how much damping would be necessary to prevent rattle. When the rattle bandwidth, $\lambda = (\omega_U - \omega_L)/\omega_n$, is zero, the system does not rattle for any excitation amplitude. From Figure 2.9, damping does reduce the rattle band for values of structural damping greater than 0.1, ($\gamma > 0.1$). The rattle bandwidth is zero for

$$\gamma = \left\{ \left(g/A_b \right)^2 - 1 \right\}^{-1/2}. \quad (2.30)$$

The amount of damping necessary to prevent rattle for a given ratio of excitation acceleration to gravity is determined from equation (2.30). The damping necessary to prevent rattle is shown versus the ratio of gravity and acceleration excitation amplitude in Figure 2.10. Typical materials could prevent rattle for acceleration excitation amplitudes less than 3/100th of gravity. For $A_b = 0.1g$ to $0.5g$ a large amount of damping is necessary to prevent rattle. The

structural damping factor must be on the order of 0.1 to 0.5. Thus, rattle may be prevented by the increase of damping coefficients through the addition of damping elements such as rubber grommets or seal. As the acceleration ratio, A_b/g , approaches unity, ($A_b \sim g$) rattle cannot be prevented.

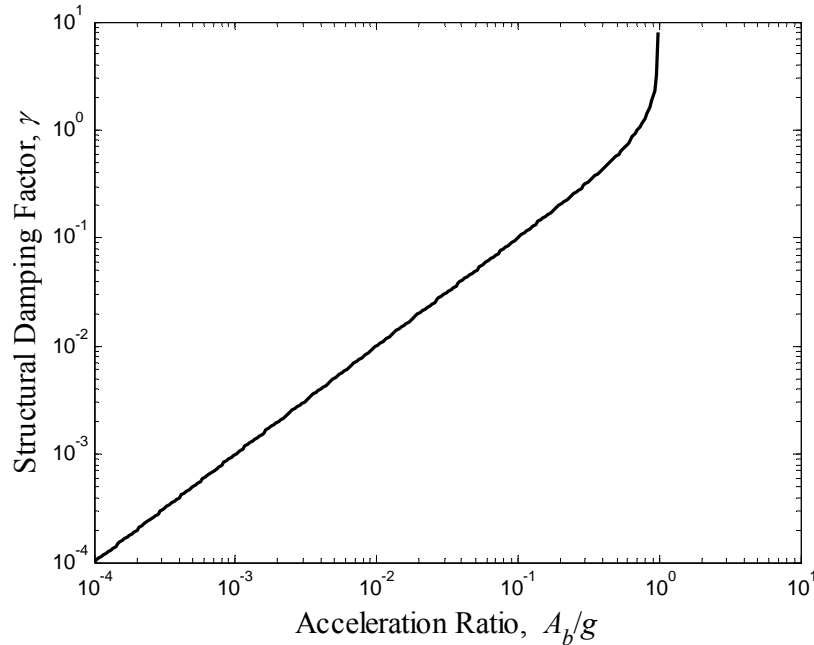


Figure 2.10: Structural damping required to prevent rattle for various base excitation acceleration and gravity ratios.

2.2.b Case 5: Effects of Preload

Case 5 represents a system consisting of flexible objects, such as lighting fixtures or door latches, held in contact with a vibrating surface by a spring. A schematic and a free body diagram for this case are shown in Figure 2.11 and Figure 2.12, respectively. Two possible orientations, vertical and horizontal, were considered. A relationship for rattle onset was derived for the vertical case. The rattle onset threshold for the corresponding horizontal system was achieved by letting the gravitational acceleration, g , equal to zero.

2.2.b.i Case 5: Base Motion Excitation

For a harmonic base excitation, $y_b = \text{Re}\{Y_b e^{-j\omega t}\}$, rattle onset occurs when the contact force between the object and the base is zero.

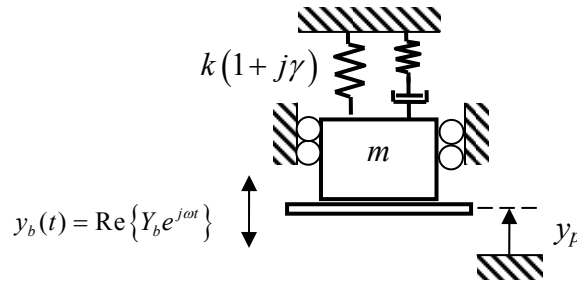


Figure 2.11: Schematic of the model for Case 5, flexible system pre-loaded against a vibrating base.

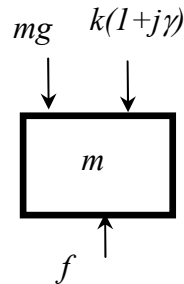


Figure 2.12: Free body diagram of the elements for Case 4.

The system is initially compressed from equilibrium by a static displacement, y_p , referred to here as the static compressive displacement. The motion of the mass, m , is described in complex notation as $y(t) = \text{Re}\{Y e^{-j\omega t}\}$ and $\ddot{y}(t) = -\omega^2 \text{Re}\{Y e^{-j\omega t}\}$. The motion of the vibrating base is described by $y_b(t) = \text{Re}\{Y_b e^{-j\omega t}\}$ and $\ddot{y}_b(t) = -\omega^2 \text{Re}\{Y_b e^{-j\omega t}\}$. For the condition where rattle does not occur, the mass is in direct contact with the base, the contact force between the

base and the mass is positive and the motion of the mass is the same as the motion of the vibrating base; i.e., $y(t) = y_b(t) = \text{Re}\{Y_b e^{-j\omega t}\}$. Because the mass is in direct contact with the base the phase angle between the motion of the mass and the base is zero for positive contact forces. The equation of motion for harmonic excitation of the flexible object is

$$\text{Re}\left\{\left[k(1+j\gamma)-\omega^2 m\right]Y_b e^{-j\omega t}\right\} = f(t) - ky_p - mg. \quad (2.31)$$

Thus the contact force is,

$$\begin{aligned} f(t) &= \text{Re}\left\{\left[k(1+j\gamma)-\omega^2 m\right]Y_b e^{-j\omega t}\right\} + ky_p + mg \\ &= kY_b \left\{\left[1 - (\omega/\omega_n)^2\right]^2 + \gamma^2\right\}^{1/2} \text{Re}\{e^{-j\omega t}\} + ky_p + mg. \end{aligned} \quad (2.32)$$

For static loading, an initial pre-load, $y_{p,\min}$, is required for the base to remain in contact with the mass when at rest. The minimum preload displacement, $y_{p,\min}$, is determined by setting the contact force to zero, ($f = 0$) for static loading, ($\omega = 0$) and by ignoring damping. Thus,

$$y_{p,\min} = -(Y_b + mg/k) = -(Y_b + g/\omega_n^2). \quad (2.33)$$

For systems with multiple modes, the stiffness and mass would be used to determine $y_{p,\min}$.

If the mass and base are not in contact when the system is at rest, $y_p < y_{p,\min}$, two scenarios exist; the system will either always rattle or never rattle. The system will always rattle, independent of frequency, when the motion of the vibrating base is larger than the spatial distance between the mass and base. The system will never be in contact, and hence never rattle, when the motion of the vibrating base is smaller than the spatial distance between the mass and base. Neither scenario is of significant interest.

Similar to Case 4, solving equation (2.32) for the contact force, f , equal to zero,

$$0 = -kY_b \left\{\left[1 - (\omega/\omega_n)^2\right]^2 + \gamma^2\right\}^{1/2} + ky_p + mg, \quad (2.34)$$

This equation can be rearranged as,

$$0 = -\left\{ \left[1 - (\omega/\omega_n)^2 \right]^2 + \gamma^2 \right\}^{1/2} + (y_p - y_{p,\min})/Y_b - 1. \quad (2.35)$$

Solving for (ω/ω_n) from equation (2.35), the range of frequencies over which **no** rattle occurs is:

$$\sqrt{1 - \sqrt{\left((y_p - y_{p,\min})/Y_b - 1 \right)^2 - \gamma^2}} < \left(\frac{\omega}{\omega_n} \right) < \sqrt{1 + \sqrt{\left((y_p - y_{p,\min})/Y_b - 1 \right)^2 - \gamma^2}}. \quad (2.36)$$

This is effectively a non-rattle band, unlike Case 4. For $y_p > y_{p,\min}$ the lower rattle onset threshold will never be greater than 0 Hz. Thus the lower threshold is extraneous. The threshold for rattle onset becomes a one-sided rattle onset threshold.

$$\left(\frac{\omega}{\omega_n} \right) > \sqrt{1 + \sqrt{\left((y_p - y_{p,\min})/Y_b - 1 \right)^2 - \gamma^2}}. \quad (2.37)$$

A few observations are noteworthy. Rattle occurs for all frequencies greater than the rattle onset threshold in equation (2.37). The threshold is always greater than the natural frequency of the system. Increasing preload, y_p , or decreasing base displacement increases the frequency at which rattle onset occurs. Rattle can be mitigated by increasing the rattle onset threshold above the operating range of the system by increasing the preload or decreasing base motion.

Four undamped ($\gamma = 0$) systems conforming to the Case 5 model with natural frequencies of 10, 25, 40, and 80 (rad/s) respectively were investigated. Contours of equal normalized onset frequency for varying base displacement amplitude and static compression ratio are shown in Figure 2.13. This should be read differently than Figure 2.9 for which the equal contours of rattle bandwidth are shown. For the graph in Figure 2.13 rattle will occur at the contour value multiplied by ω_n for the selected condition. For example, a system with natural frequency $\omega_n = 10$ rad/s with static compressive displacement ratio, $(y_p - y_{p,\min})/y_{p,\min} = 1$, and base excitation, $Y_b = 10$ mm will rattle at a threshold frequency of approximately $3\omega_n$. For a constant base displacement magnitude and static compression displacement ratio, the rattle onset threshold is decreased by increasing the natural frequency. Thus systems with higher natural frequencies are more susceptible to rattle.

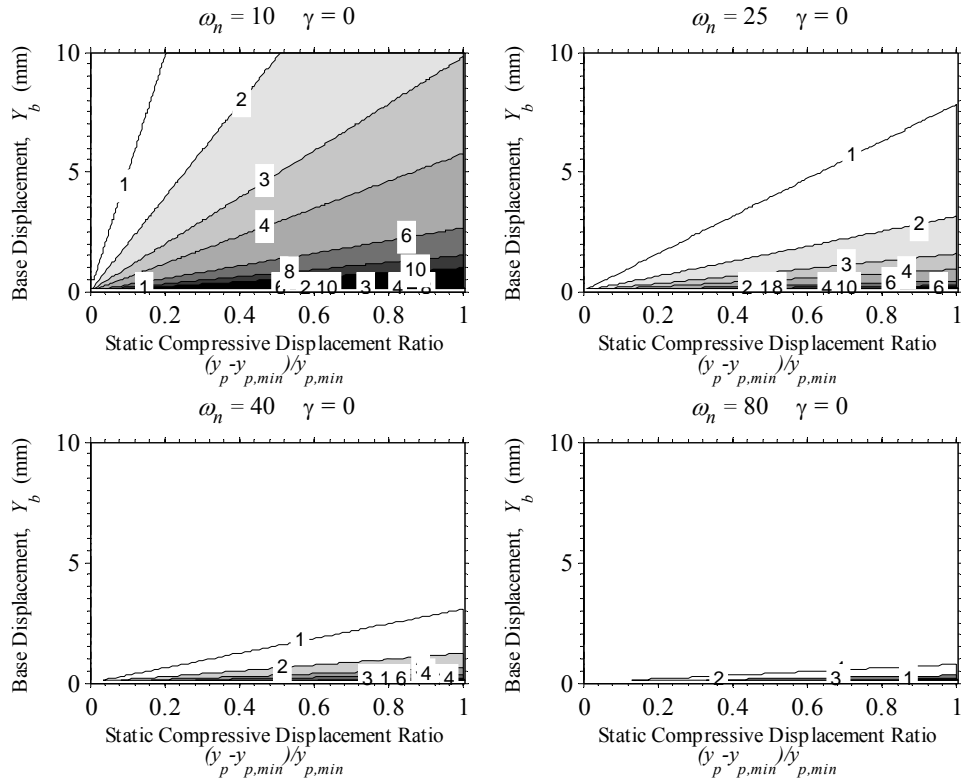


Figure 2.13: Normalized frequency necessary to cause rattle for Case 5 (static compressive displacement ratio vs. base displacement excitation magnitude), $\gamma=0$.

As with Case 4, it is important to consider whether damping is important. The same four systems were investigated using a large structural damping factor, $\gamma = 0.05$. The results were found to be identical. Thus damping has a negligible effect on the rattle onset threshold. Damping is not an effective mitigation strategy, as with Case 4, unless very high levels of damping can be introduced. Rattle can be minimized by shifting the rattle onset threshold to higher frequencies which is achieved by increasing the preload, decreasing the excitation amplitude, or decreasing the natural frequency of the system. Rattle may be eliminated by shifting the rattle threshold above the range of frequencies of excitation.

2.2.c Case 6: Effects of Preload and Flexible Floor

Case 6 was designed to investigate the influence of both preload (Case 5) and a flexible floor (Case 4). This model represents a flexible system with applied preload such as a window system with a gasket or a door in a door frame with a gasket. Two orientations of this rattle system were considered, horizontal (without gravity) and vertical (with gravity). The flexible surface was modeled as having mass, m_1 , with complex stiffness, $k_1(I+j\gamma_1)$, where γ_1 is the structural damping coefficient. The flexible rattle object, which is preloaded, was modeled as having mass, m_2 with complex stiffness, $k_2(I+j\gamma_2)$, where γ_2 is the structural damping coefficient. When the object, m_2 , and the flexible floor, m_1 , move together with the same velocity, there is no rattle.

2.2.c.i Case 6: Static Force and Minimum Preload

The static contact force between the masses and the minimum preload is required for solving the equations of motion for the flexible components in the Case 6 rattle model. For the static case, the velocity of the flexible components is zero and damping effects are insignificant. The schematic and free body diagram for the static case of Case 6 is shown in Figure 2.14 and Figure 2.15, respectively. The effect of preload was included by enforcing the static displacement, y_p . The system was initially compressed from equilibrium by a static compressive displacement, y_p .

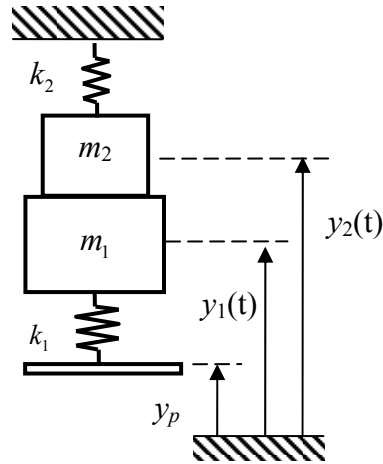


Figure 2.14: Schematic of model for static Case 6.

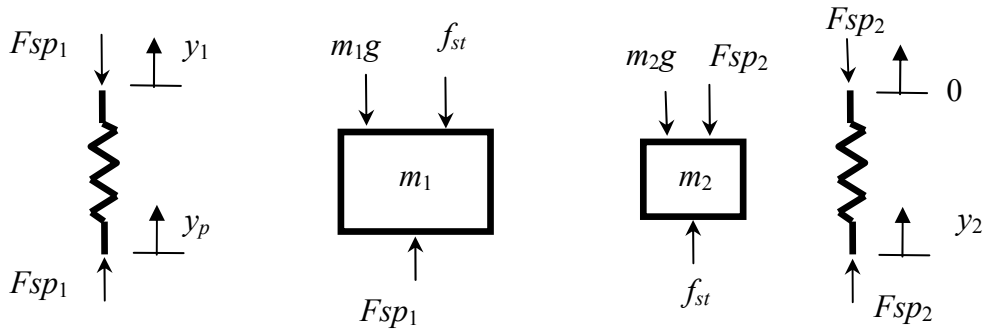


Figure 2.15: Free body diagram of the elements for Case 6.

The same argument that, $y_p > y_{p,\min}$, for Case 5 requires that the static contact force, f_{st} , between the two flexible components must be positive ($f_{st} > 0$) when the system is at rest. The equation of motion for the two flexible components is,

$$f_{st} = F_{sp1} - m_1 g = k_1 (y_p - y_1) - m_1 g, \quad (2.38)$$

$$f_{st} = F_{sp2} + m_2 g = k_2 y_2 + m_2 g. \quad (2.39)$$

The assumption that the masses are in contact when the system is at rest ($f_{st} > 0$), results in the following constraint equation:

$$y = y_1 = y_2. \quad (2.40)$$

By multiplying equation (2.38) by k_2 and equation (2.39) by k_1 then substituting the constraint equation (2.40) in for y , the static force is

$$(k_1 + k_2) f_{st} = k_1 k_2 y_p + (k_1 m_2 - k_2 m_1) g. \quad (2.41)$$

The natural frequency of the total system is $\omega_n = \sqrt{K/M}$, where $K = k_1 + k_2$, $M = m_1 + m_2$, the natural frequency of the lower flexible component is $\omega_1 = \sqrt{k_1/m_1}$, and the natural frequency of the upper flexible component is $\omega_2 = \sqrt{k_2/m_2}$. The system is initially compressed from equilibrium by the static displacement, y_p .

The contact force, $f_{st,vert}$, at the static equilibrium for a vertical system is:

$$\begin{aligned} f_{st,vert} &= \frac{k_1 k_2 y_p + (k_1 m_2 - k_2 m_1) g}{k_1 + k_2} \\ &= (k_1 k_2 / K) \left[y_p + (1/\omega_2^2 - 1/\omega_1^2) g \right]. \end{aligned} \quad (2.42)$$

The minimum amount of preload for which the flexible systems will remain in contact when the system is at rest is, $y_{p,min}$. The minimum preload, $y_{p,min}$, is determined by setting equation (2.42) to zero and solving for y_p . Thus, $y_{p,min} = (1/\omega_1^2 - 1/\omega_2^2) g$. Therefore equation (2.42) simplifies to

$$f_{st,vert} = (k_1 k_2 / K) (y_p - y_{p,min}). \quad (2.43)$$

For a horizontal system, the contact force, $f_{st,horz}$, at static equilibrium is:

$$f_{st,horz} = \frac{k_1 k_2}{K} y_p. \quad (2.44)$$

For the horizontal orientation $y_{p,min} = 0$.

2.2.c.ii Case 6: Undamped Base Motion Excitation

Case 6 was solved first for the undamped system because of mathematical simplicity. The undamped version provides an intuitive understanding of the rattle onset thresholds. The schematic and free-body-diagram for undamped Case 6 are shown in Figure 2.16 and Figure 2.17, respectively. The damped version of Case 6 will be derived in the next section.

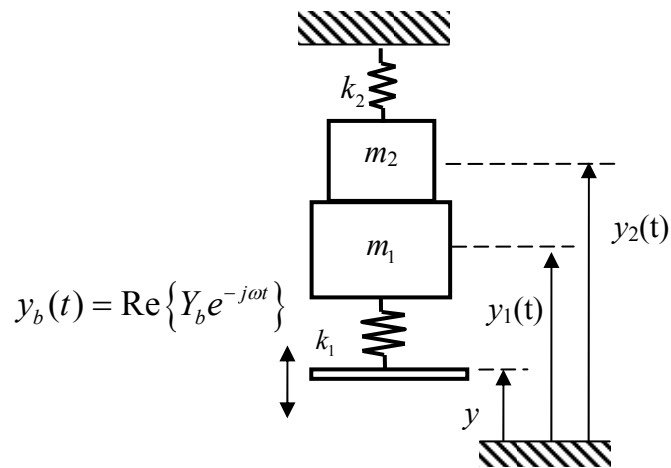


Figure 2.16: Schematic of model for undamped Case 6, flexible system pre-loaded against a vibrating flexible base.

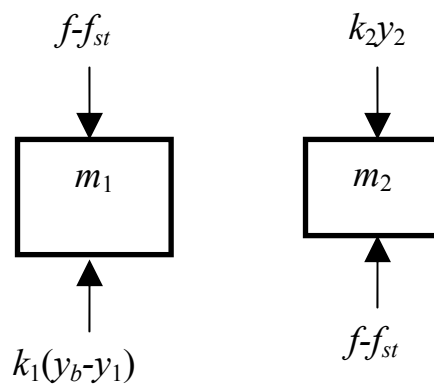


Figure 2.17: Free body diagram for undamped Case 6.

By using Newton's 2nd law of motion, the equations of motion were expressed as,

$$m_1 \ddot{y}_1 + k_1 y_1 = k_1 y_b - f + f_{st}, \quad (2.45)$$

$$m_2 \ddot{y}_2 + k_2 y_2 = f - f_{st}, \quad (2.46)$$

where y_b is the base excitation, f is the contact force between the flexible components, and f_{st} is the static contact force in the system. For the case when rattle does not occur, the masses move together with the same motion (i.e., $y_1 = y_2$) and the contact force is positive. The motion of the masses moving together, M , is described in complex notation using, $y(t) = Y \operatorname{Re}\{e^{-j\omega t}\}$ and $\ddot{y}(t) = -\omega^2 Y \operatorname{Re}\{e^{-j\omega t}\}$. The motion of the vibrating base is described by $y_b(t) = Y_b \operatorname{Re}\{e^{-j\omega t}\}$. For motion when rattle does not occur, the masses move together with the same displacement (i.e., $Y_1 = Y_2 = Y$) and the contact force is positive. The solution for the case where $y = y_1 = y_2$, is obtained from equations (2.45) and (2.46):

$$y(t) = \frac{k_1 Y_b / K}{1 - (\omega / \omega_n)^2} \operatorname{Re}\{e^{-j\omega t}\}. \quad (2.47)$$

Substituting equation (2.47) into (2.46) and solving for the contact force yield,

$$f(t) = \left(\frac{k_1 k_2 Y_b}{K} \right) \frac{1 - (\omega / \omega_2)^2}{1 - (\omega / \omega_n)^2} \operatorname{Re}\{e^{-j\omega t}\} + f_{st}, \quad (2.48)$$

where f_{st} is the static contact force. The first term on the right hand side of (2.48) is the dynamic contact force.

The spring is initially compressed from equilibrium by a displacement y_p . The requirement that $y_p > y_{p,\min}$ ensures that the system is in contact with the base when the system is at rest. Rattle onset occurs when the contact force becomes zero ($f = 0$), which is assumed to occur at peak acceleration amplitudes when $e^{j\omega t} = -1$. The rattle band for the vertical system is solved in terms of (ω / ω_n) from equation (2.48) and (2.42):

For $\omega_1 > \omega_n > \omega_2$ where system 1 is either stiffer or has less mass than system 2:

$$\sqrt{\frac{y_p - y_{p,\min} + Y_b}{y_p - y_{p,\min} + (\omega_n / \omega_2)^2 Y_b}} < \left(\frac{\omega}{\omega_n} \right) < \sqrt{\frac{y_p - y_{p,\min} - Y_b}{y_p - y_{p,\min} - (\omega_n / \omega_2)^2 Y_b}}. \quad (2.49)$$

For $\omega_1 < \omega_n < \omega_2$ where system 1 is more flexible or has more mass than system 2:

$$\sqrt{\frac{y_p - y_{p,\min} - Y_b}{y_p - y_{p,\min} - (\omega_n/\omega_2)^2 Y_b}} < \left(\frac{\omega}{\omega_n}\right) < \sqrt{\frac{y_p - y_{p,\min} + Y_b}{y_p - y_{p,\min} + (\omega_n/\omega_2)^2 Y_b}}. \quad (2.50)$$

2.2.c.iii Case 6: Damped Base Motion Excitation

Case 6 with damping was investigated to account for structurally dissipative elements. The schematic and free body diagram for the damped Case 6 are shown in Figure 2.18 and Figure 2.19, respectively.

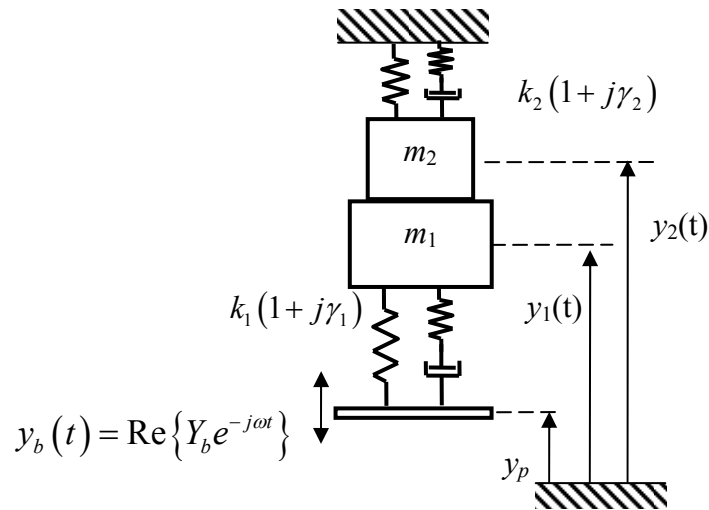


Figure 2.18: Schematic of model for damped Case 6, flexible system pre-loaded against a vibrating flexible base.

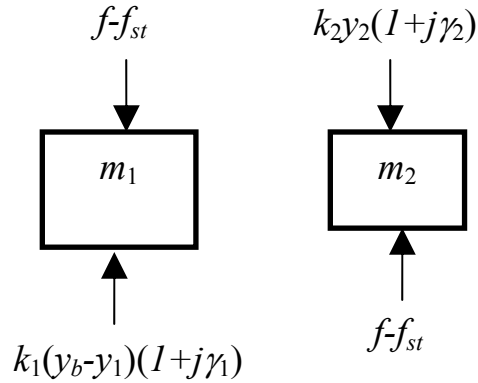


Figure 2.19: Free body diagram for Case 6, including damping.

The equations of motion for harmonic excitation of Case 6 with damping is,

$$\operatorname{Re}\left\{\left[k_1(1+j\gamma_1)-\omega^2m_1\right]Y_1e^{-j\omega t}\right\}=\operatorname{Re}\left\{k_1(1+j\gamma_1)Y_b e^{-j\omega t}\right\}-f+f_{st}, \quad (2.51)$$

$$\operatorname{Re}\left\{\left[k_2(1+j\gamma_2)-\omega^2m_2\right]Y_2e^{-j\omega t}\right\}=f-f_{st}. \quad (2.52)$$

Following the same approach as for previous cases.

$$\left[K+j(k_1\gamma_1+k_2\gamma_2)-\omega^2M\right]Y=k_1Y_b(1+j\gamma_1), \quad (2.53)$$

Therefore,

$$\begin{aligned} Y(j\omega) &= \frac{k_1Y_b(1+j\gamma_1)}{\left[K-\omega^2M+j(k_1\gamma_1+k_2\gamma_2)\right]} \\ &= \left(\frac{k_1Y_b}{K}\right) \left\{ \frac{1+\gamma_1^2}{\left[1-(\omega/\omega_n)^2\right]^2 + \left[(k_1\gamma_1+k_2\gamma_2)/K\right]^2} \right\}^{1/2} e^{-j\phi}. \end{aligned} \quad (2.54)$$

Substituting equation (2.54) into (2.52) and solving for the total contact force, f , yields,

$$f(t) = f_{st} + Y_b \left(\frac{k_1k_2}{K}\right) \left\{ \frac{(1+\gamma_1^2)\left[\left[1-(\omega/\omega_n)^2\right]^2 + \gamma_2^2\right]}{\left[1-(\omega/\omega_n)^2\right]^2 + \left[(k_1\gamma_1+k_2\gamma_2)/K\right]^2} \right\}^{1/2} \operatorname{Re}\left\{e^{-j(\omega t+\phi)}\right\}. \quad (2.55)$$

The spring is initially compressed from equilibrium by displacement y_p and is introduced through the static contact force, f_{st} , term. As discussed in the previous section it is required that $y_p > y_{p,\min}$. This ensures that the system is in contact with the base when the system is at rest. Rattle onset occurs when the contact force becomes zero ($f = 0$), which is assumed to occur at peak acceleration amplitudes when $e^{-j(\omega t + \phi)} = -1$. Solving for rattle onset for the vertical orientation by substituting equation (2.43) for the static contact force,

$$0 = \left(\frac{k_1 k_2}{K}\right)(y_p - y_{p,\min}) - Y_b \left(\frac{k_1 k_2}{K}\right) \left\{ \frac{(1 + \gamma_1^2) \left[\left[1 - (\omega/\omega_2)^2 \right]^2 + \gamma_2^2 \right]}{\left[1 - (\omega/\omega_n)^2 \right]^2 + \left[(k_1 \gamma_1 + k_2 \gamma_2)/K \right]^2} \right\}^{1/2}, \quad (2.56)$$

this can be rearranged as:

$$0 = \left[1 - (\omega/\omega_n)^2 \right]^2 + \left[(k_1 \gamma_1 + k_2 \gamma_2)/K \right]^2 + \left(\frac{Y_b}{y_p - y_{p,\min}} \right)^2 (1 + \gamma_1^2) \left[\left[1 - (\omega/\omega_2)^2 \right]^2 + \gamma_2^2 \right]. \quad (2.57)$$

By rearranging equation (2.57) in the following manner, where $\mu = (\omega/\omega_n)^2$

$$A\mu^2 + B\mu + C = 0, \quad (2.58)$$

where,

$$A = \left[1 + \left(\frac{\omega_n}{\omega_2} \right)^4 \left(\frac{Y_b}{y_p - y_{p,\min}} \right)^2 (1 + \gamma_1^2) \right] \quad (2.59)$$

$$B = -2 \left[1 + \left(\frac{\omega_n}{\omega_2} \right)^2 \left(\frac{Y_b}{y_p - y_{p,\min}} \right)^2 (1 + \gamma_1^2) \right] \quad (2.60)$$

$$C = \left[1 + \left(\frac{k_1 \gamma_1 + k_2 \gamma_2}{K} \right)^2 + \left(\frac{Y_b}{y_p - y_{p,\min}} \right)^2 (1 + \gamma_1^2)(1 + \gamma_2^2) \right] \quad (2.61)$$

The solution to the quadratic equation for equation (2.58) for the rattle onset threshold for normalized frequency is,

$$\left(\frac{\omega}{\omega_n}\right)^2 = \mu_{1,2} = \frac{-B \pm \sqrt{B^2 - 4AC}}{2A}. \quad (2.62)$$

Thus the upper and lower rattle onset thresholds are,

$$\left(\frac{\omega}{\omega_n}\right)_{U,L} = \sqrt{\frac{|B| \pm \sqrt{B^2 - 4AC}}{2A}}, \quad (2.63)$$

such that $\omega_L < \omega_U$ and the lower rattle threshold, ω_L , must be greater than 0 Hz. The rattle band relationships will be left in this form and illustrated using parameter studies.

In Figure 2.20, the contours of rattle bandwidth, λ , are shown for various ratios of natural frequencies, $\omega_R = (\omega_1/\omega_2)$, where the natural frequency of the lower flexible component is $\omega_1 = \sqrt{k_1/m_1}$, and the natural frequency of the upper flexible component is $\omega_2 = \sqrt{k_2/m_2}$. The ratio, $\omega_R = (\omega_1/\omega_2)$, decreases across and down the subplot rows. Each of the eight systems are evaluated with no damping, ($\gamma_1 = \gamma_2 = 0$). Several general observations may be made from Figure 2.20. By increasing the preload the rattle band is reduced for constant excitation. As the ratio of component natural frequencies, ω_R , approaches unity the rattle bandwidth, λ , approaches unity. When $\omega_R = 1$ rattle onset occurs for all preload and excitation amplitudes. For $\omega_1 \ll \omega_2$ and also $\omega_1 \gg \omega_2$ rattle bandwidth is decreased for constant preload and excitation amplitude.

From these observations several rattle mitigation strategies are evident. Increasing preload decreases the rattle band. In practical systems it is unlikely that $\omega_1 = \omega_2 = \omega_n$ exactly. However, for flexible components of similar stiffness and mass, $\omega_1 \rightarrow \omega_2$. Thus the effect of preload is diminished and rattle onset occurs for all preload and excitation amplitudes. Thus, the mitigation strategy is to either stiffen or soften one of the flexible components involved in the rattle system to reduce the rattle band. As with Case 5, damping was found to be negligible.

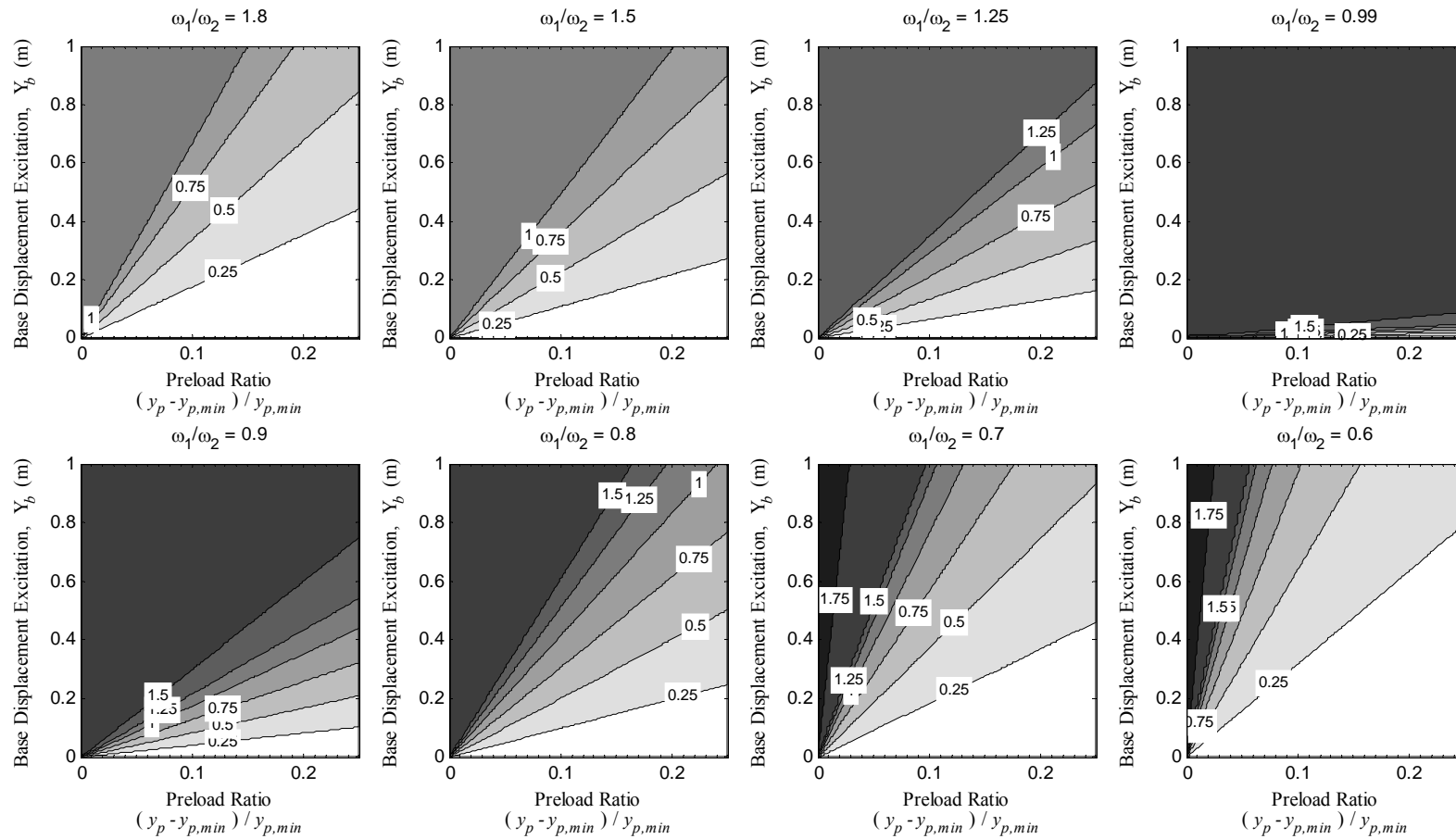


Figure 2.20: Contours of equal non-dimensional rattle bandwidth, λ , for Case 6 (static compressive displacement vs. base displacement excitation magnitude), $\gamma_1 = \gamma_2 = 0$.

2.2.c.iv Forced excitation

The next case study is for the same system excited with harmonic forced excitation, where F_b is the force magnitude. This is a case study of a situation where the flexible floor is excited directly by a force. In the application to airport noise, this may be a simple model for a wall excited by sound energy, with a preloaded object resting against it. The schematic model and free body diagram is shown in Figure 2.21 and Figure 2.19, respectively.

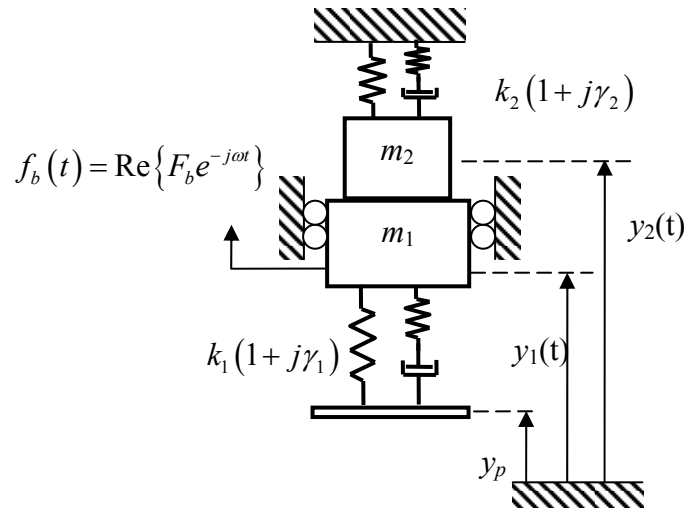


Figure 2.21: Schematic of model for Case 6, flexible system pre-loaded against a vibrating flexible base.

The development for the forced system is similar to the motion excitation system. The equations of motion for force excitation of Case 6 with damping is,

$$\text{Re}\left\{\left[k_1(1 + j\gamma_1) - \omega^2 m_1\right] Y_1 e^{-j\omega t}\right\} = \text{Re}\left\{F_b e^{-j\omega t}\right\} - f(t) + f_{st}, \quad (2.64)$$

$$\text{Re}\left\{\left[k_2(1 + j\gamma_2) - \omega^2 m_2\right] Y_2 e^{-j\omega t}\right\} = f(t) - f_{st}. \quad (2.65)$$

The solution for bulk motion, where $y = y_1 = y_2$, is obtained by adding equations (2.64) and (2.65).

$$\left[K + j(k_1\gamma_1 + k_2\gamma_2) - \omega^2 M\right] Y = F_b. \quad (2.66)$$

Therefore,

$$\begin{aligned}
 Y(j\omega) &= \frac{F_b}{\left[K - \omega^2 M + j(k_1 \gamma_1 + k_2 \gamma_2) \right]}, \\
 &= \left(\frac{F_b}{K} \right) \left\{ \frac{1}{\left[1 - (\omega/\omega_n)^2 \right]^2 + \left[(k_1 \gamma_1 + k_2 \gamma_2)/K \right]^2} \right\}^{1/2} e^{-j\phi}. \quad (2.67)
 \end{aligned}$$

Substitution of equation (2.67) into (2.65) and solving for the contact force, f , yields

$$f(t) = f_{st} + \left(\frac{k_2 F_b}{K} \right) \left\{ \frac{\left[1 - (\omega/\omega_2)^2 \right]^2 + \gamma_2^2}{\left[1 - (\omega/\omega_n)^2 \right]^2 + \left[(k_1 \gamma_1 + k_2 \gamma_2)/K \right]^2} \right\}^{1/2} \text{Re} \left\{ e^{-j(\omega t + \phi)} \right\}. \quad (2.68)$$

The spring is initially compressed from equilibrium by displacement y_p and is introduced through the static contact force, f_{st} , term along with gravitational loads. As discussed in the previous section it is required that $y_p > y_{p,\min}$. This ensures that the system is in contact with the base when the system is at rest.

Rattle onset will occur when the contact force becomes zero ($f = 0$), which occurs at peak acceleration amplitudes when $e^{-j(\omega t + \phi)} = -1$. Solving for rattle onset for the vertical orientation by substituting equation (2.43) for the static contact force,

$$0 = \left(\frac{k_1 k_2}{K} \right) (y_p - y_{p,\min}) - F_b \left(\frac{k_2}{K} \right) \left\{ \frac{\left[1 - (\omega/\omega_2)^2 \right]^2 + \gamma_2^2}{\left[1 - (\omega/\omega_n)^2 \right]^2 + \left[(k_1 \gamma_1 + k_2 \gamma_2)/K \right]^2} \right\}^{1/2}, \quad (2.69)$$

this can be rearranged as:

$$0 = \left[1 - (\omega/\omega_n)^2 \right]^2 + \left[(k_1 \gamma_1 + k_2 \gamma_2)/K \right]^2 + \left(\frac{F_b/k_1}{y_p - y_{p,\min}} \right)^2 \left[\left[1 - (\omega/\omega_2)^2 \right]^2 + \gamma_2^2 \right]. \quad (2.70)$$

Rearranging in the following manner, where $\mu = (\omega/\omega_n)^2$,

$$A\mu^2 + B\mu + C = 0, \quad (2.71)$$

where,

$$A = \left[1 + \left(\frac{\omega_n}{\omega_2} \right)^4 \left(\frac{F_b/k_1}{y_p - y_{p,\min}} \right)^2 \right], \quad (2.72)$$

$$B = -2 \left[1 + \left(\frac{\omega_n}{\omega_2} \right)^2 \left(\frac{F_b/k_1}{y_p - y_{p,\min}} \right)^2 \right], \quad (2.73)$$

$$C = \left[1 + \left(\frac{k_1\gamma_1 + k_2\gamma_2}{K} \right)^2 + \left(\frac{F_b/k_1}{y_p - y_{p,\min}} \right)^2 (1 + \gamma_2^2) \right]. \quad (2.74)$$

The rattle onset threshold for normalized frequency is,

$$\left(\frac{\omega}{\omega_n} \right)^2 = \mu_{1,2} = \frac{-B \pm \sqrt{B^2 - 4AC}}{2A}. \quad (2.75)$$

Thus upper and lower rattle thresholds:

$$\left(\frac{\omega}{\omega_n} \right)_{U,L} = \sqrt{\frac{|B| \pm \sqrt{B^2 - 4AC}}{2A}}, \quad (2.76)$$

such that $\omega_L < \omega_U$ and the lower rattle threshold, ω_L , must be greater than 0 Hz. The rattle band relationships will be left in this form and illustrated using parameter studies.

The sound energy can be described by incident sound pressure level. From the forced excitation model the rattle onset threshold can be described in terms of incident sound pressure level, L_p , where

$$L_p = 10 \log_{10} \left(p_{rms}^2 / p_{ref}^2 \right) \text{ [dB re } 20 \mu\text{Pa]}. \quad (2.77)$$

The incident pressure is proportional to the forcing excitation,

$$F_b = Sp_{pk} = \sqrt{2}Sp_{rms}, \quad (2.78)$$

where S is the surface area of the insonified panel, p_{pk} is the peak sound pressure, and p_{rms} is the incident sound pressure. The result is force excitation in terms of incident sound pressure level.

$$p_{rms} = p_{ref} \sqrt{10^{(L_p/10)}}. \quad (2.79)$$

By substitution of equation (2.78) into (2.79) the following is obtained

$$F_b = Sp_{ref} \sqrt{2} \sqrt{10^{(L_p/10)}} . \quad (2.80)$$

In Figure 2.22 the contours of rattle bandwidth, λ , are shown for various ratios of natural frequencies, $\omega_R = (\omega_1/\omega_2)$ for the incident pressure excitation system. The ratio, $\omega_R = (\omega_1/\omega_2)$, decreases across and down the subplot rows. Each of the eight systems are evaluated with no damping, $\gamma_1 = \gamma_2 = 0$. Similar observations are made as for Figure 2.20. Increasing preload decreases the rattle bandwidth. Dissimilar natural frequencies of the components also decrease the rattle bandwidth for constant preload and incident sound pressure level. A plot of the forced system with damping is not included because the effect of damping is negligible, as with Case 5.

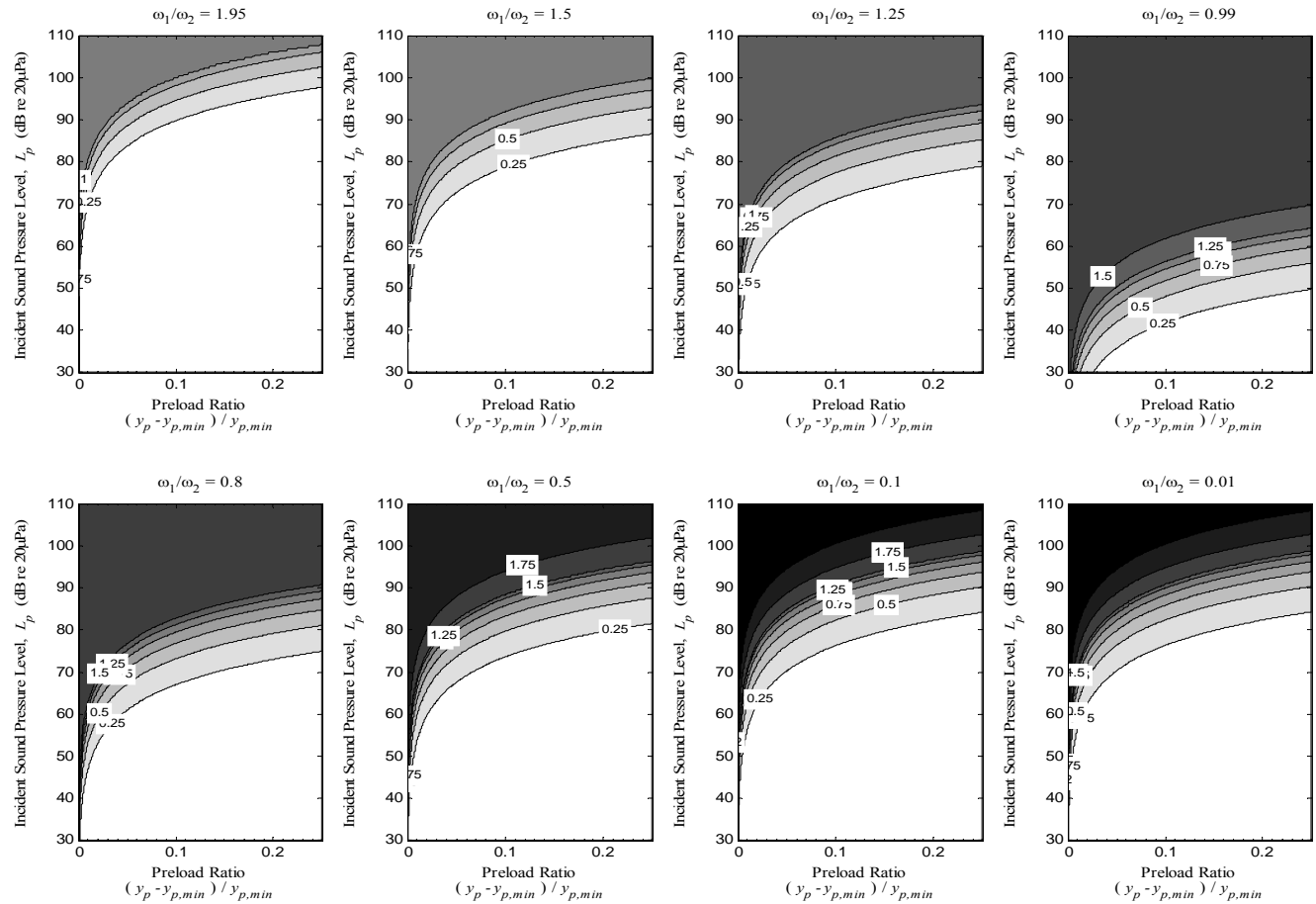


Figure 2.22: Contours of equal non-dimensional rattle bandwidth, λ , for Case 6 (static compressive displacement vs. incident sound pressure level), $\gamma_1 = \gamma_2 = 0$.

3 EXPERIMENTAL RATTLE STUDY

A rattle experiment was conducted at Purdue University's Ray W. Herrick Laboratories in order to evaluate the principles identified in the analytical rattle models. Four windows known to be susceptible to rattle were excited via high-fidelity playback of three, high-amplitude, low-frequency noise signals. The signals included pre-recorded aircraft take-off noise, a swept sine signal, and pink noise. The vibration and acoustic response of each of the windows was measured to determine the relationship between frequency and acceleration amplitude that is required for rattle onset.

3.1 Objective

The objective of the experiment was to identify the onset of rattle by investigating the response of window panels insonified with large amplitude, low-frequency sound waves.

3.2 Test Method

Four windows that were known to rattle were selected. The dynamic response of the four windows was measured first. The mode shapes of the windows were found to correspond to the low order modes of a large panel as expected. For rattle evaluation, the four windows were insonified at four different amplitudes using three input signal recordings. The recordings included aircraft take-off, swept sine, and pink noise. Each signal was played through an Altec 1201A loudspeaker and BagEnd P-D18E-R subwoofer configuration capable of radiating flat-spectrum noise from 20 Hz to 15 kHz. The excitation source is shown in Figure 3.1.



Figure 3.1: Loudspeaker set-up for rattle experiment.

For each signal, a series of four amplitudes were selected such that the lowest amplitude did not produce rattle for any of the four windows while the highest two signal strengths caused audible rattle of the window. Response of each window was measured using two accelerometers placed on the windows away from the primary nodal lines of the modes of the windows. Sound pressures inside and outside of the test room were also measured.



Figure 3.2: Experimental set-up at Herrick Labs, Loudspeakers directed at set of two large and two small windows.



Figure 3.3: Experimental set-up at Herrick Labs, Close-up of four windows.

The placement of loudspeakers and microphones relative to the panels (windows) was set-up as specified by ASTM E-966 [9], ISO 140-5 [10] and ISO 140-14 [11] standards. In Figure 3.2 the loudspeakers are shown directed at the bank of windows on the left, including two large (upper) windows and two small (lower) windows. The floor-to-ceiling windows shown in the center of Figure 3.2 were not measured in this study. A close up of the four windows is shown in Figure 3.3 with accelerometers attached to each window and microphones placed to record sound indoors and outdoors of the room. A schematic of the loudspeaker and microphone placements is shown in Figure 3.4.

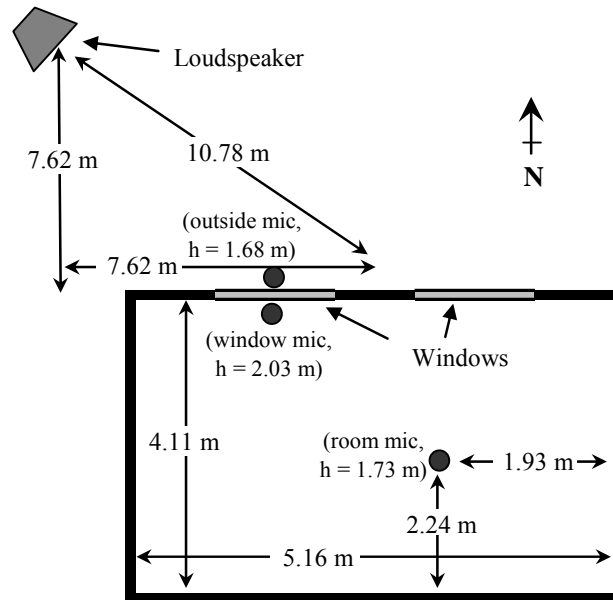


Figure 3.4: Schematic of rattle experiment. Placement of loudspeaker and microphones.

The loudspeakers were placed 10.78 m (35' 4") from the mid-point between the sets of windows at an angle of 45° on top of a folding-table, 0.76 m (2' 6") off the ground. All three microphones were covered with windscreens. The windscreen of the outside microphone was cut away so that the microphone could be placed 12 mm (1/2 in.) away from the window.

3.3 Mobility Analysis of Rattle-Prone Windows

The four windows in the rattle experiment were all made from single-pane glazing with aluminum frames. The two upper windows, shown in Figure 3.3, were both 1.22 m x 1.22 m (48" x 48"). The lower windows were both 1.17 m x 0.36 m (46" x 14"). The lower windows opened inwards pivoting down; i.e. they were hopper-style windows. During the experiment both lower windows were latched securely.

The mobility of the panels was measured on the four test windows to determine the natural frequencies of each window. Mobility is the inverse of mechanical impedance, or the ratio of complex amplitude of velocity and force for a particular interface. The mobility was

measured by striking each window with an impact hammer and measuring the vibration response with an accelerometer. For post-process analysis, a force window with 10% trigger was applied to the input channel (PCB Type 086C03 medium impact hammer) and an exponential window with time constant, $\tau = 1.3896$ seconds, to the output channels (PCB Type 333B32 accelerometers) to minimize the effects of background noise.

In order to accurately identify higher-order mode shapes, five accelerometers were placed asymmetrically on the upper windows away from nodal lines as shown in Figure 3.5. Four accelerometers were mounted on the lower windows as shown in Figure 3.6. The impact hammer was struck at each of the grid points and the drive-point and cross mobilities were measured using the accelerometers. Multiple Reference Impact Testing (MRIT) and X-Modal software [12], written at the University of Cincinnati and implemented by the Purdue University structural-health-monitoring group, was used to capture mobility data and identify natural frequencies of the windows. MRIT was used to capture data, while X-Modal was used to identify natural frequencies from a synthesis of the response for all grid-point impact excitations.

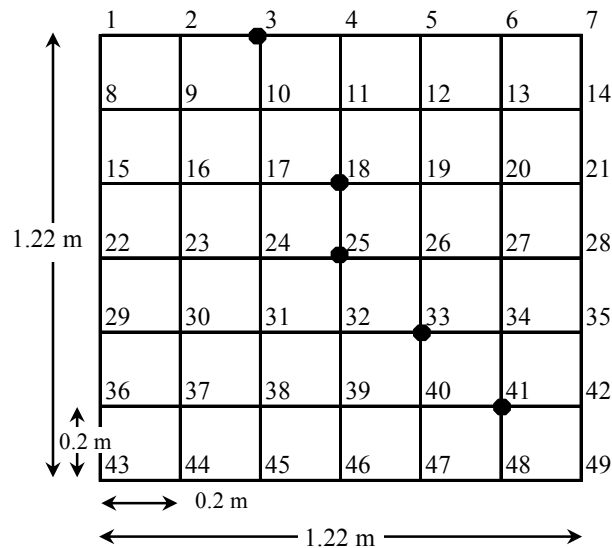


Figure 3.5: Grid-point locations for 1.22 m x 1.22 m (48'' x 48'') upper window with five accelerometer locations denoted by black dots.

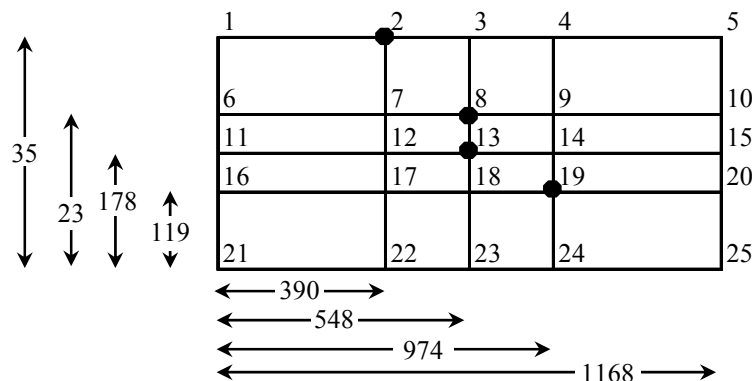


Figure 3.6: Grid-point locations for 1.17 m x 0.36 m (46" x 14") lower window with four accelerometer locations denoted by black dots. Dimensions in mm.

The natural frequencies of the four windows are shown in Table 3.1. The natural frequencies are similar for the windows having the same geometry, as expected. Differences can be attributed to the age of windows and irregularities at the window frame boundary conditions.

Table 3.1: Natural frequencies of four rattle-prone windows.

Natural Frequencies (Hz)			
<i>Lower East</i>	<i>Lower West</i>	<i>Upper East</i>	<i>Upper West</i>
30	37	26	25
35	52	43	41
44	68	53	51
51	91	70	66
65	122	90	87
121		97	91
160		106	126
		134	133
		137	145
		154	158
		172	165
		181	173
		221	203
		242	239
		263	252
		267	262

3.4 *Experimental Results*

The response of one window (lower east), in the bottom left corner of Figure 3.3, to the highest signal strength swept sine, aircraft take-off, and pink noise signals is presented in this section. The complete results for all four windows are compiled in the Appendices. Spectrogram plots are contained in Appendix A and acceleration level versus frequency for all four windows is contained in Appendix B.

Measurement locations include an outdoor microphone, which is used to measure the noise source, an indoor room microphone, and window-mounted accelerometers. All vibration response plots are the response measured using the accelerometer at location 33 as shown in Figure 3.5 for the upper window and location 19 as shown in Figure 3.6 for the lower windowsFigure .

The background noise measured using the outside microphone is shown in Figure 3.7 in the form of a spectrogram. The background noise spectrogram is shown in the top subplot. To create the spectrogram an FFT length of 4096 samples was included per time slice with a Hanning window applied and 85% overlap. The sampling frequency was 4096 Hz. The time history of the (1/8) second time-averaged equivalent level, L_{eq} , is shown in the bottom subplot of the respective figures. Unweighted, A-weighted, and C-weighted equivalent sound levels are shown in the lower subplot. The vibration response of the lower east window to the background noise is shown in Figure 3.8.

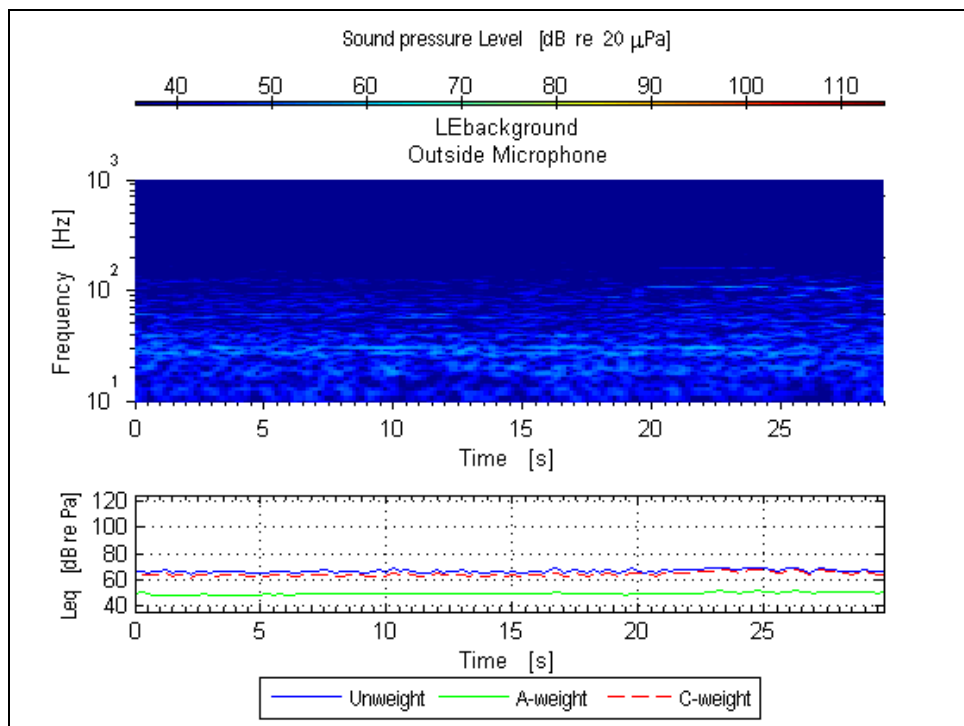


Figure 3.7: Background noise sound pressure level at the outside microphone.

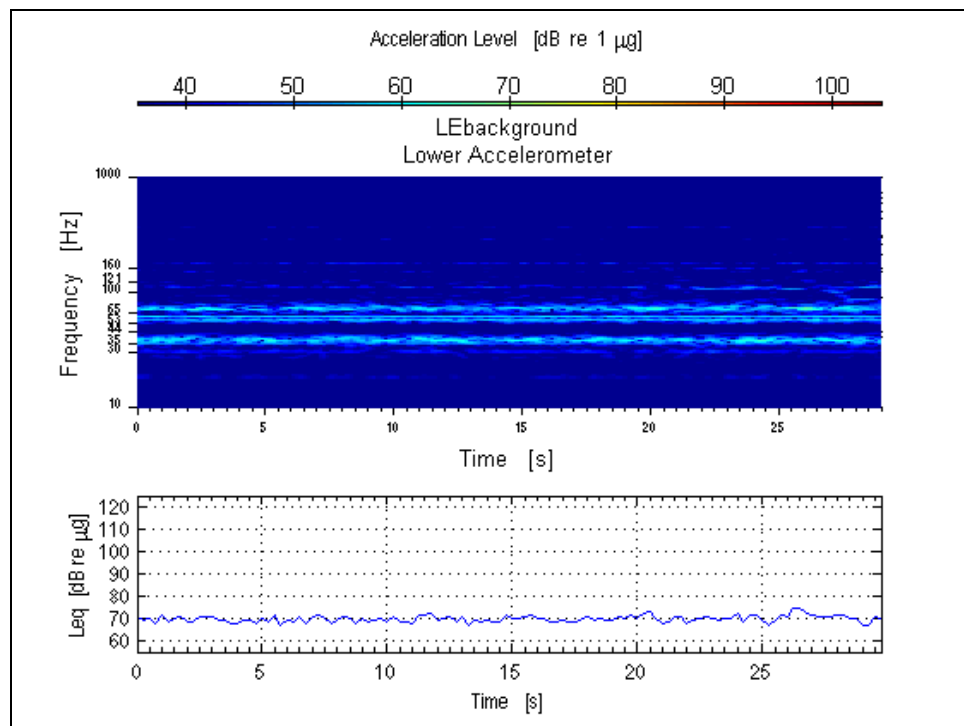


Figure 3.8: Vibration response of window to background noise.

The horizontal highlights of the window vibration response spectrogram shown in Figure 3.8 correspond to the low order natural frequencies of the window. The dotted line at 100 dB on the L_{eq} subplot represents a rattle threshold determined by this experimental study which will be discussed later. For now it is noteworthy to mention that the response of the window is well below the experimental rattle threshold despite larger acceleration response at the natural frequencies.

3.4.a Swept Sine Excitation

For the highest signal strength for the swept sine signal, the resulting overall sound pressure level at the outside window surface was 100 dBC as shown in Figure 3.9. The acceleration response of the lower east window to the highest amplitude swept sine signal is shown in Figure 3.10. The swept sine signal sweeps down from 700 Hz to 20 Hz, repeating after 78 seconds. The bottom-most diagonal line shown in both figures is the response to the input frequency from the swept sine frequency generator. The parallel lines are due to harmonic distortion caused by driving the loudspeakers at high amplitudes: i.e. beyond their linear range. The microphone and accelerometer responses were recorded simultaneously.

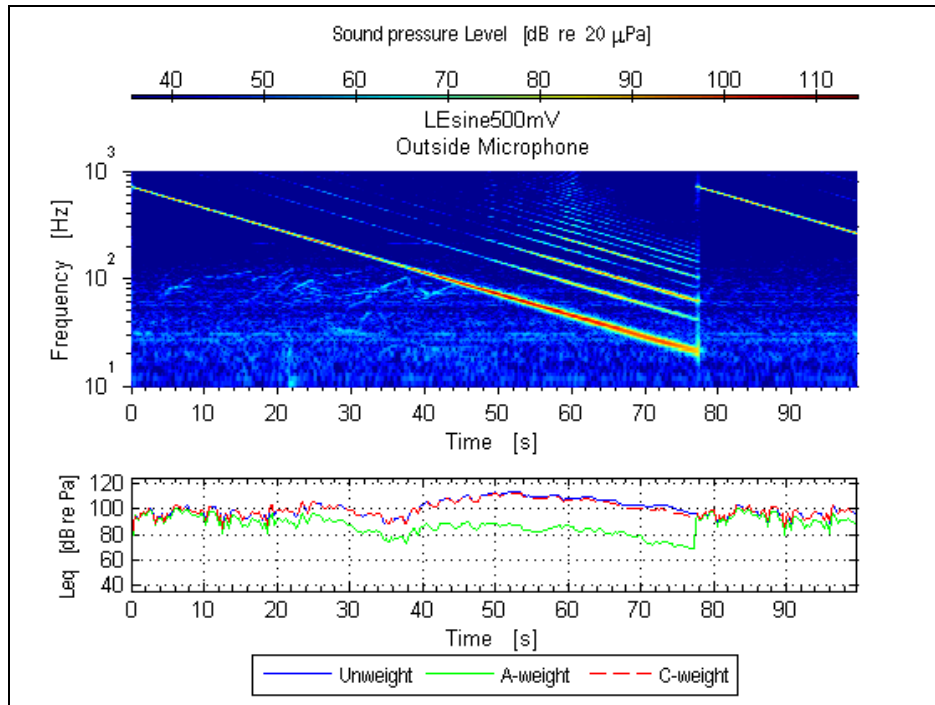


Figure 3.9: Sound pressure level measured at the outside microphone to the swept sine.

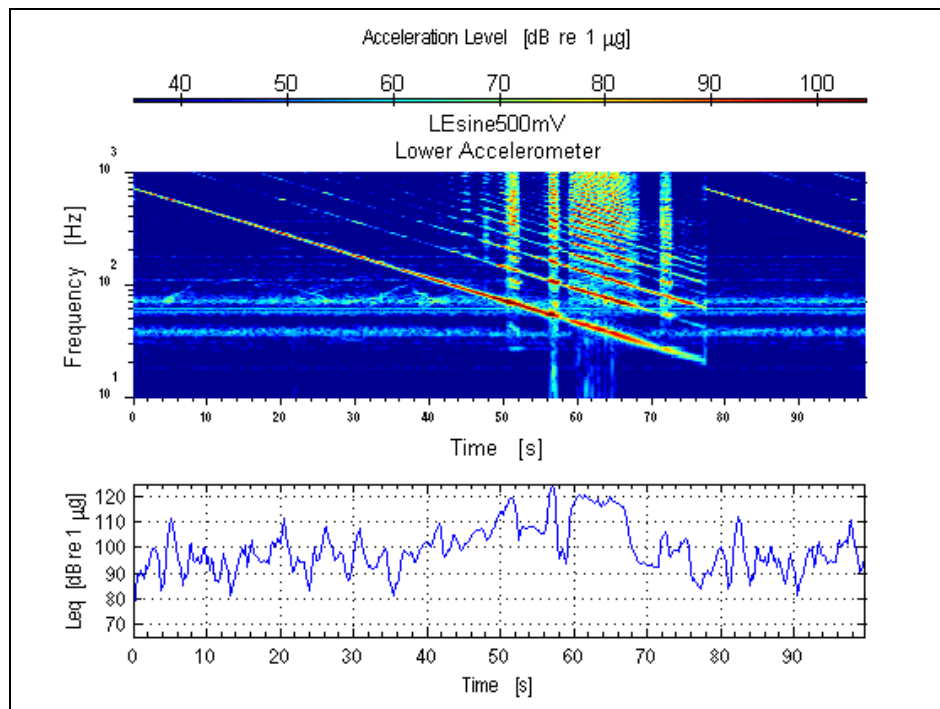


Figure 3.10: Vibration response of the lower left window to highest swept sine signal amplitude with overall sound pressure level of 100 dBC.

Rattle events occurred at the frequencies of the vertical highlights, indicating non-linear, broadband window response to acoustical excitation. Previous studies also described rattle as a broadband response [13]. The rattle onset typically occurred when the acceleration level exceeded 100 dB re 1 μg or 0.1 g_{rms} . In the frequency range shown (10-1000 Hz) in Figure 3.9 rattle is not “heard” by the outside microphone. The spectrogram in Figure 3.11 is identical to Figure 3.10 except the frequency scale is over the low frequency range (10-200 Hz).

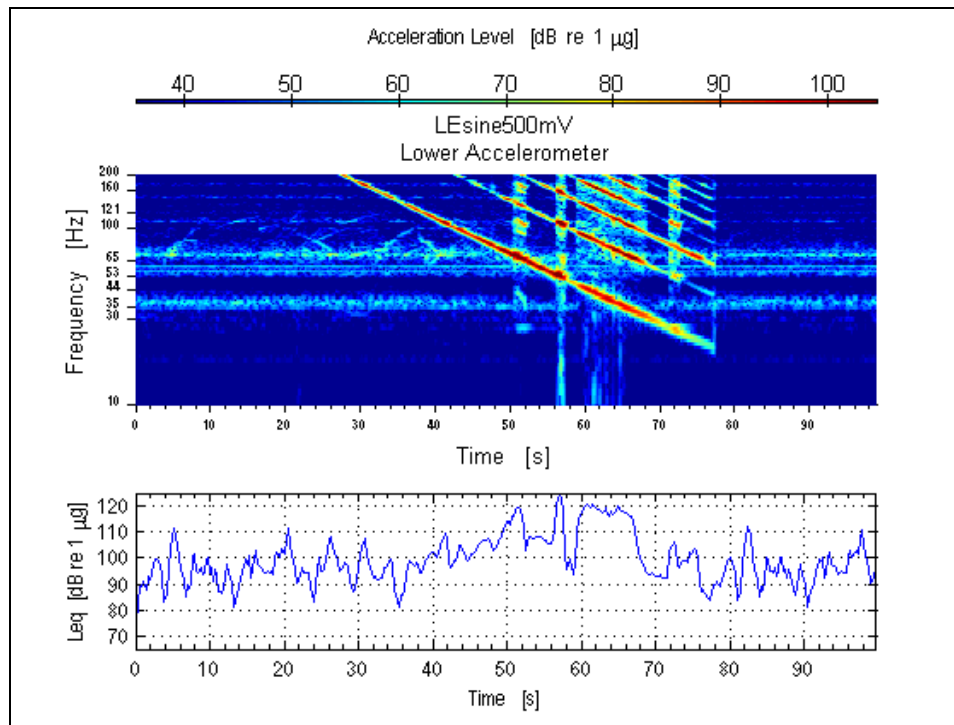


Figure 3.11: Same plot as Figure 3.10 but with smaller frequency scale (10-200 Hz).

The bottom-most diagonal line is the swept sine (700-20 Hz) from the function generator and again the parallel lines are harmonic distortion from driving the loudspeaker at high amplitudes. The tick marks on the frequency axis indicate the resonances of the window which were determined by the mobility test described earlier. The first rattle event (seen as a vertical highlight) occurs when the swept sine passes through 65 Hz and corresponds to the resonance of the window at 65 Hz. The second rattle event corresponds to resonance of the window at 53 Hz. Rattle also occurs at resonance of 44 Hz and carries through to the 35 Hz resonance. The final

rattle event occurs when the swept sine passes through the 30 Hz resonance of the window. Near each of the resonances, rattle occurs over a range of frequencies. This range of frequencies is the rattle band discussed earlier. The rattle band is centered at the natural frequency as predicted by the analytical models.

Overall acceleration levels, L_{eq} , of the lower east window to the four signal amplitudes of the swept sine are shown in Figure 3.12. The four signal strengths corresponded to different overall outside sound levels measured at the surface of the window, which are indicated by the different line-styles (‘dash-dot-dot’ = 70 dBC overall outside sound level, ‘dash-dot’ = 80 dBC, ‘dashed’ = 90 dBC, and ‘solid’ = 100 dBC). The range of frequencies over which the window rattled is identified using a bold line-style. Rattle onset was determined via visual inspection of the window response spectrogram to determine when the window was excited into broadband response.

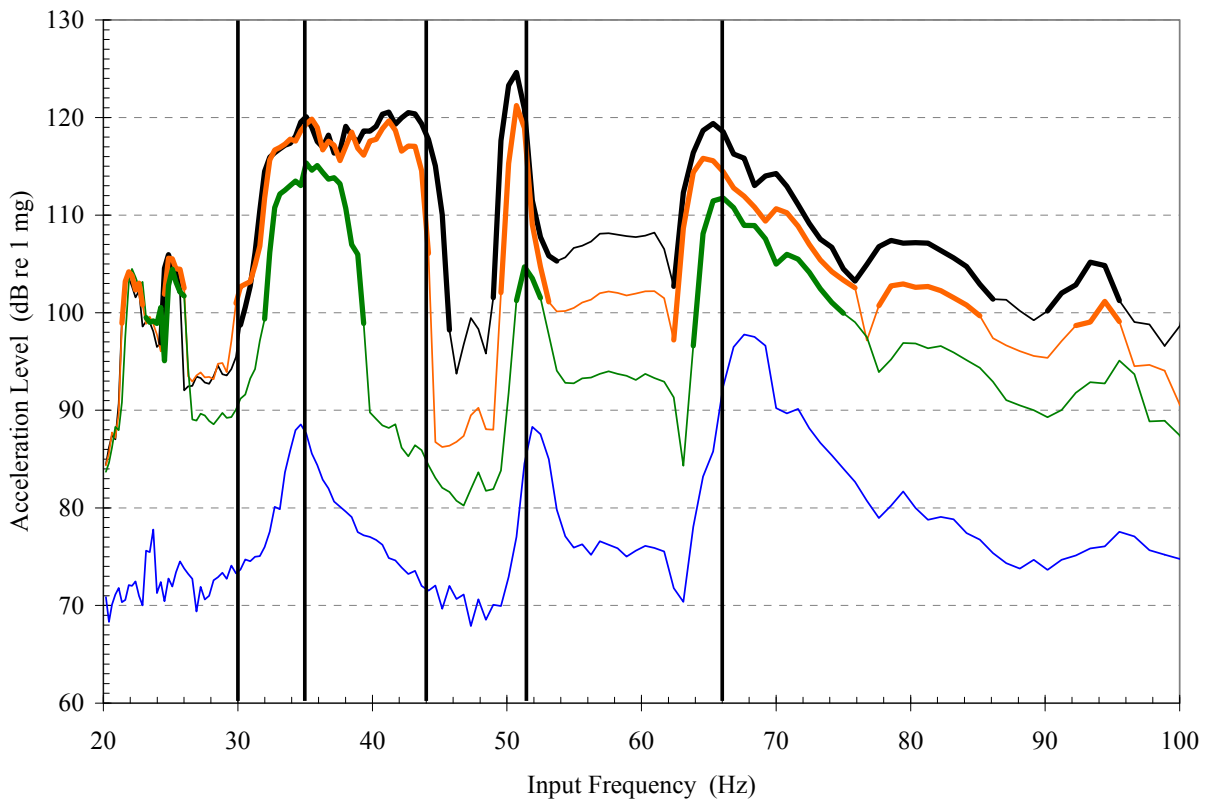


Figure 3.12: Response of the lower east window to four swept sine signal strengths; 70 dBC blue, 80 dBC green, 90 dBC orange, 100 dBC black. Bolded line-style indicates input frequencies at which rattle occurred.

The natural frequencies of the window are indicated by the vertical, black lines at 30, 35, 44, 51, and 65 Hz. These frequencies correspond with the natural frequencies as determined by mobility analysis and listed in Table 3.1. The location of this accelerometer is apparently on a nodal line of the 30 Hz resonance and thus “blind” to that resonance.

Several observations can be made based on the results shown in Figure 3.12. First, the rattle did not occur at any frequency for the lowest signal amplitude indicated by the blue C-weighted 70 dB line, even though resonant behavior is evident from the increased acceleration level near the natural frequencies. Thus, for the right combination of parameters (excitation amplitude, preload, material stiffness), rattle can be mitigated. Secondly, for this window, rattle occurred at acceleration levels greater than 100 (dB re 1 μg) or 0.1 g_{rms} . Thirdly, the rattle bandwidth increases for increasing excitation amplitude. This is most apparent, perhaps, for rattle near the 52 Hz resonance. For increasing signal amplitude, the bandwidth over which rattle occurs is larger. Fourthly, the rattle onset threshold (acceleration amplitude) for the window is essentially the same regardless of the mode shape.

The rattle behavior of the window corresponds well to the behavior of the Case 6 rattle system. The Case 6 rattle system model predicts an upper and lower rattle onset threshold centered about the natural frequency of the system. In the rattle experiment upper and lower rattle onset thresholds are centered about the resonances of the window. The Case 6 rattle system model predicted that for increasing excitation acceleration amplitude the rattle bandwidth increased. This same phenomenon occurs in the window response to the swept sine.

The acceleration levels for all four windows corresponding to the outside sound pressure level is plotted for all sampled values in Figure 3.13. The scatter or range of incident sound pressure level and resulting acceleration level of the window response are shown in the plot. Non-rattle response is indicated by x's, rattle onset by ♦'s and rattle response by ■'s. The purple shaded region is the range of window acceleration level response to incident sound pressure level in the measurements conducted by NASA Langley [14][15] and summarized by Hubbard [3]. The range of acceleration level response of the four windows in this investigation is significantly higher than the region of measure window response in the Hubbard study. This may be due to the large size of the windows as well as the condition and old age of the four windows. The two of the four windows measured in this investigation were 1.22 m (48 in) square windows with

single-pane glass in an aluminum frame. The other two windows were 1.17 m x 0.36 m (46" x 14"). The type and condition of the windows measured in the Hubbard study is unknown.

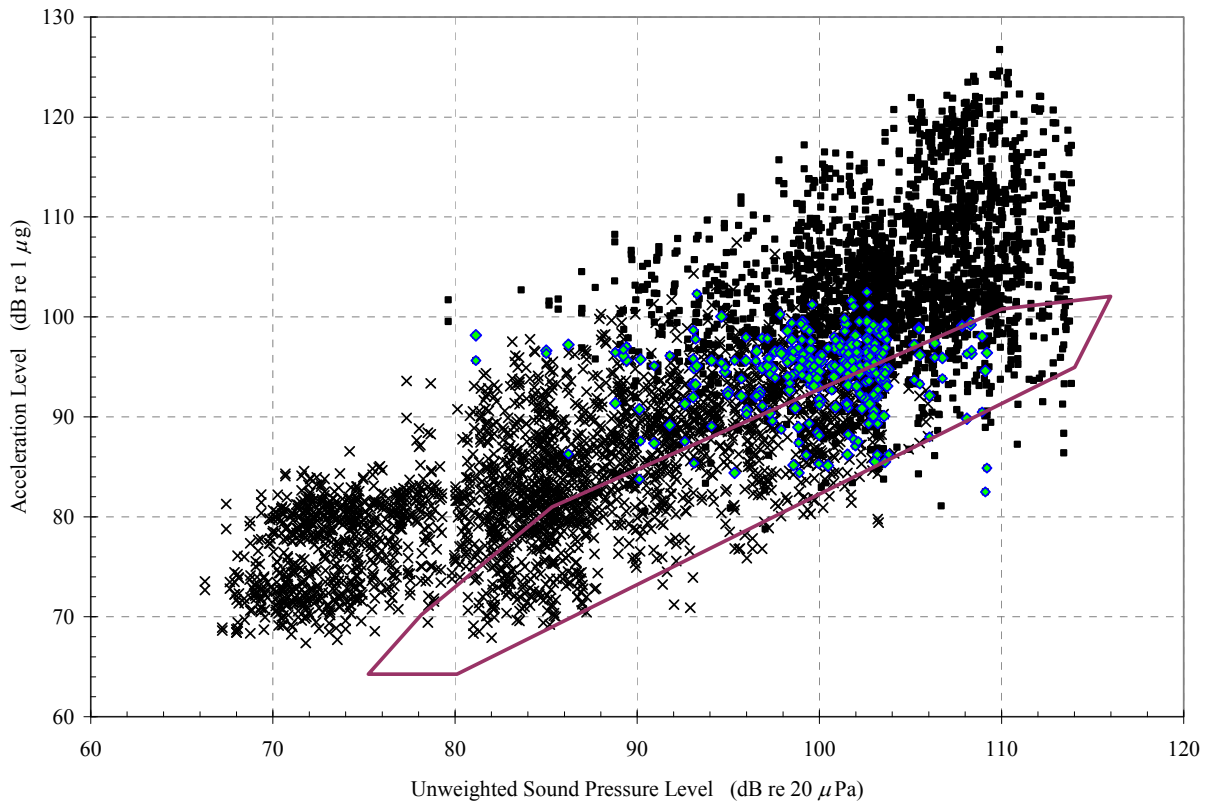


Figure 3.13: Acceleration response of all four windows to Swept Sine at various sound pressure levels: Non-rattle rattle response (x); Rattle onset (o); Rattle response (■). Shaded region is the range of measured window acceleration response reported in Hubbard [3].

3.4.b Aircraft Take-Off Excitation

The aircraft take-off signal is considered to be a random signal in time. Shown in Figure 3.14 is the spectrogram of the outside microphone measuring the aircraft take-off signal with overall equivalent sound pressure level, $L_{eq} = 95$ dB at the window. The pre-recorded aircraft signal used in this study was a recording of a typical large jet aircraft take-off measured from a single location. It is evident that aircraft take-off noise contains significant low frequency content, as shown by the 20 dB difference between the A-weighted and C-weighted L_{eq} at the beginning of the measurement. The low frequency content is consistent throughout the signal as seen in the spectrogram. The incident sound pressure level and vibration response of the window to the highest aircraft take-off signal amplitude is shown in Figure 3.14 and Figure 3.15.

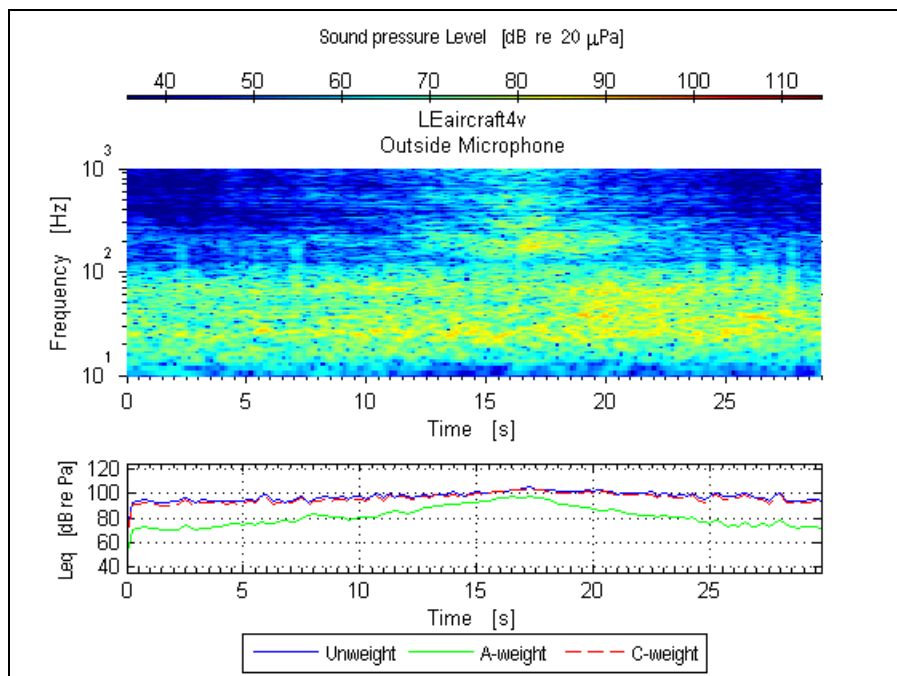


Figure 3.14: Sound pressure level measured at the outside microphone to highest aircraft take-off signal amplitude.

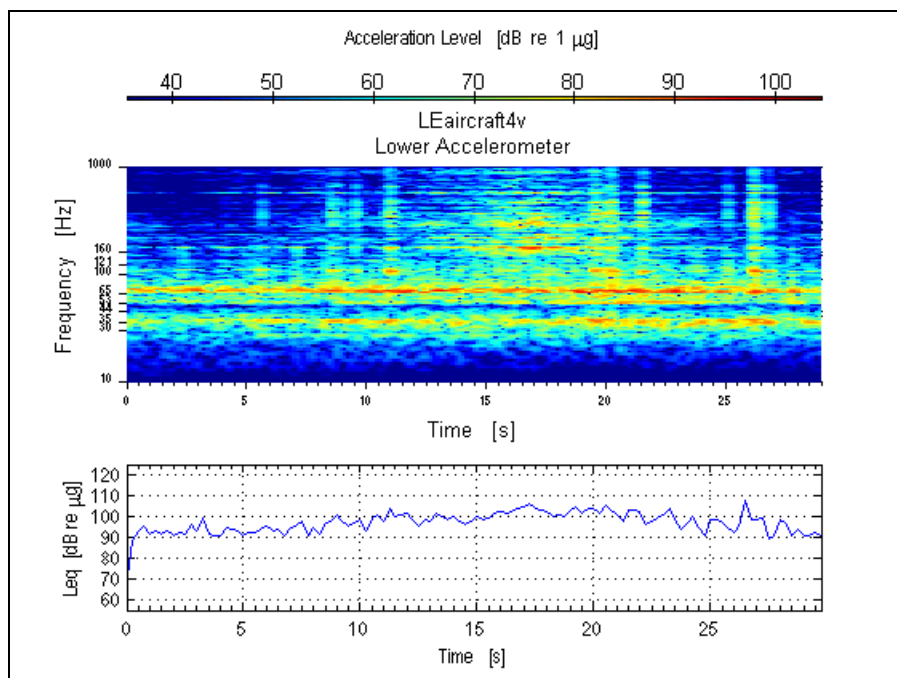


Figure 3.15: Vibration response of the lower east window to highest aircraft take-off signal amplitude.

Rattle events are identifiable as vertical highlights, indicating non-linear, broadband response at times 6 s, 9 s, 11 s, 20 s, 22 s, and 26 s. Rattle onset typically occurred when the acceleration level, L_{eq} , was greater than 100 dB (re $1\mu\text{g}$) or $0.1 g_{rms}$. Audible rattle events are tabulated in Table 3.2 for all aircraft take-off measurements.

Table 3.2: Audible rattle events during measurement for aircraft take-off signal.

Window	Signal Amplitude, Incident Sound Level (dB)	Rattle Not Audible	Rattle Audible
Lower East	70	X	
	80		X
	90		X
	100		X
Lower West	70	X	
	80		X
	90		X
	100		X
Upper East	70	X	
	80		X
	90		X
	100		X
Upper West	70	X	
	80		X
	90		X
	100		X

3.4.c Random Excitation

The pink noise signal is a random signal in time. Shown in Figure 3.16 is the spectrogram of the outside microphone measuring the pink noise signal with overall equivalent sound pressure level, $L_{eq} = 100$ dB at the window. The sound level is relatively uniform across the measured frequency range. The incident sound pressure level and vibration response of the window to the highest aircraft take-off signal amplitude are shown in Figure 3.16 and Figure 3.17.

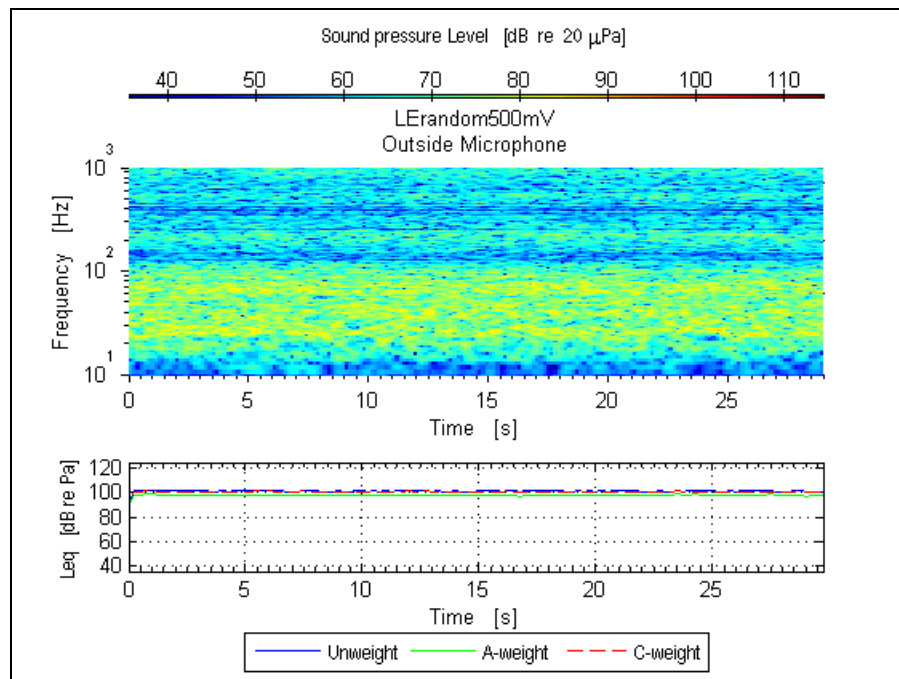


Figure 3.16: Sound pressure level measured at the outside microphone to highest pink noise signal amplitude.

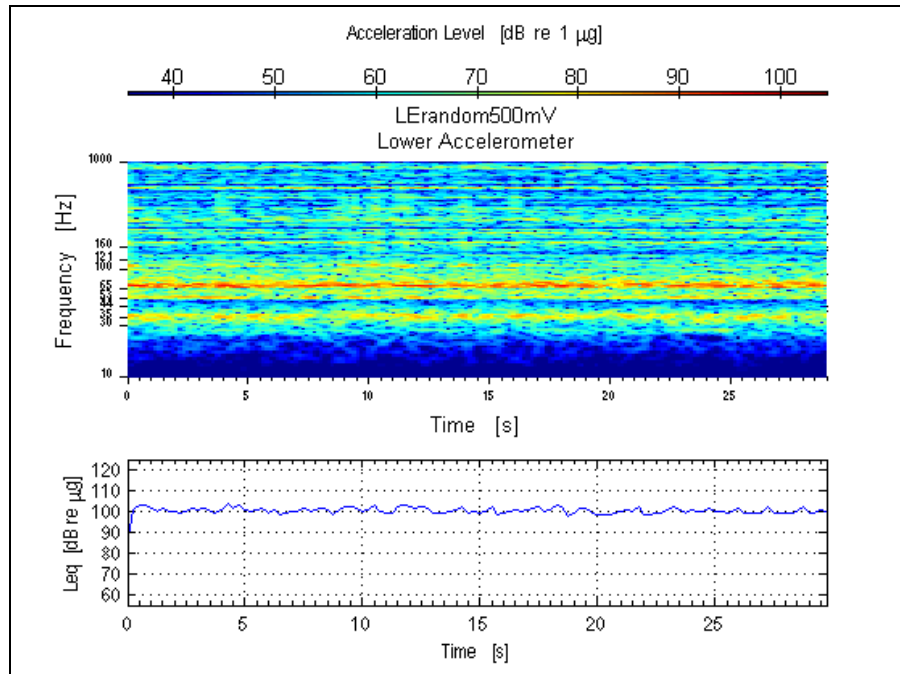


Figure 3.17: Vibration response of the lower east window to highest pink noise signal amplitude.

The tic marks along the frequency axis indicate the natural frequencies of the window as determined by the mobility test. Rattle was audible during this measurement at 4 s, 9 s, 10 s, 12 s, 14 s, and 16 s. Faint vertical highlights can be seen in the spectrogram at these points in time. More pronounced is the window response at the natural frequencies. This can be seen as the horizontal highlights of increased acceleration level for given frequency. Audible rattle events are tabulated in Table 3.3 for all pink noise measurements.

Table 3.3: Audible rattle events during measurement for pink noise signal.

Window	Signal Amplitude, Incident Sound Level (dB)	Rattle Not Audible	Rattle Audible
Lower East	70	X	
	80	X	
	90		X
	100		X
Lower West	70	X	
	80	X	
	90		X
	100		X
Upper East	70	X	
	80	X	
	90		X
	100		X
Upper West	70	X	
	80	X	
	90		X
	100		X

4 SUMMARY AND CONCLUSIONS

Six analytical models of rattle systems were investigated. Three of the models, Cases 1 through 3, are models of non-resonant systems which are comparable to those studied in previous research. The other three models, Cases 4 through 6, are models of resonant systems. Rattle criteria have been developed for various excitation sources, including harmonic base motion and forced excitation. For harmonic base motion, the rattle onset threshold was expressed in terms of acceleration magnitude for all but Case 5 and Case 6, which is expressed in terms of base displacement amplitude. For forced excitation, a rattle onset threshold was derived in terms of the incident sound pressure amplitude. These criteria include the rattle onset threshold and the rattle bandwidth.

In all six models, a decrease of the excitation is an effective mitigation strategy. Only Case 3 is affected by lean angle. For Case 5 the rattle onset threshold is one-sided with rattle occurring at all frequencies above the rattle onset threshold. For Case 4 and 6, where flexible elements preload the masses, the rattle onset threshold is two-sided, having an upper and lower onset threshold centered about the natural frequency of the total system. The rattle bandwidth can be minimized by increasing preload and/or designing the sub-system natural frequencies to be dissimilar, as in $\omega_1 \ll \omega_2$ or $\omega_1 \gg \omega_2$. Thus, a mitigation strategy might be to either stiffen or soften one of the flexible bodies involved in the rattle system. The non-resonant rattle onset thresholds are summarized in Table 4.1 and the resonant rattle onset thresholds in Table 4.2.

Table 4.1: Rattle onset thresholds for non-resonant systems.

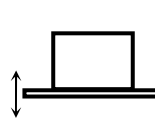
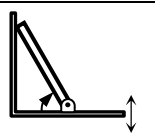
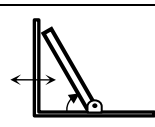
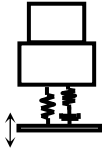
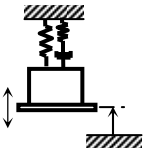
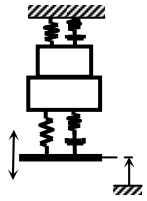
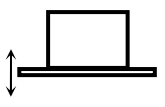
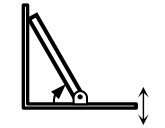
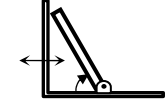
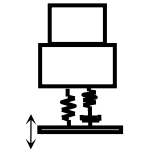
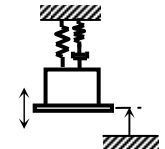
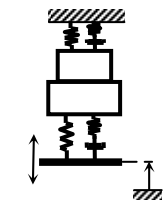
		<i>Harmonic Motion Excitation</i>	<i>Pressure Excitation</i>
<i>Case 1</i>		$A_b > g$	--
<i>Case 2</i>		$A_b > g$	--
<i>Case 3</i>		$A_b > \frac{g}{2 \tan \theta}$	--

Table 4.2: Rattle onset thresholds for resonant systems.

		<i>Harmonic Motion Excitation</i>	<i>Pressure Excitation</i>
<i>Case 4</i>		$\sqrt{1 - \sqrt{(A_b/g)^2 (1 + \gamma^2) - \gamma^2}}$ $< (\omega/\omega_n) <$ $\sqrt{1 + \sqrt{(A_b/g)^2 (1 + \gamma^2) - \gamma^2}}$	--
<i>Case 5</i>		$\left(\frac{\omega}{\omega_n}\right) > \sqrt{1 + \sqrt{\left(\frac{y_p - y_{p,\min}}{Y_b} - 1\right)^2 - \gamma^2}}$	--
<i>Case 6</i>		$\omega_1 > \omega_n > \omega_2 :$ $\sqrt{\frac{y_p - y_{p,\min} + Y_b}{y_p - y_{p,\min} + (\omega_n/\omega_2)^2 Y_b}}$ $< (\omega/\omega_n) <$ $\sqrt{\frac{y_p - y_{p,\min} - Y_b}{y_p - y_{p,\min} - (\omega_n/\omega_2)^2 Y_b}}$ $\omega_1 < \omega_n < \omega_2 :$ $\sqrt{\frac{y_p - y_{p,\min} - Y_b}{y_p - y_{p,\min} - (\omega_n/\omega_2)^2 Y_b}}$ $< (\omega/\omega_n) <$ $\sqrt{\frac{y_p - y_{p,\min} + Y_b}{y_p - y_{p,\min} + (\omega_n/\omega_2)^2 Y_b}}$	$\omega_1 > \omega_n > \omega_2 :$ $\sqrt{\frac{y_p - y_{p,\min} + (\sqrt{2}Sp_{rms}/k_1)}{y_p - y_{p,\min} + (\omega_n/\omega_2)^2 (\sqrt{2}Sp_{rms}/k_1)}}$ $< (\omega/\omega_n) <$ $\sqrt{\frac{y_p - y_{p,\min} - (\sqrt{2}Sp_{rms}/k_1)}{y_p - y_{p,\min} - (\omega_n/\omega_2)^2 (\sqrt{2}Sp_{rms}/k_1)}}$ $\omega_1 < \omega_n < \omega_2 :$ $\sqrt{\frac{y_p - y_{p,\min} - (\sqrt{2}Sp_{rms}/k_1)}{y_p - y_{p,\min} - (\omega_n/\omega_2)^2 (\sqrt{2}Sp_{rms}/k_1)}}$ $< (\omega/\omega_n) <$ $\sqrt{\frac{y_p - y_{p,\min} + (\sqrt{2}Sp_{rms}/k_1)}{y_p - y_{p,\min} + (\omega_n/\omega_2)^2 (\sqrt{2}Sp_{rms}/k_1)}}$

Rattle mitigation strategies are tabulated for the six rattle models in Table 4.3. In general, reducing excitation and increasing preload will increase the rattle onset threshold and mitigate rattle.

Table 4.3: Rattle mitigation strategies

		<i>Harmonic Motion Excitation</i>	<i>Pressure Excitation</i>
<i>Case 1</i>		<i>Reduce excitation.</i>	--
<i>Case 2</i>		<i>Reduce excitation.</i>	--
<i>Case 3</i>		<i>Reduce excitation.</i> <i>Reduce angle.</i>	--
<i>Case 4</i>		<i>Increase pre-load.</i> <i>Reduce excitation.</i>	--
<i>Case 5</i>		<i>Increase pre-load</i> <i>Reduce excitation.</i> <i>Decrease natural frequency</i> <i>(reduce stiffness or increase mass).</i>	--
<i>Case 6</i>		<i>Increase pre-load.</i> <i>Reduce excitation.</i> <i>Soften or stiffen one flexible</i> <i>body relative to the other.</i>	<i>Increase pre-load.</i> <i>Reduce excitation.</i> <i>Soften or stiffen one flexible</i> <i>body relative to the other.</i>

Experiments were conducted to verify the possible usefulness of the analytical rattle models. Four windows prone to rattle were tested with three types of excitation signals (swept sine, pre-recorded aircraft take-off, and random pink noise) at various signal strength amplitudes. The rattle behavior of the window tested in the rattle experiment was in qualitative agreement with the behavior predicted by the horizontal orientation Case 6 resonant rattle model. The rattle

occurred in a frequency band near the resonant frequencies of the window. This behavior is consistent with predicted response of the analytical models. Several key observations may be made. Rattle did not occur at any frequency for the lowest signal amplitude though resonant behavior is evident. Thus for the right combination of parameters (excitation amplitude, preload, material stiffness), rattle can be mitigated. Secondly, the rattle bandwidth increased for the increasing excitation amplitude. Lastly, the rattle onset threshold (acceleration amplitude) for the window was independent of frequency.

This study has investigated the mechanisms which cause rattle. Resonant rattle models were developed which better represent the response of systems into rattle than previous non-resonant rattle models.

5 LIST OF REFERENCES

- [1] F. Kavarana, B. Rediers, Squeak and Rattle—State of the Art and Beyond, *Sound and Vibration*, pp. 56-64, April, (2001).
- [2] L.C. Sutherland, S. Fidell, and A. Harris, Findings of the Low-Frequency Noise Expert Panel of the Rickfield-MAC Mitigation Agreement of 17 December 1998, Volumes I, II, and III, 30 September (2000).
- [3] H.H. Hubbard, Noise Induced House Vibrations and Human Perception, *Noise Control Engineering Journal*, Vol. 19, pp.49-55, (1982).
- [4] P.D. Schomer, S.D. Hottman, F.M. Kessler, and R.K. Kessler, Expedient Methods for Rattle-Proofing Certain Housing Components, *USA-CERL, N-87/24*, (1987).
- [5] S.A. Clevenson, Experimental Determination of the Rattle of Simple Models, NASA Langley Research Center, *NASA-TM-78756*, (1978).
- [6] H.D. Carden and W.H. Mayes, Measured Vibration Response Characteristics of Four Residential Structures Excited by Mechanical and Acoustical Loadings, NASA Langley Research Center, *NASA-TN-D-5776*, (1970).
- [7] L.C. Sutherland, Low Frequency Response of Structures, *Wyle Report, WR-82-18*, (1982).
- [8] L.C. Sutherland, B.H. Sharp, and R.A. Mantey, Preliminary Evaluation of Low Frequency Noise and Vibration Reduction Retrofit Concepts for Wood Frame Structures, *Wyle Report, WR-83-26*, (1983).
- [9] ASTM E966, Standard Guide for Field Measurements of Airborne Sound Insulation of Building Façade Elements, American Society for Testing and Materials (ASTM), West Conshohocken, PA, (2002).
- [10] ISO 140-5, Acoustics—Measurement of Sound Insulation in Buildings and of Building Elements—Part 5: Field Measurements of Airborne Sound Insulation of Façade Elements and Façades, International Organization for Standardization (ISO), Geneva, (1998).
- [11] ISO 140-14, Acoustics—Measurement of Sound Insulation in Buildings and of Building Elements—Part 14: Guidelines for Special Situations in the Field, International Organization for Standardization (ISO), Geneva, (2004).
- [12] H. Kess, MRIT and X-Modal Users Manual, Purdue University, December, (2004).
- [13] J.-Y. Her and S.-R. Hsieh, A Review of Squeak and Rattle Prevention – A Personal Perspective, *Proceedings of Noise-Con '98*, Ypsilanti, MI, April 5-8 (1998).
- [14] Staff-Langley Research Center: Concorde Noise-Induced Building Vibrations, John F. Kennedy International Airport, Report No. 3, NASA TM-78727, (April 1978).
- [15] Staff-Langley Research Center: Concorde Noise-Induced Building Vibrations, International Airport Dulles—Final Report, NASA TM-74083 (September 1977).

6 APPENDICES

6.1 Appendix A: Experimental plots of rattle study

6.1.a Plots of Lower East (LE) window

6.1.a.i Background noise on Lower East (LE) window

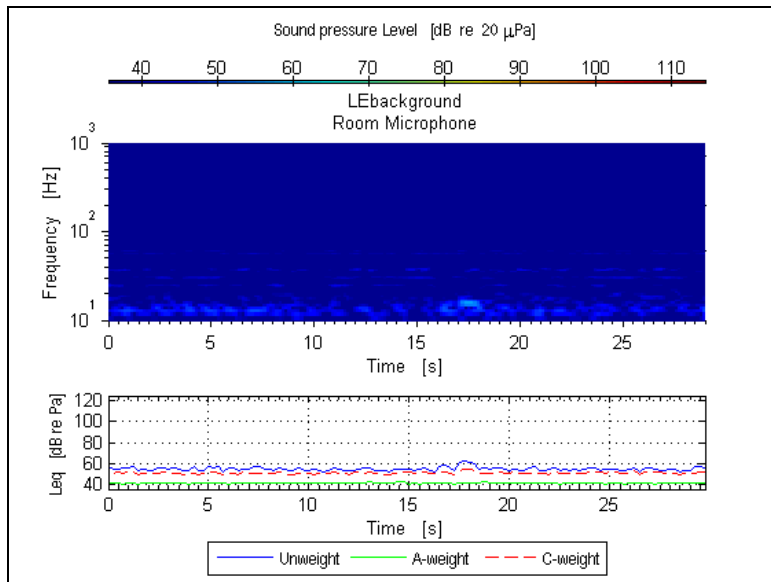


Figure A.1: Room mic measuring background noise

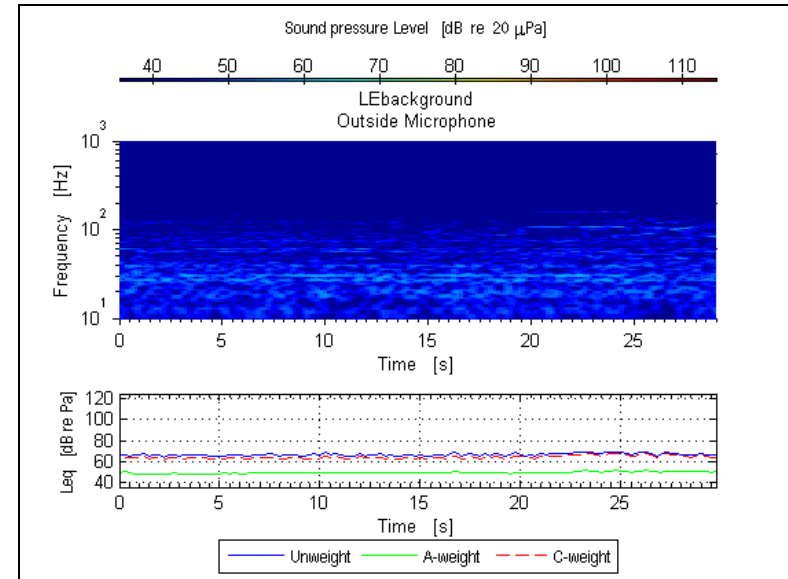


Figure A.2: Outdoor mic measuring background noise

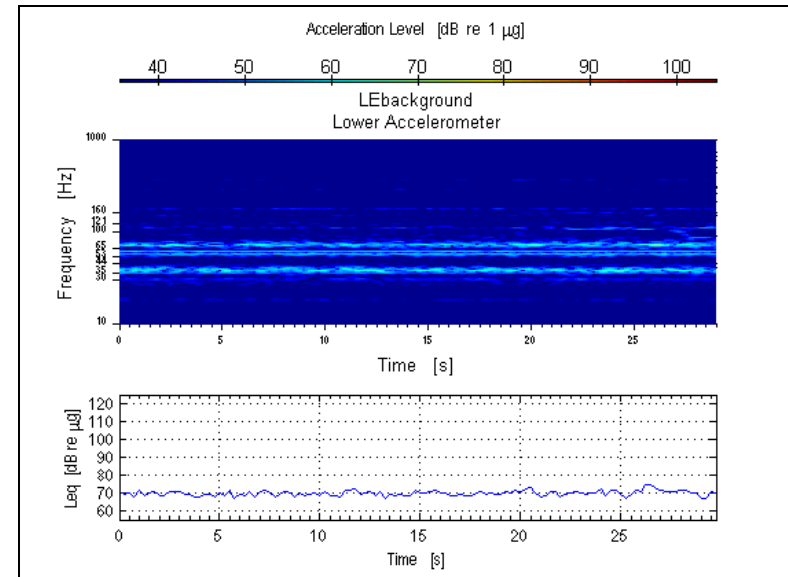


Figure A.3: Accelerometer measuring background noise

6.1.a.ii Aircraft take-off playback, Lower East (LE) window

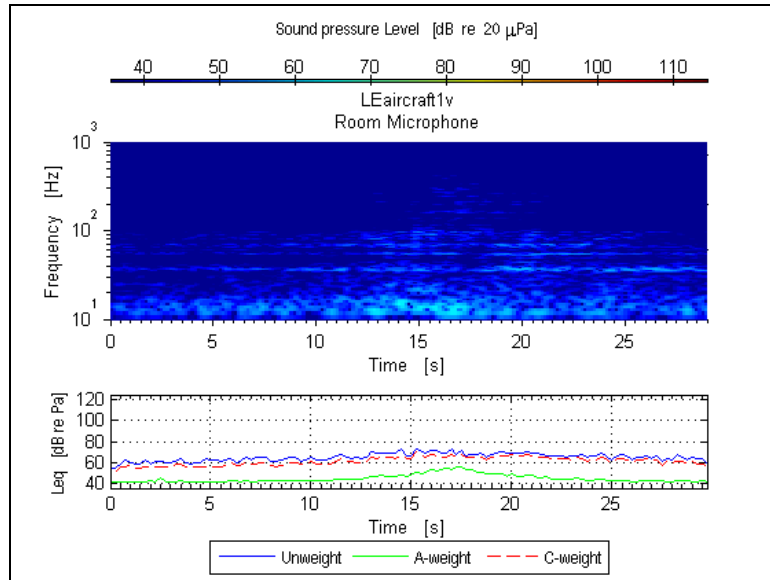


Figure A.4: Room mic measuring aircraft take-off, (70 dBC at window)

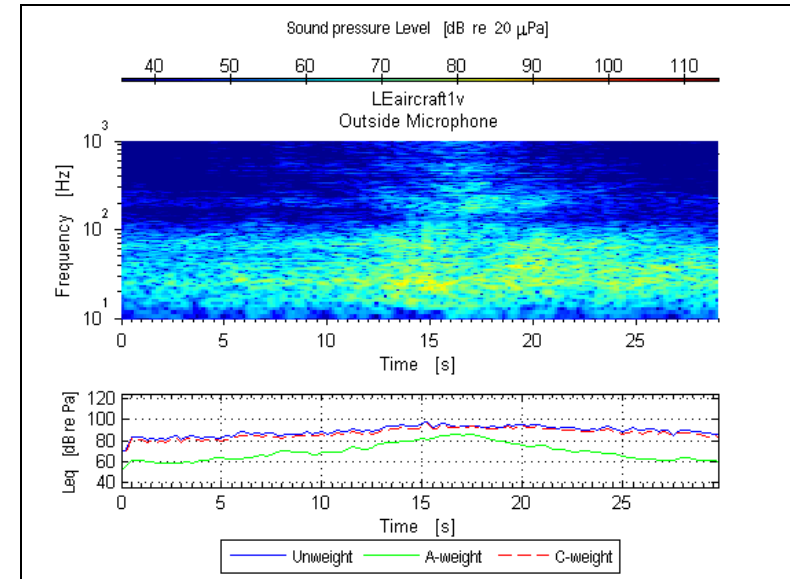


Figure A.5: Outdoor mic measuring aircraft take-off, (70 dBC at window)

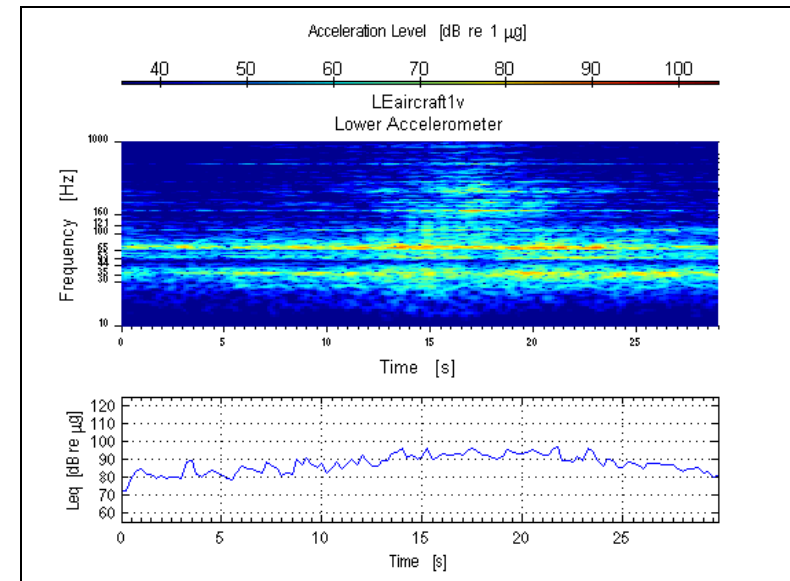


Figure A.6: Accelerometer measuring aircraft take-off, (70 dBC at window)

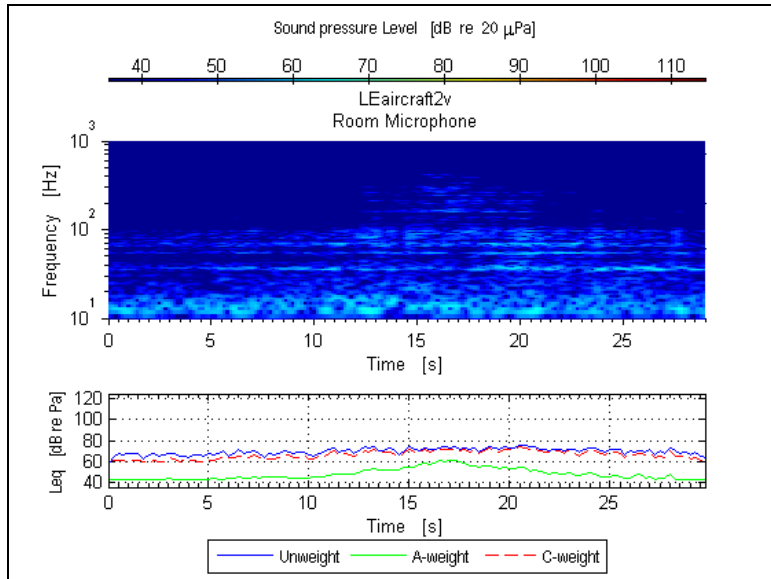


Figure A.7: Room mic measuring aircraft take-off, (80 dBC at window)

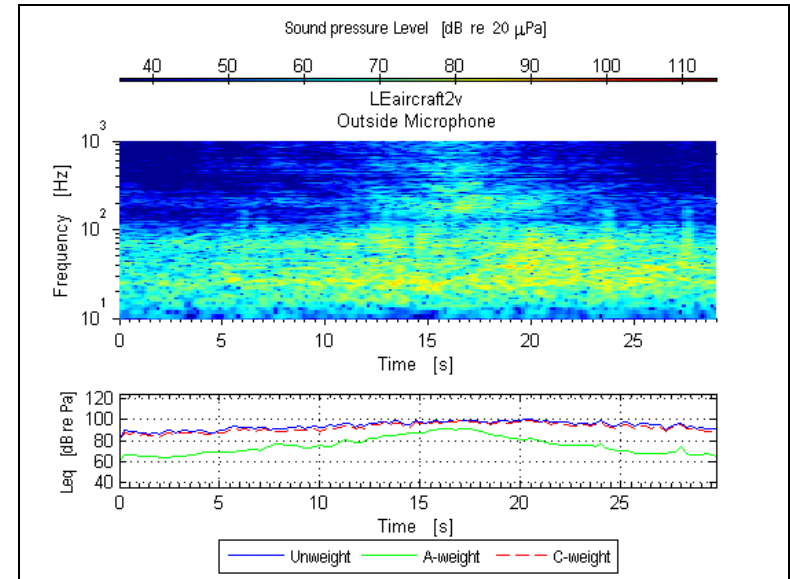


Figure A.8: Outdoor mic measuring aircraft take-off, (80 dBC at window)

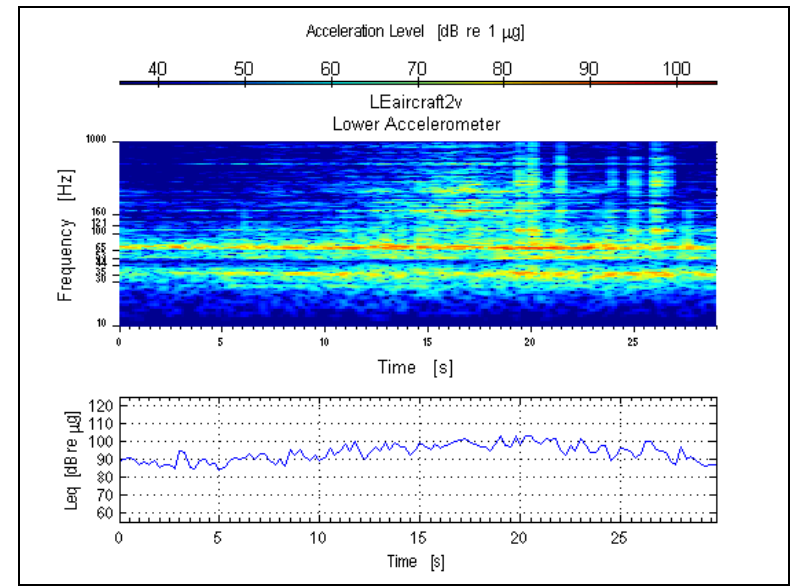


Figure A.9: Accelerometer measuring aircraft take-off, (80 dBC at window)

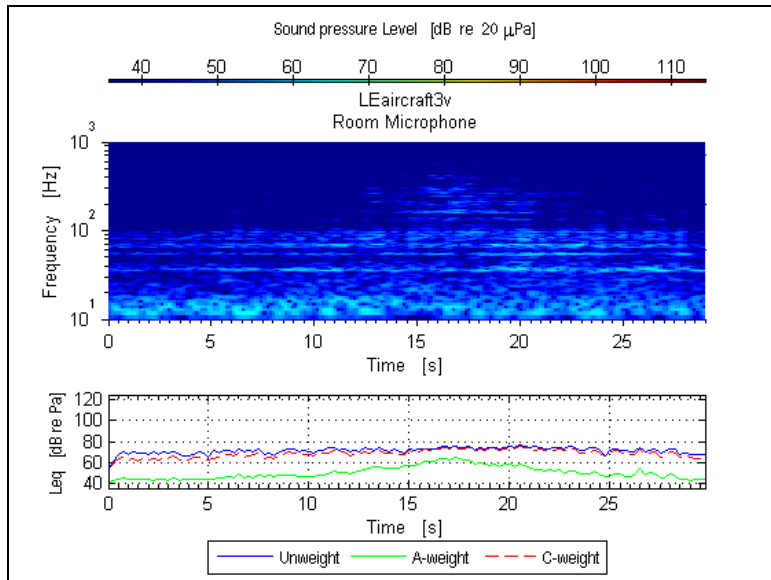


Figure A.10: Room mic measuring aircraft take-off, (90 dBC at window)

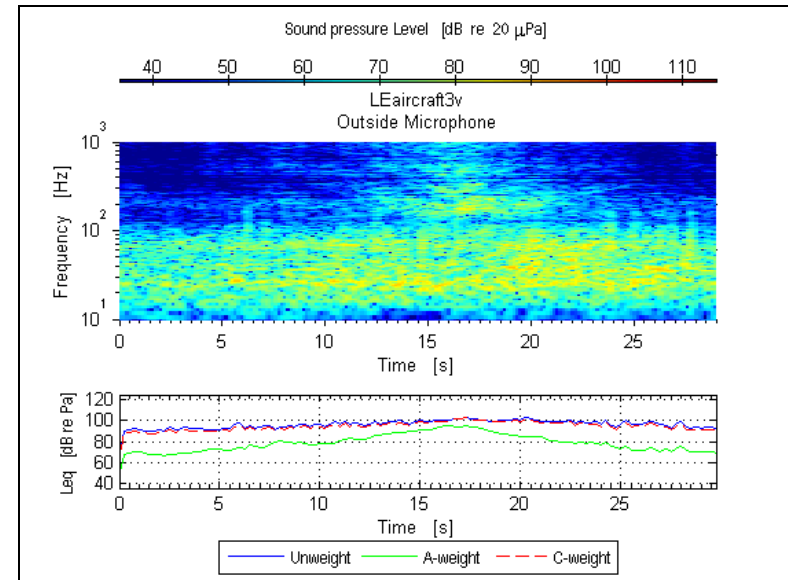


Figure A.11: Outdoor mic measuring aircraft take-off, (90 dBC at window)

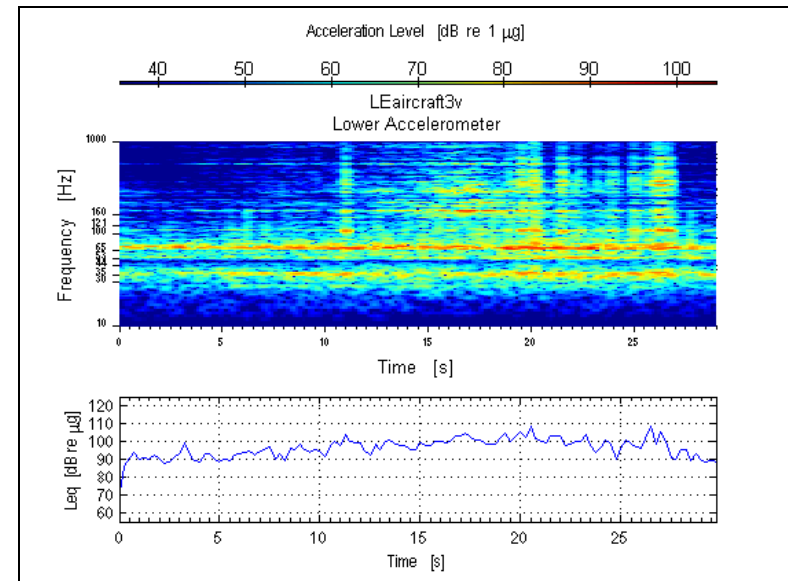


Figure A.12: Accelerometer measuring aircraft take-off, (90 dBC at window)

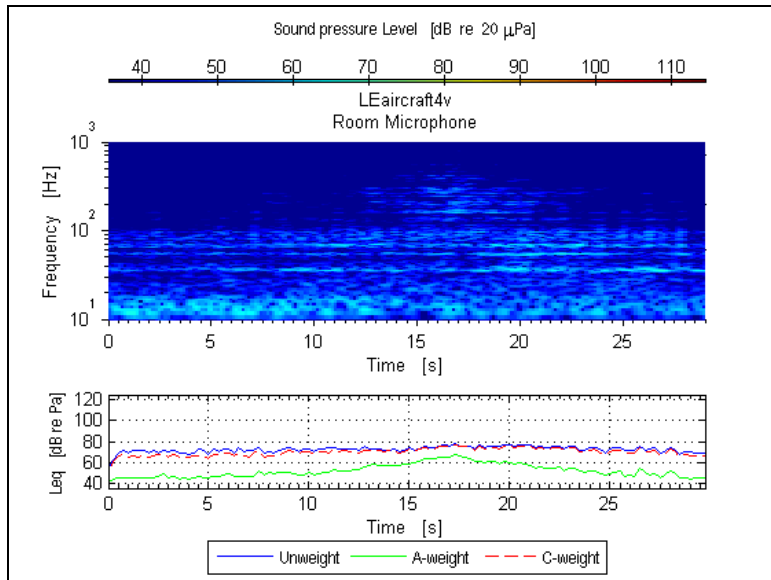


Figure A.13: Room mic measuring aircraft take-off, (100 dBC at window)

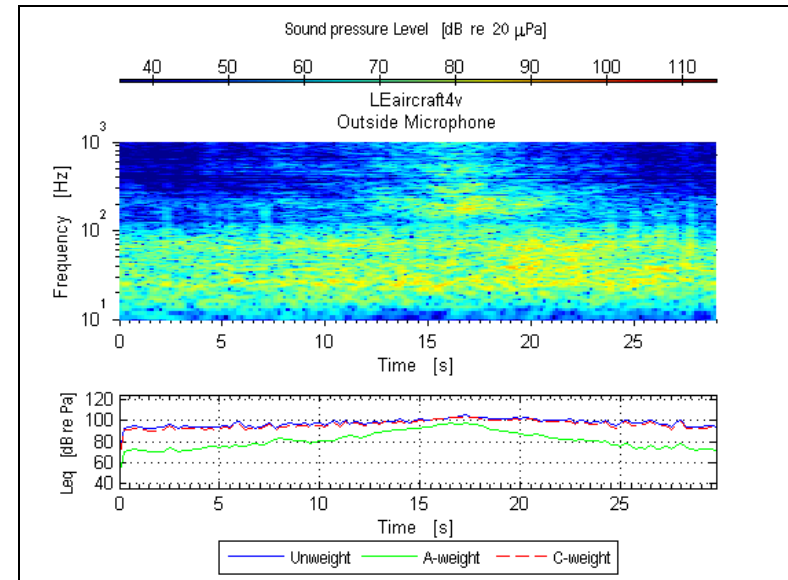


Figure A.14: Outdoor mic measuring aircraft take-off, (100 dBC at window)

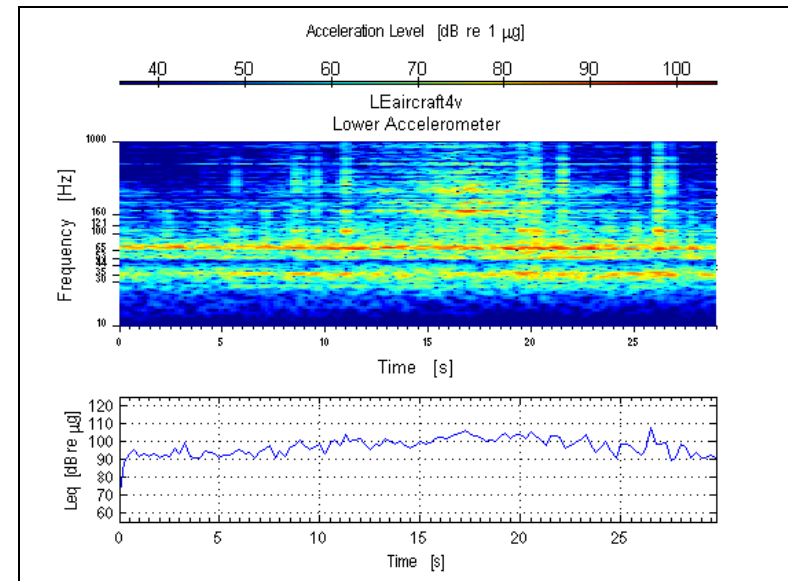


Figure A.15: Accelerometer measuring aircraft take-off, (100 dBC at window)

6.1.a.iii Swept sine, Lower East (LE) window

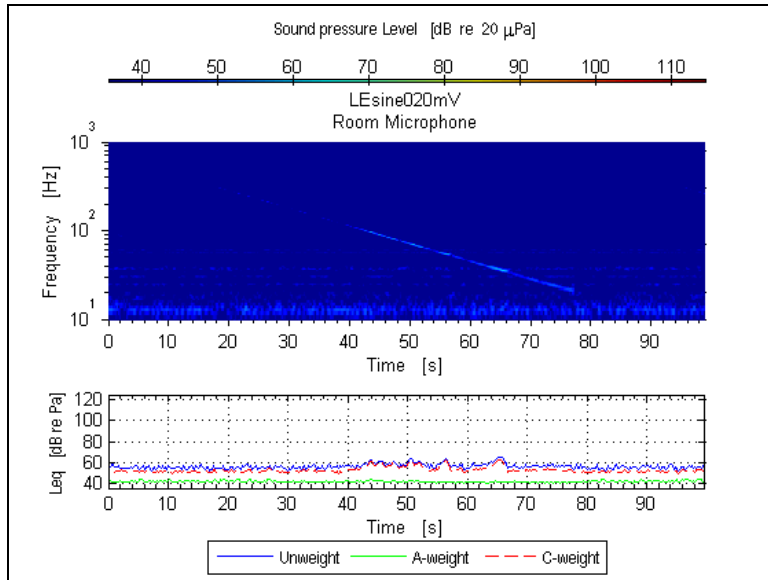


Figure A.16: Room mic measuring swept sine, (70 dBC at window)

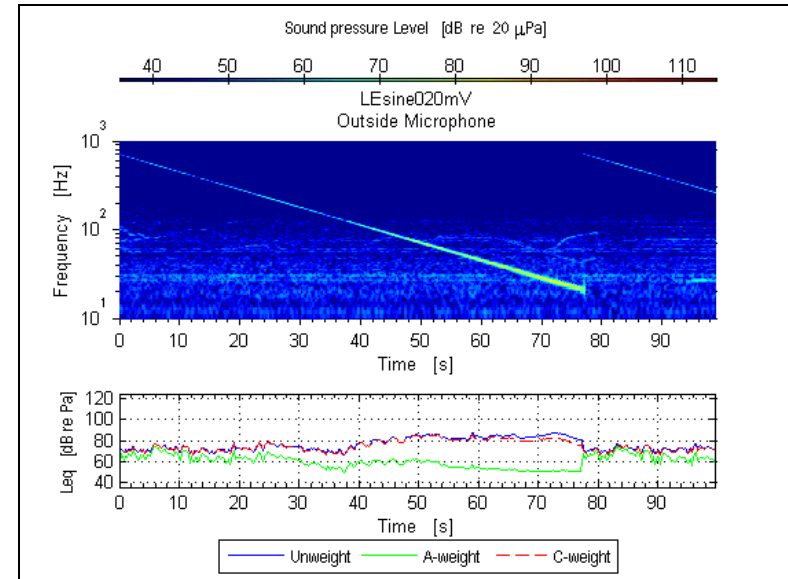


Figure A.17: Outdoor mic measuring swept sine, (70 dBC at window)

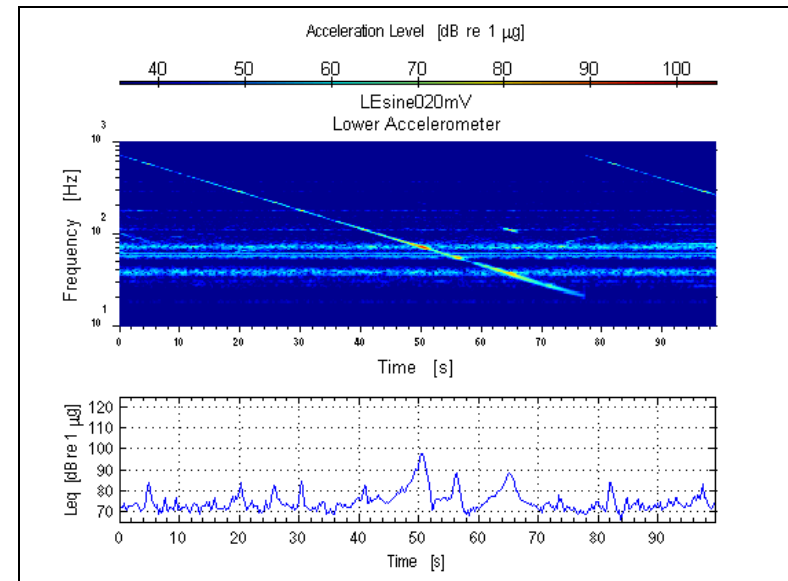


Figure A.18: Accelerometer measuring swept sine, (70 dBC at window)

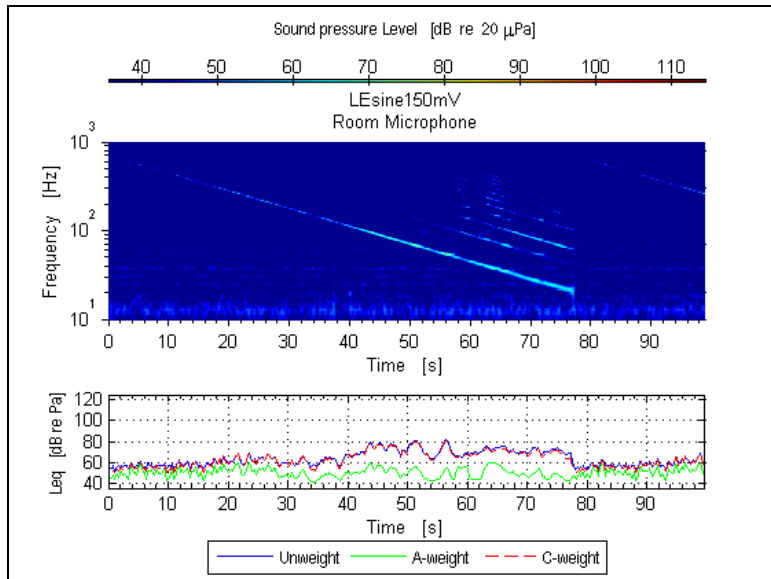


Figure A.19: Room mic measuring swept sine, (80 dBC at window)

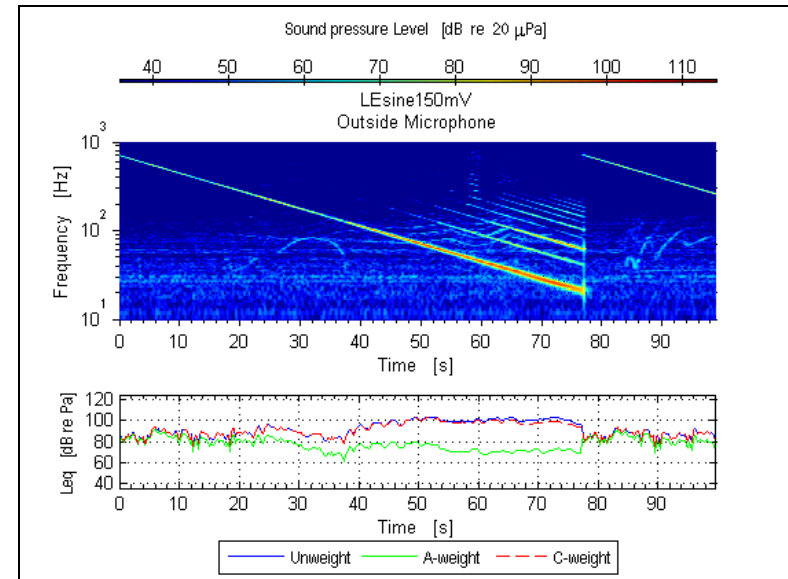


Figure A.20: Outdoor mic measuring swept sine, (80 dBC at window)

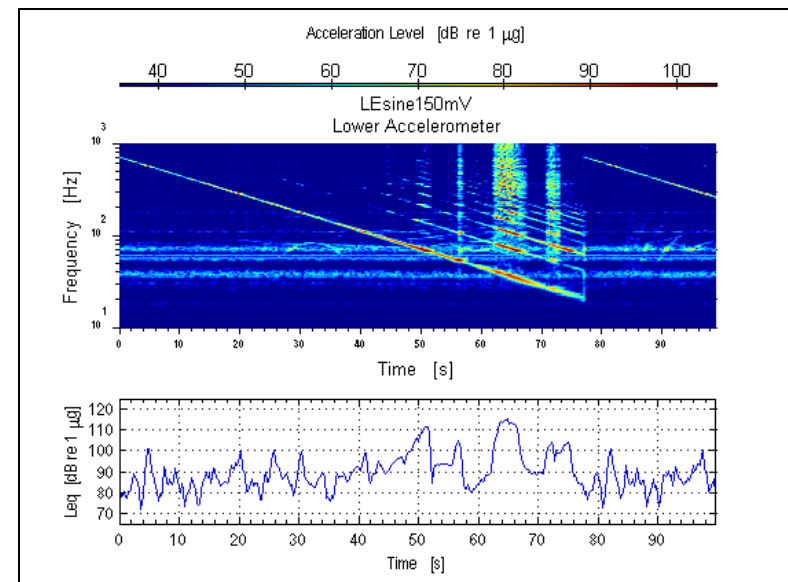


Figure A.21: Accelerometer measuring swept sine, (80 dBC at window)

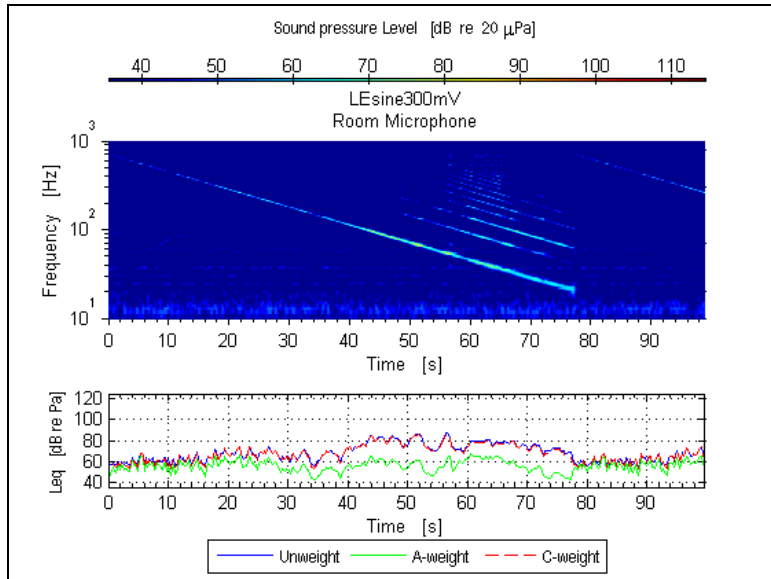


Figure A.22: Room mic measuring swept sine, (90 dBC at window)

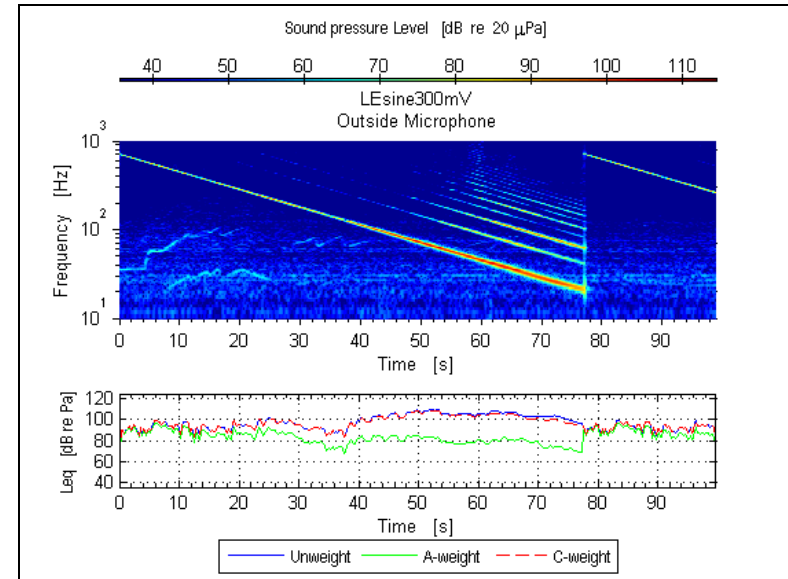


Figure A.23: Outdoor mic measuring swept sine, (90 dBC at window)

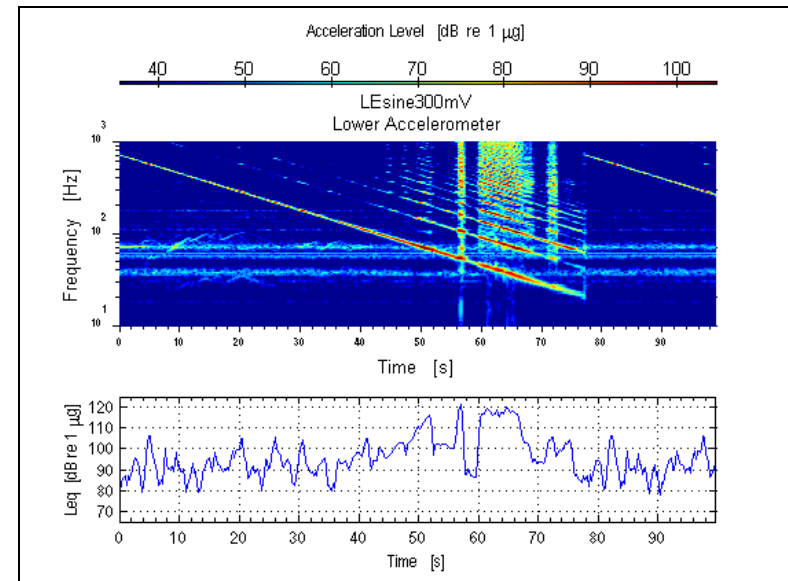


Figure A.24: Accelerometer measuring swept sine, (90 dBC at window)

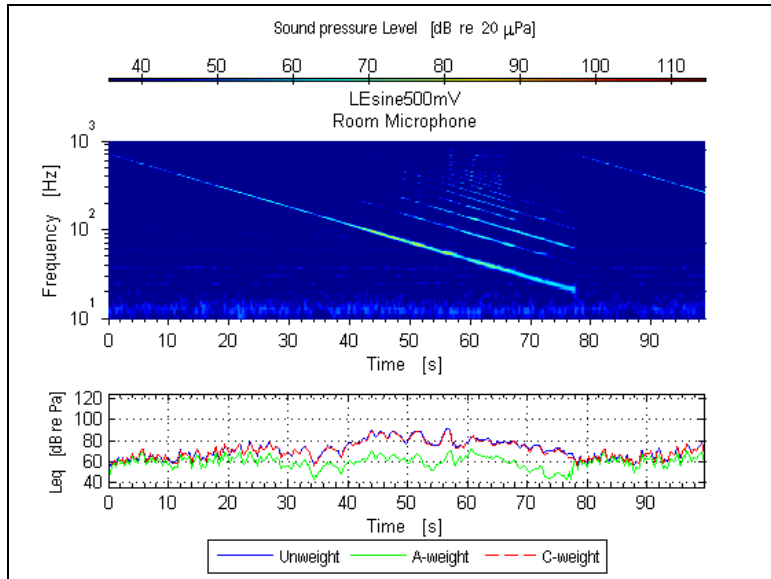


Figure A.25: Room mic measuring swept sine, (100 dBC at window)

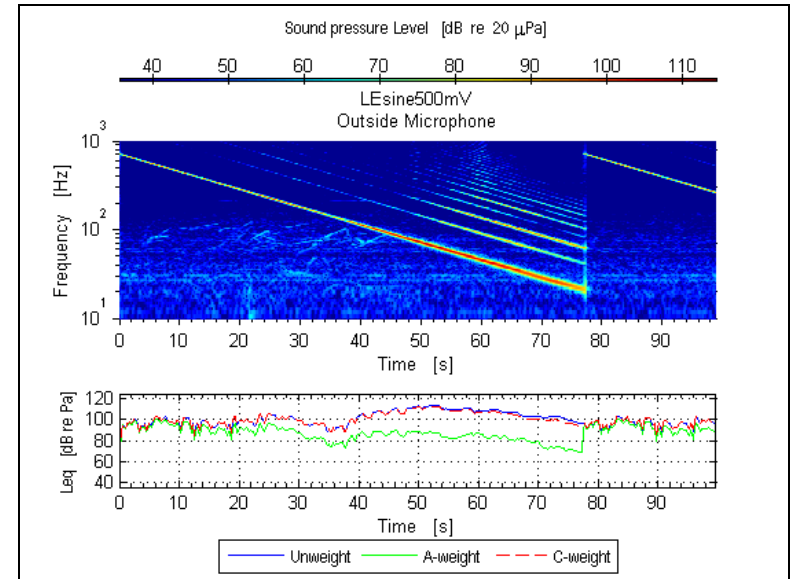


Figure A.26: Outdoor mic measuring swept sine, (100 dBC at window)

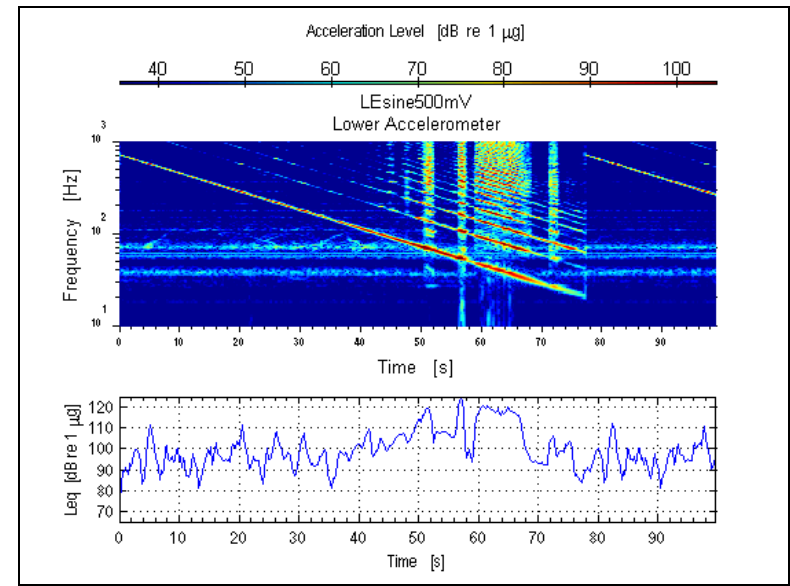


Figure A.27: Accelerometer measuring swept sine, (100 dBC at window)

6.1.a.iv Random noise signal, Lower East (LE) window

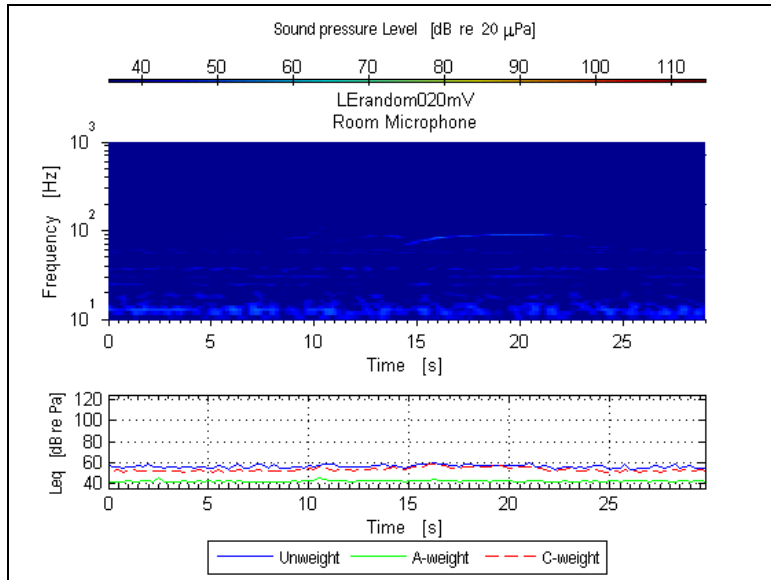


Figure A.28: Room mic measuring random noise, (70 dBC at window)

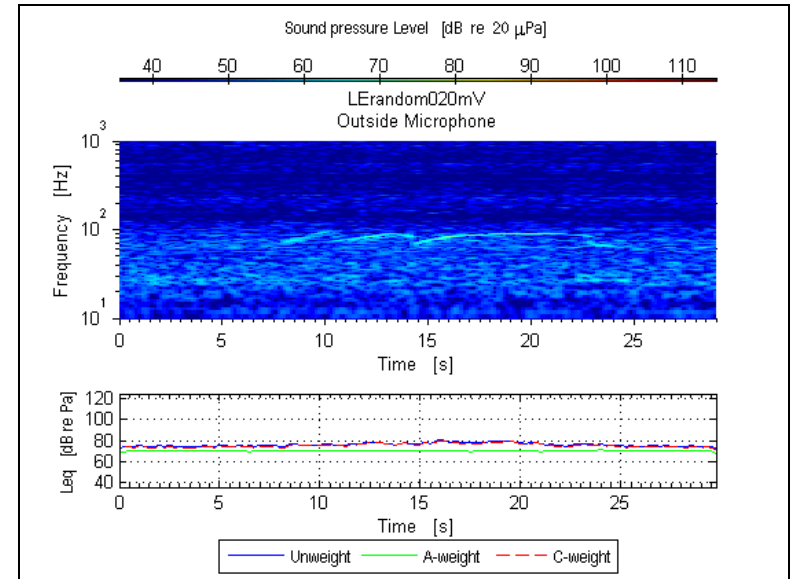


Figure A.29: Outdoor mic measuring random noise, (70 dBC at window)

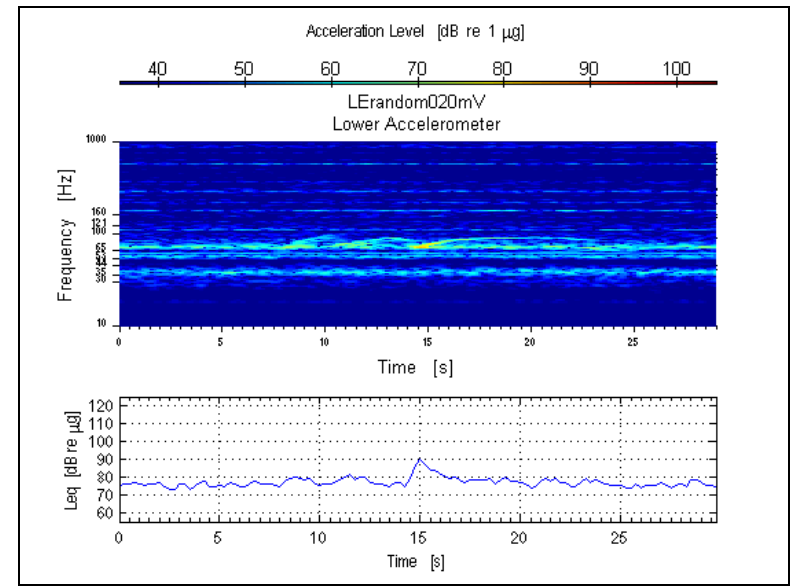


Figure A.30: Accelerometer measuring random noise, (70 dBC at window)

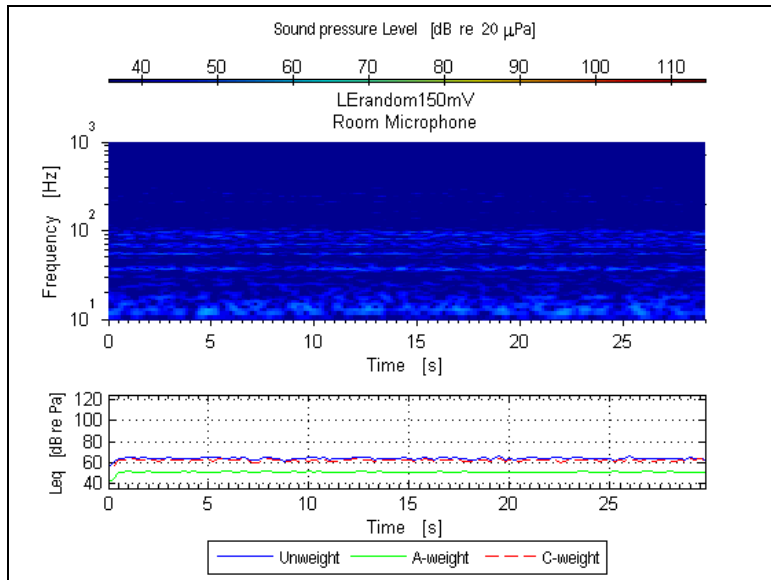


Figure A.31: Room mic measuring random noise, (80 dBC at window)

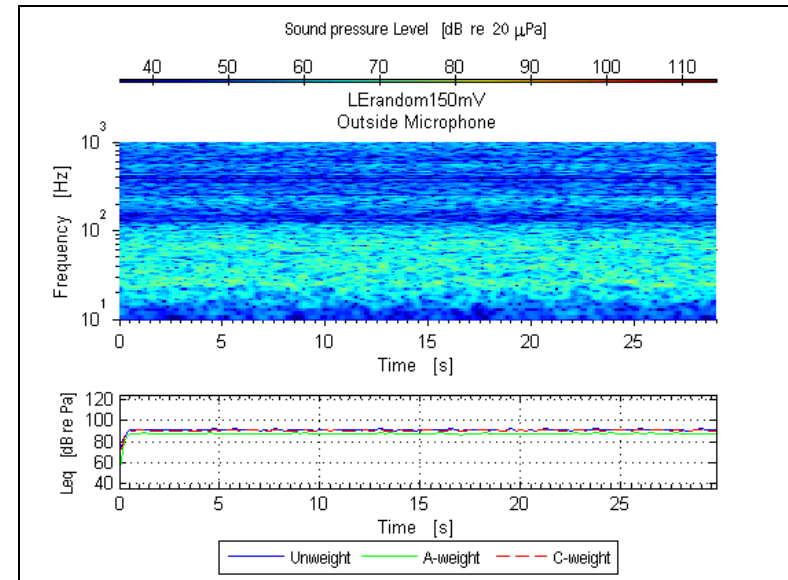


Figure A.32: Outdoor mic measuring random noise, (80 dBC at window)

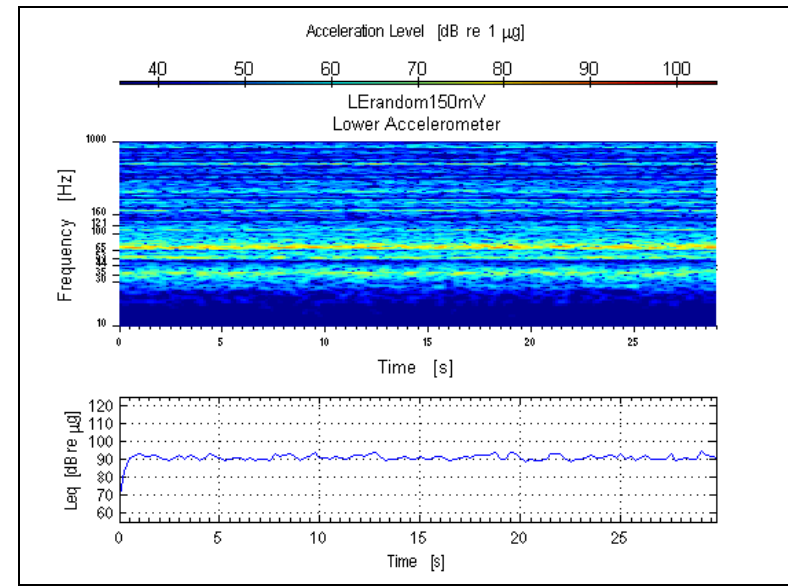


Figure A.33: Accelerometer measuring random noise, (80 dBC at window)

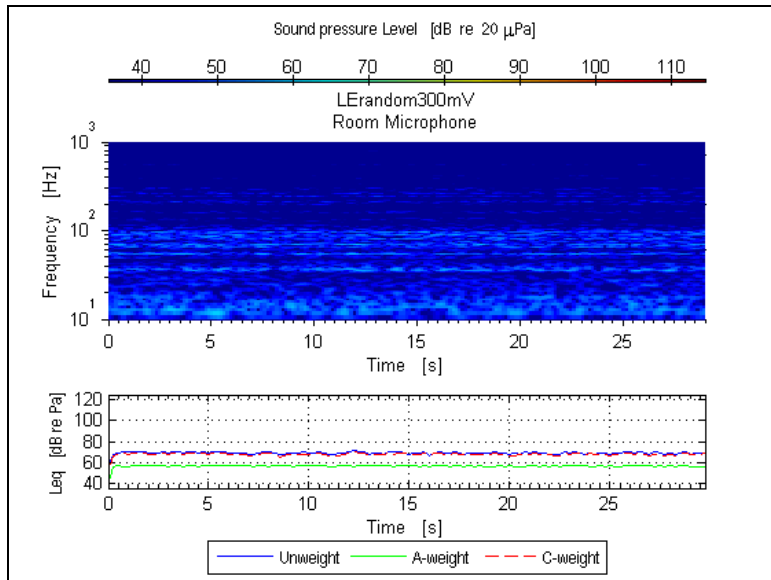


Figure A.34: Room mic measuring random noise, (90 dBC at window)

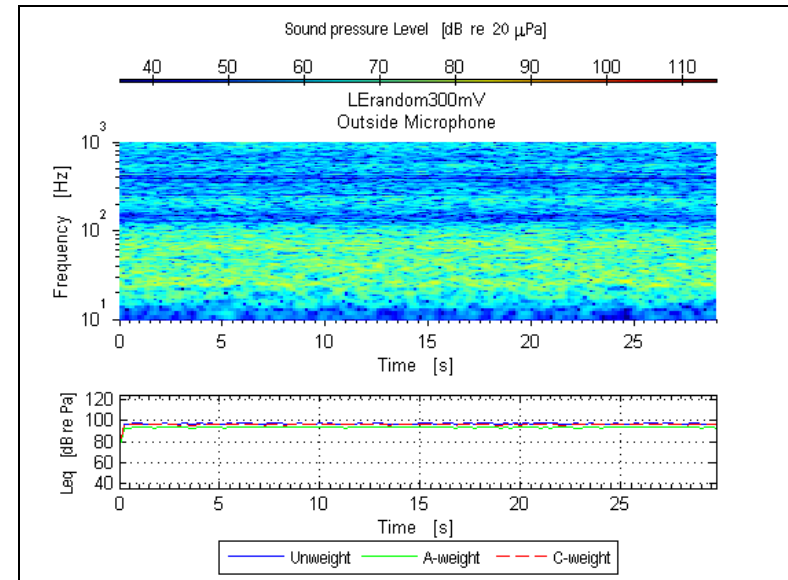


Figure A.35: Outdoor mic measuring random noise, (90 dBC at window)

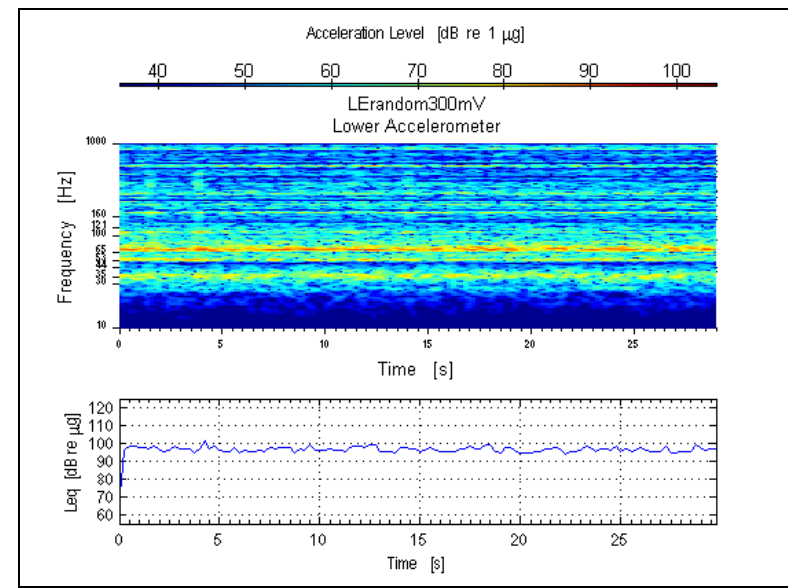


Figure A.36: Accelerometer measuring random noise, (90 dBC at window)

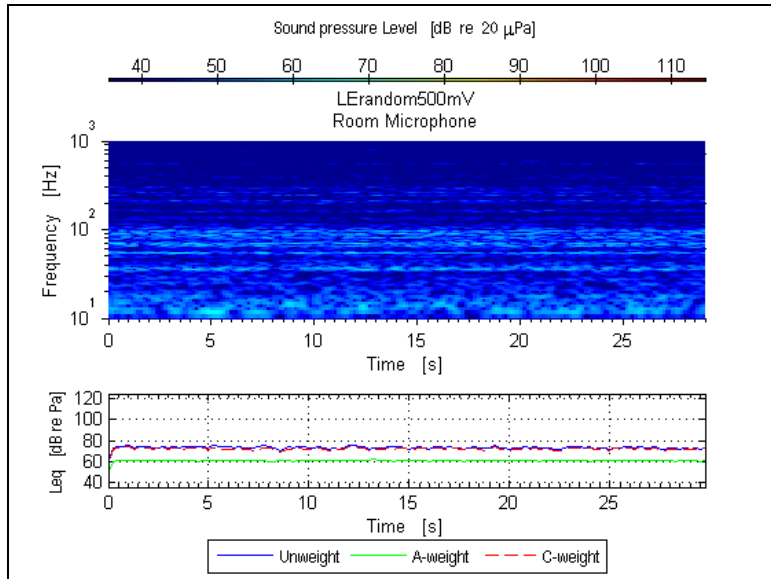


Figure A.37: Room mic measuring random noise, (100 dBC at window)

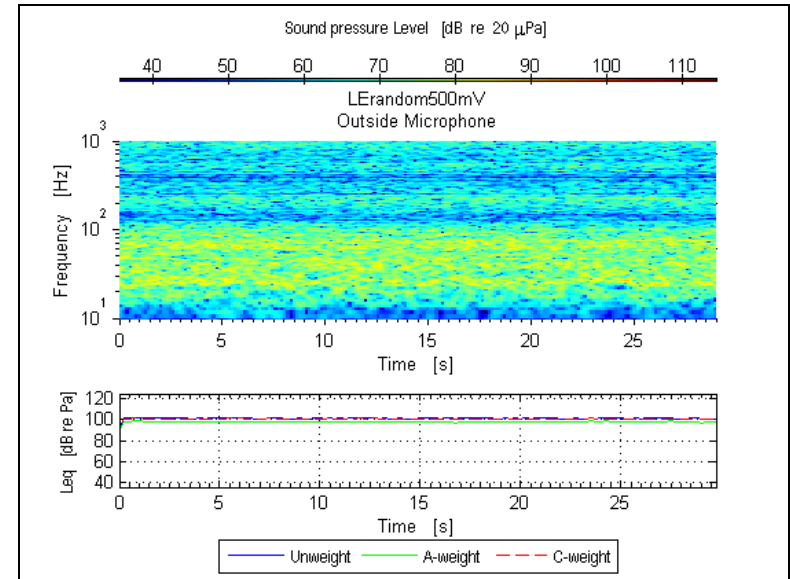


Figure A.38: Outdoor mic measuring random noise, (100 dBC at window)

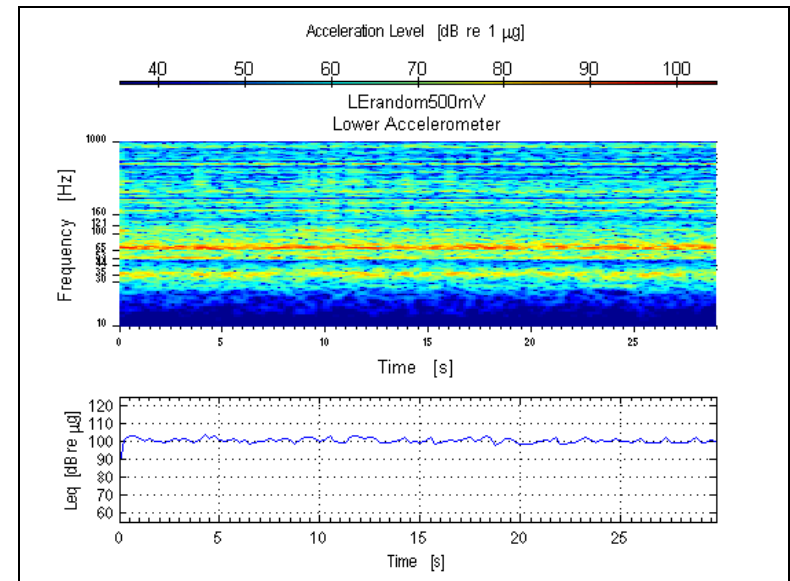


Figure A.39: Accelerometer measuring random noise, (100 dBC at window)

6.1.b Plots of Lower West (LW) window

6.1.b.i Background noise on Lower West (LW) window

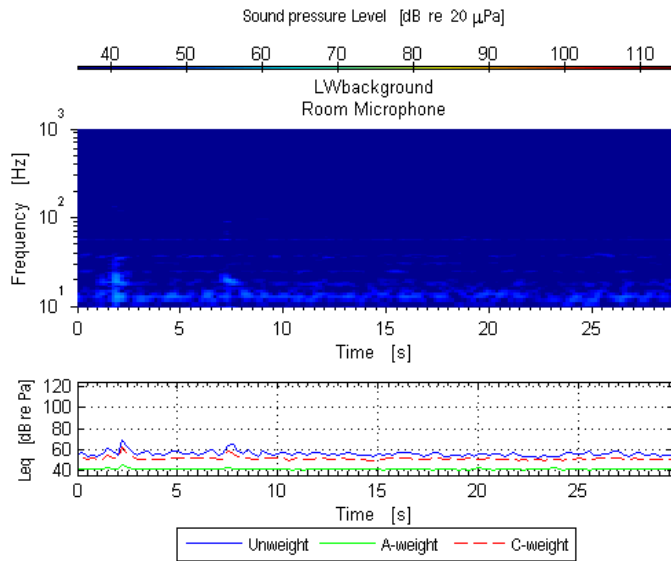


Figure A.40: Room mic measuring background noise

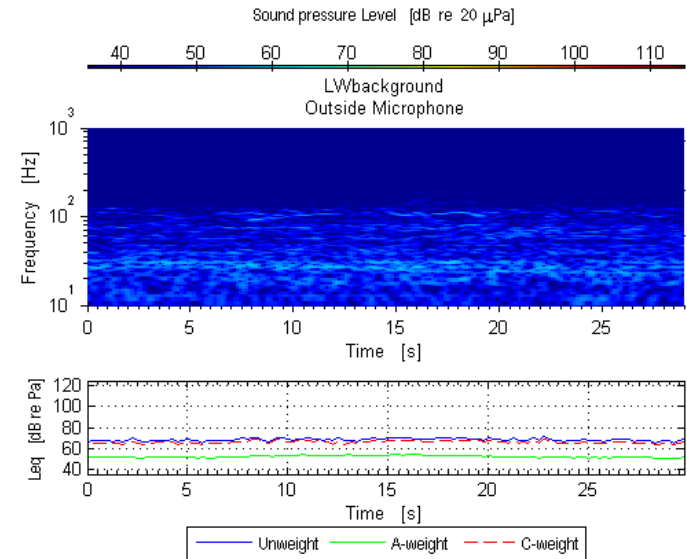


Figure A.41: Outdoor mic measuring background noise

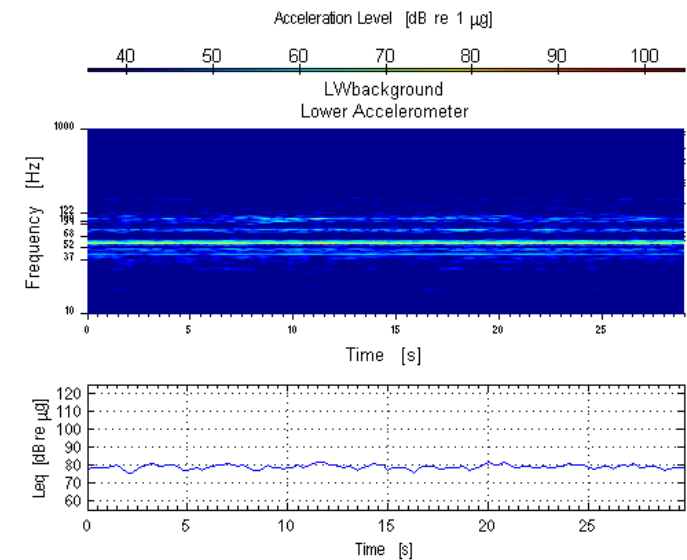


Figure A.42: Accelerometer measuring background noise

6.1.b.ii Aircraft take-off playback, Lower West (LW) window

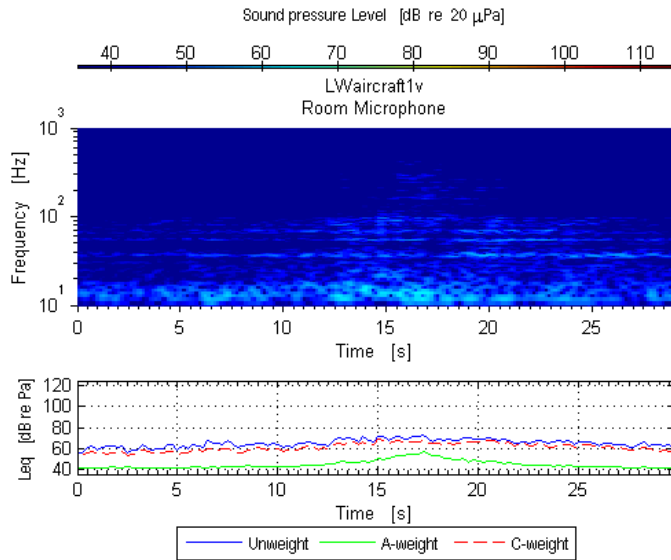


Figure A.43: Room mic measuring aircraft take-off, (70 dBC at window)

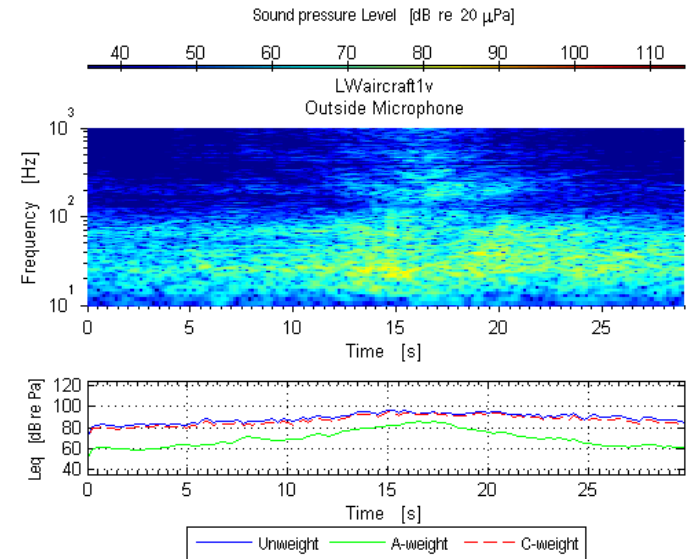


Figure A.44: Outdoor mic measuring aircraft take-off, (70 dBC at window)

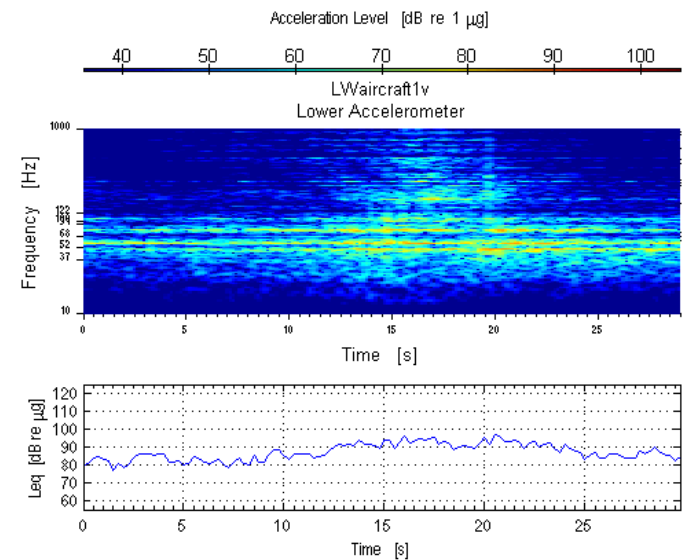


Figure A.45: Accelerometer measuring aircraft take-off, (70 dBC at window)

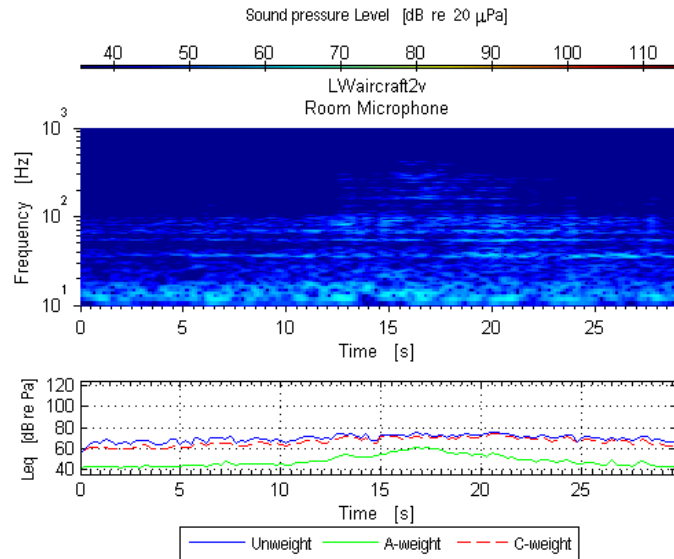


Figure A.46: Room mic measuring aircraft take-off, (80 dBC at window)

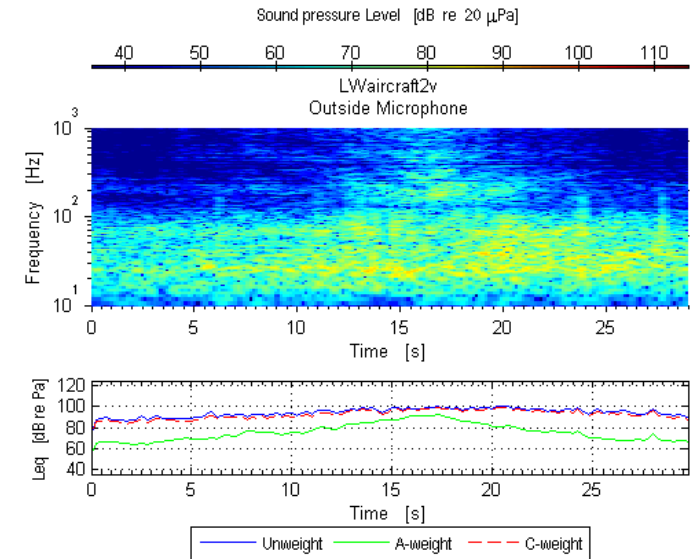


Figure A.47: Outdoor mic measuring aircraft take-off, (80 dBC at window)

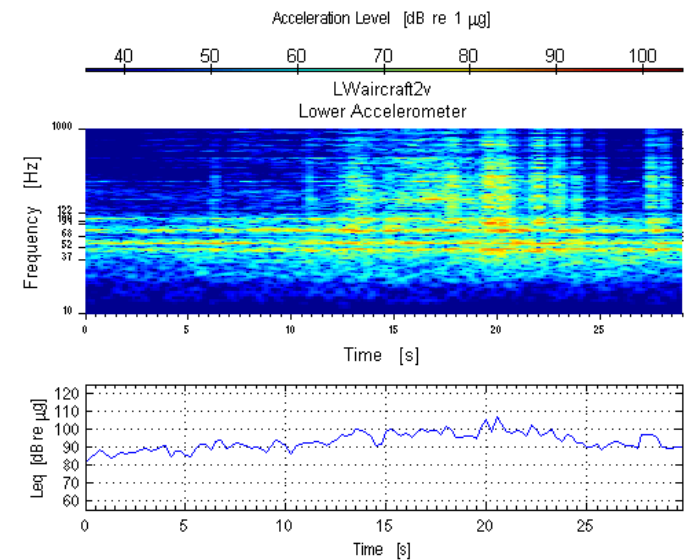


Figure A.48: Accelerometer measuring aircraft take-off, (80 dBC at window)

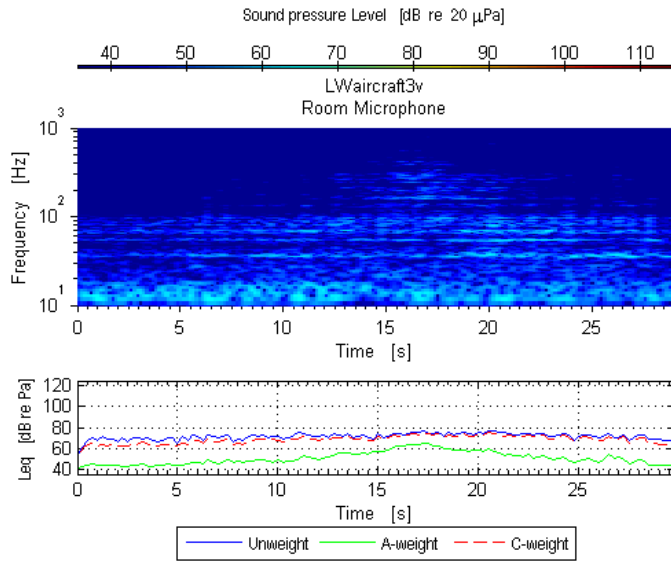


Figure A.49: Room mic measuring aircraft take-off, (90 dBC at window)

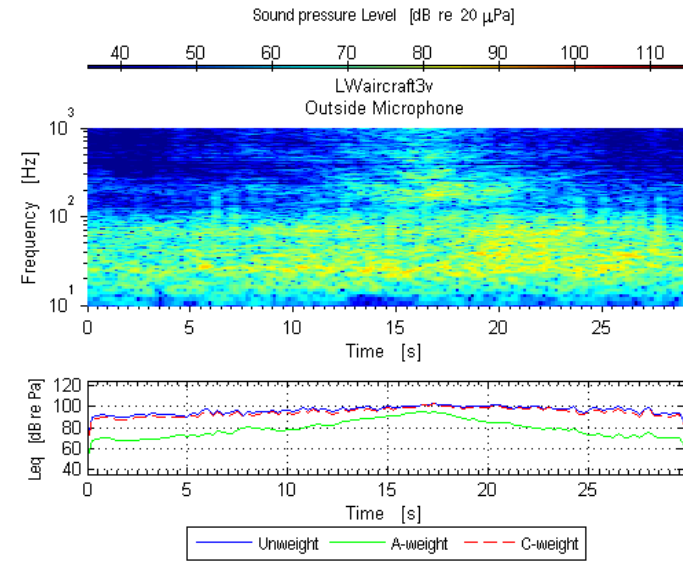


Figure A.50: Outdoor mic measuring aircraft take-off, (90 dBC at window)

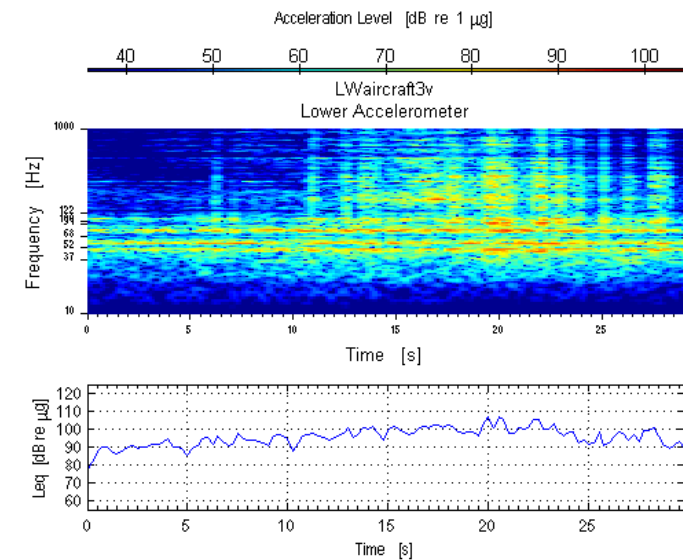


Figure A.51: Accelerometer measuring aircraft take-off, (90 dBC at window)

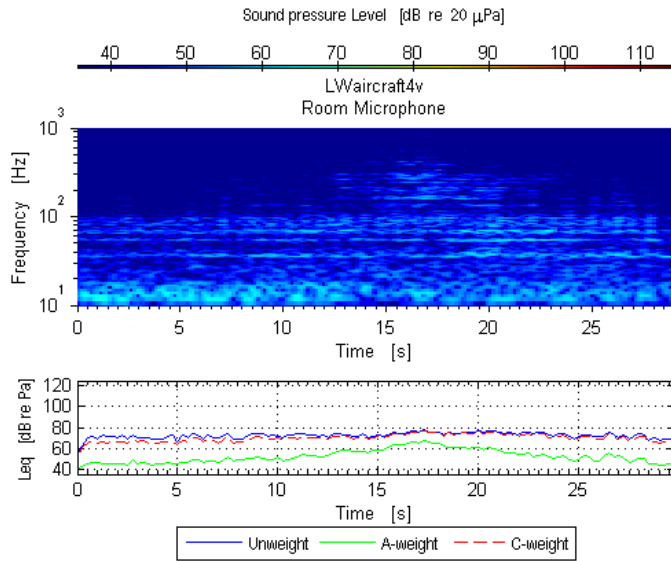


Figure A.52: Room mic measuring aircraft take-off, (100 dBC at window)

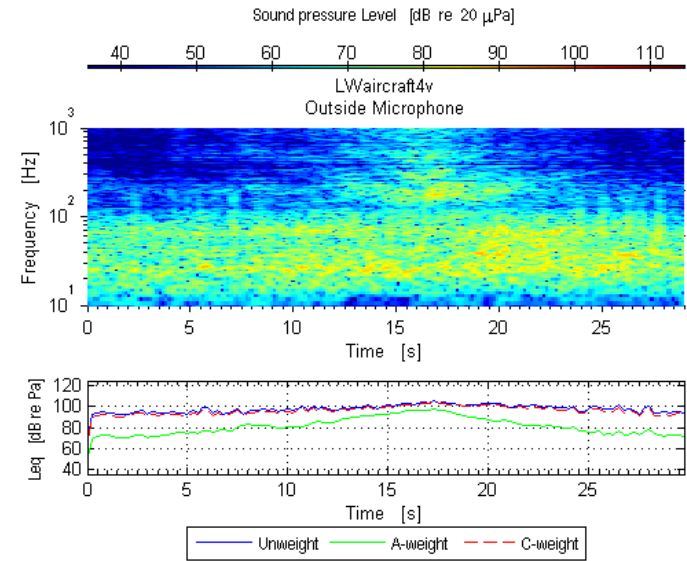


Figure A.53: Outdoor mic measuring aircraft take-off, (100 dBC at window)

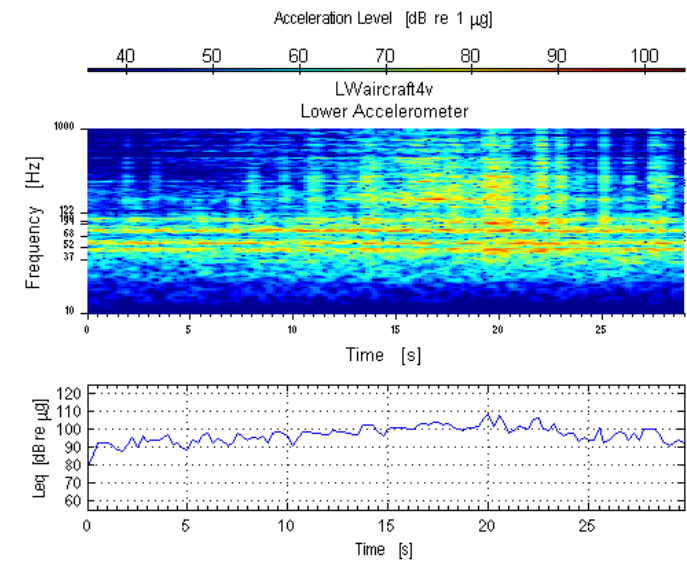


Figure 54: Accelerometer measuring aircraft take-off, (100 dBC at window)

6.1.b.iii Swept sine, Lower West (LW) window

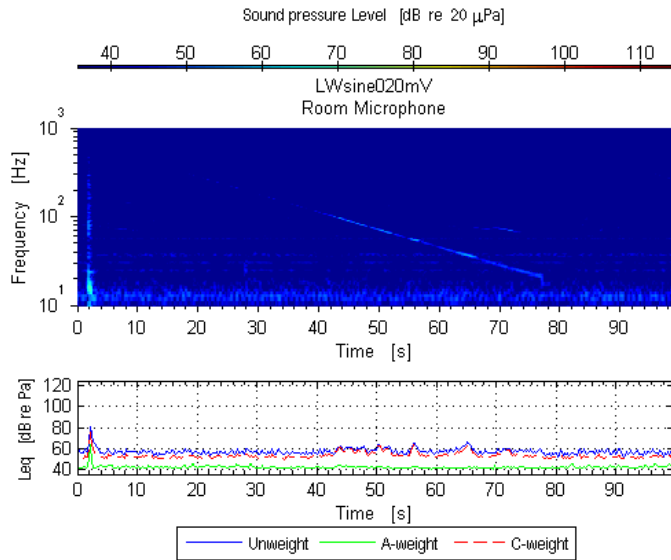


Figure A.55: Room mic measuring swept sine, (70 dBC at window)

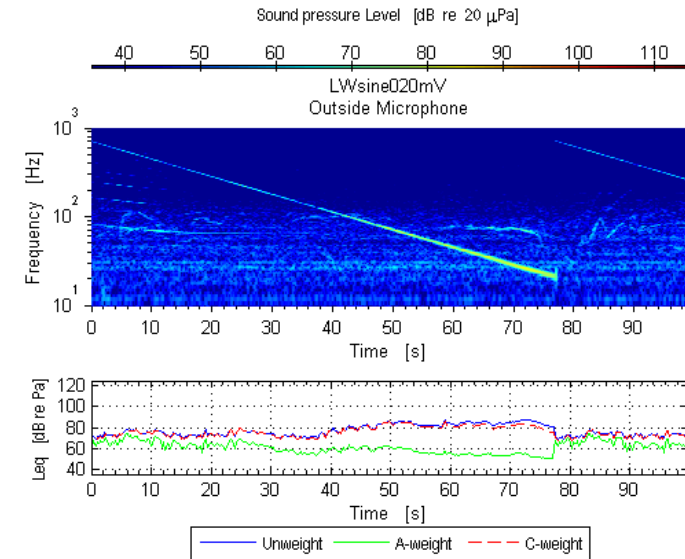


Figure A.56: Outdoor mic measuring swept sine, (70 dBC at window)

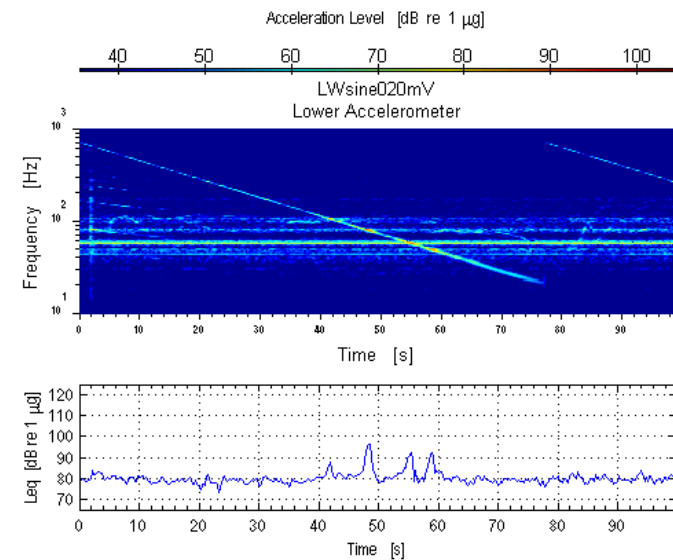


Figure A.57: Accelerometer measuring swept sine, (70 dBC at window)

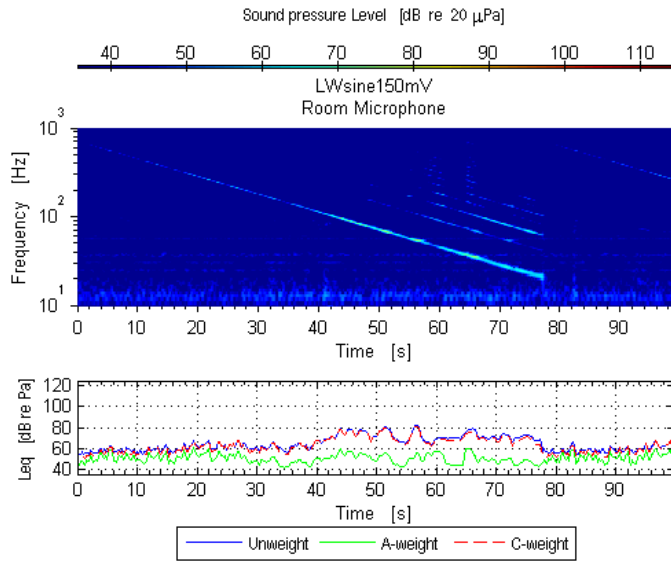


Figure A.58: Room mic measuring swept sine, (80 dBC at window)

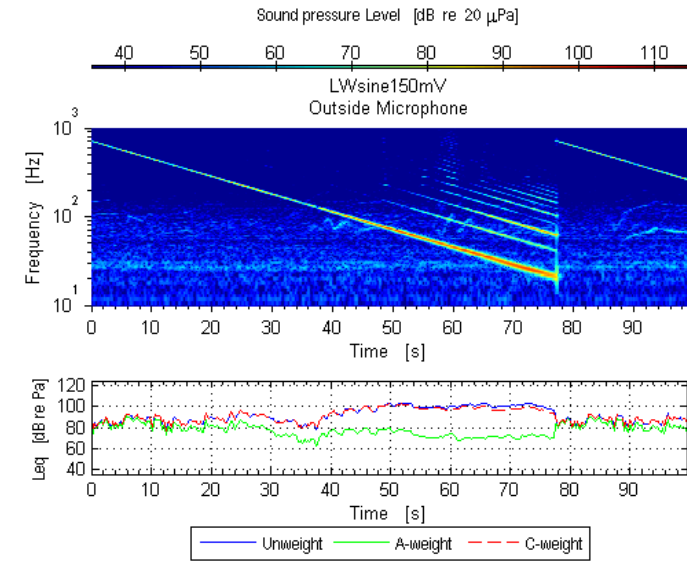


Figure A.59: Outdoor mic measuring swept sine, (80 dBC at window)

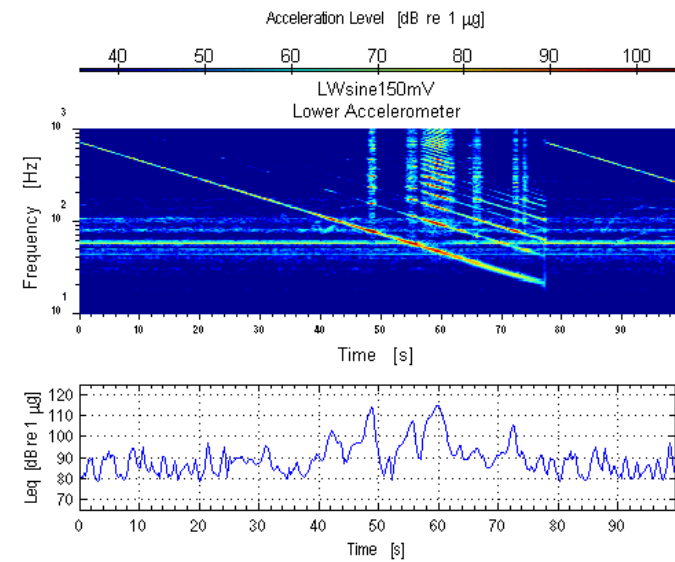


Figure A.60: Accelerometer measuring swept sine, (80 dBC at window)

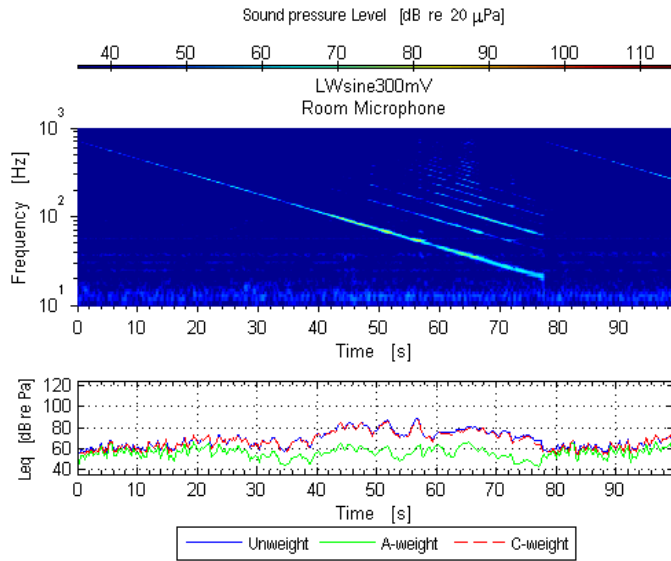


Figure A.61: Room mic measuring swept sine, (90 dBC at window)

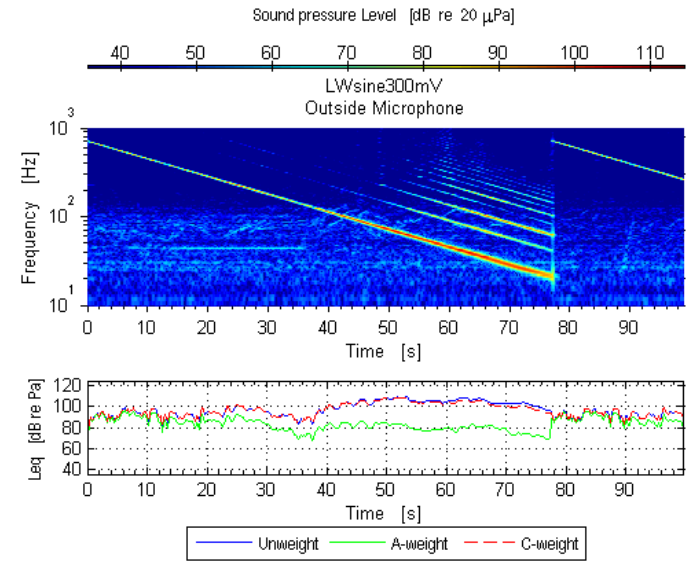


Figure A.62: Outdoor mic measuring swept sine, (90 dBC at window)

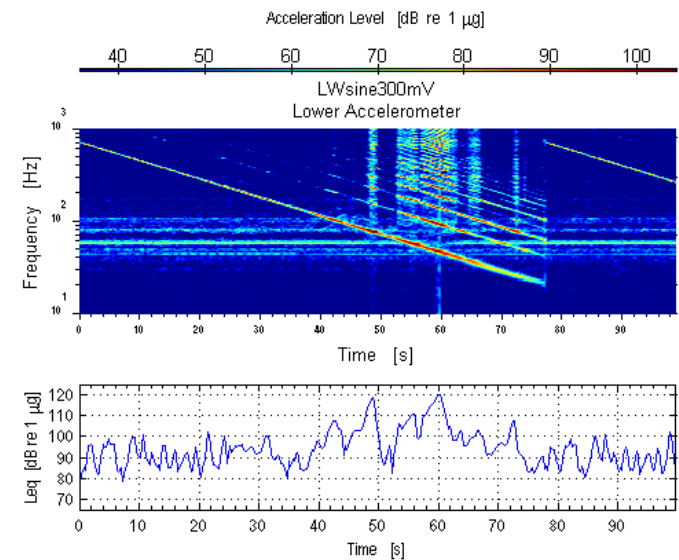


Figure A.63: Accelerometer measuring swept sine, (90 dBC at window)

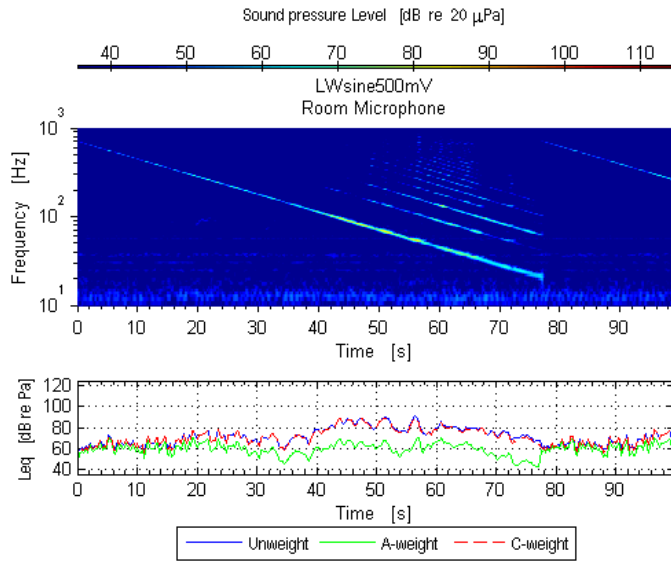


Figure A.64: Room mic measuring swept sine, (100 dBC at window)

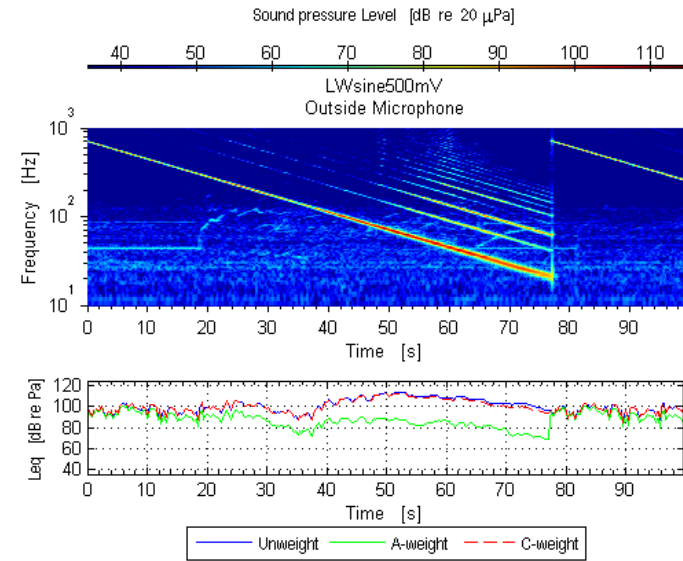


Figure A.65: Outdoor mic measuring swept sine, (100 dBC at window)

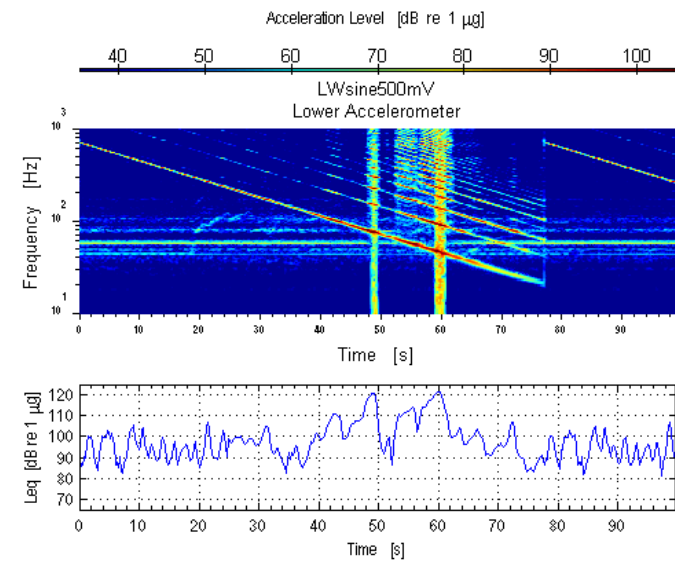


Figure A.66: Accelerometer measuring swept sine, (100 dBC at window)

6.1.b.iv Random noise signal, Lower West (LW) window

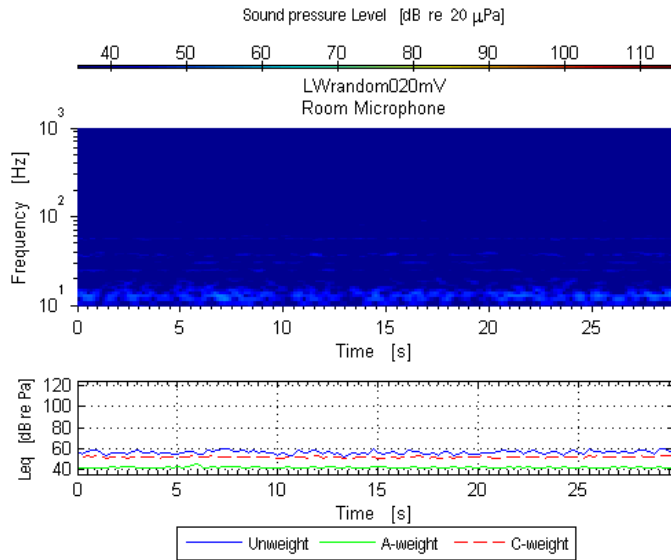


Figure A.67: Room mic measuring random noise, (70 dBC at window)

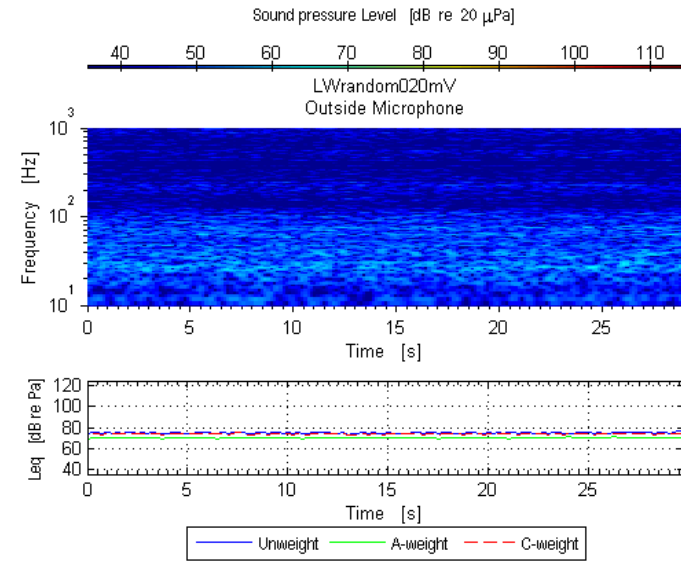


Figure A.68: Outdoor mic measuring random noise, (70 dBC at window)

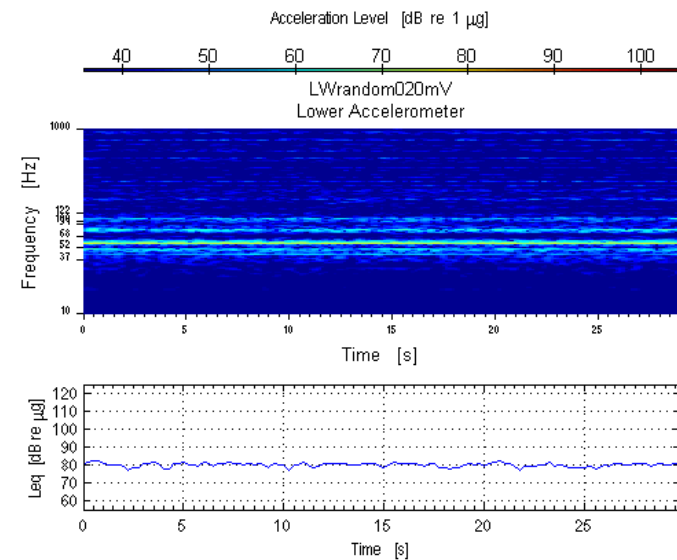


Figure A.69: Accelerometer measuring random noise, (70 dBC at window)

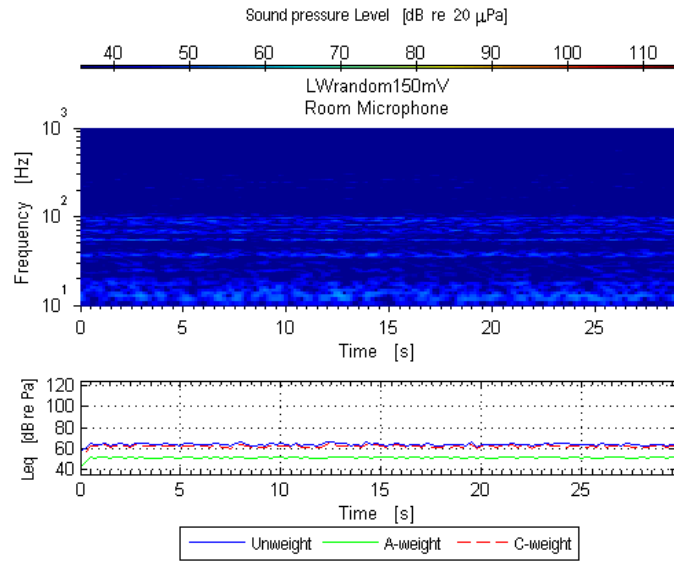


Figure A.70: Room mic measuring random noise, (80 dBC at window)

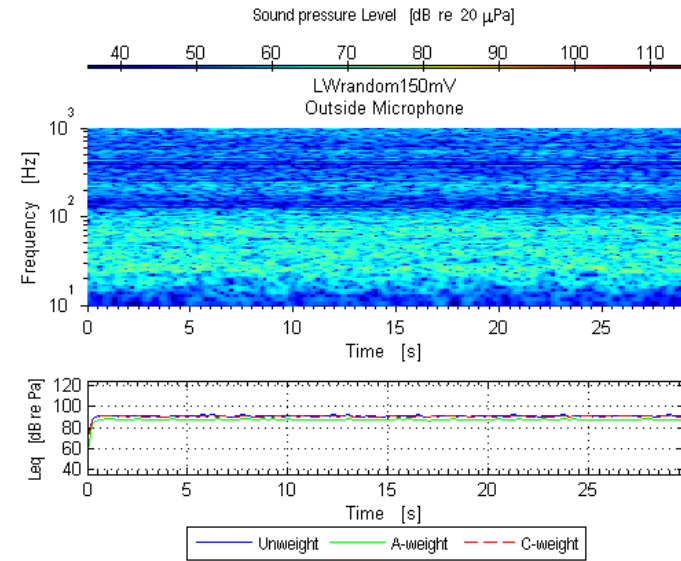


Figure A.71: Outdoor mic measuring random noise, (80 dBC at window)

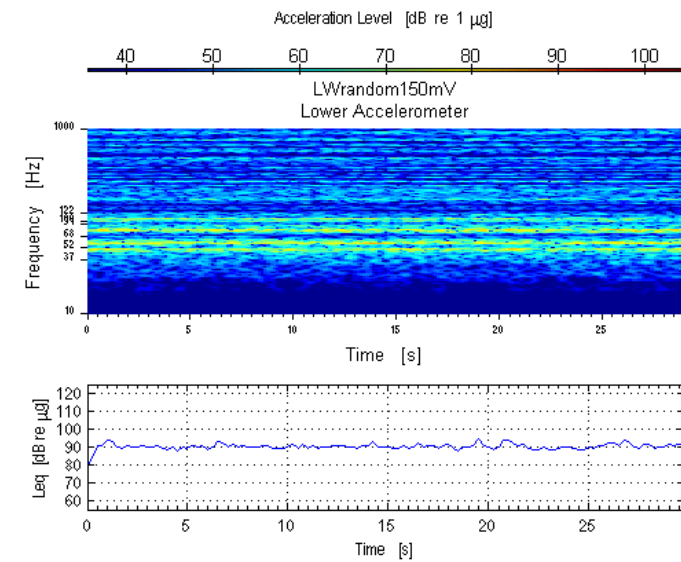


Figure A.72: Accelerometer measuring random noise, (80 dBC at window)

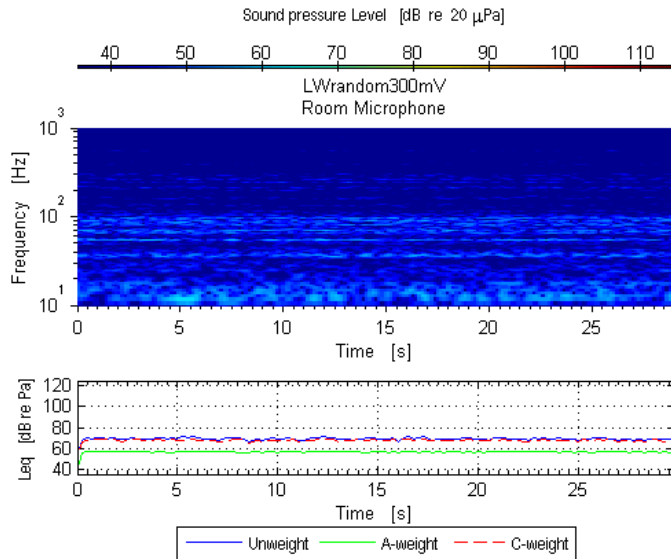


Figure A.73: Room mic measuring random noise, (90 dBC at window)

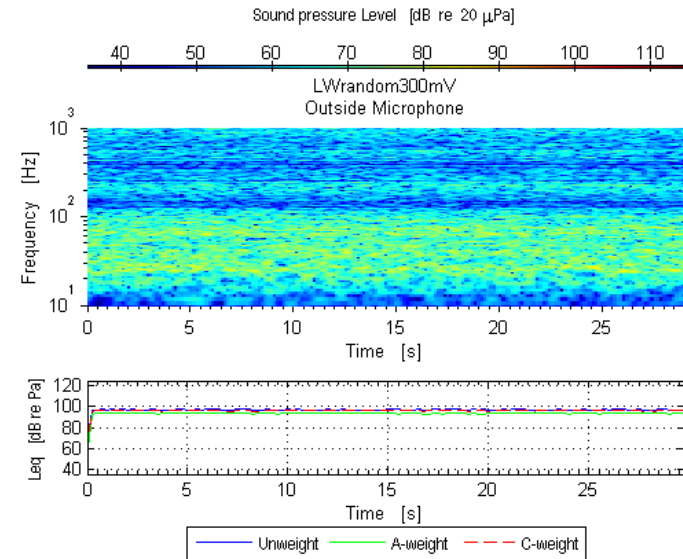


Figure A.74: Outdoor mic measuring random noise, (90 dBC at window)

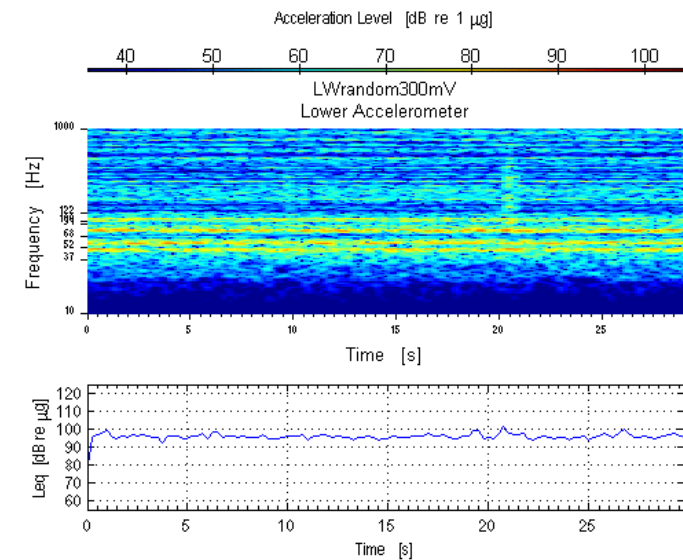


Figure A.75: Accelerometer measuring random noise, (90 dBC at window)

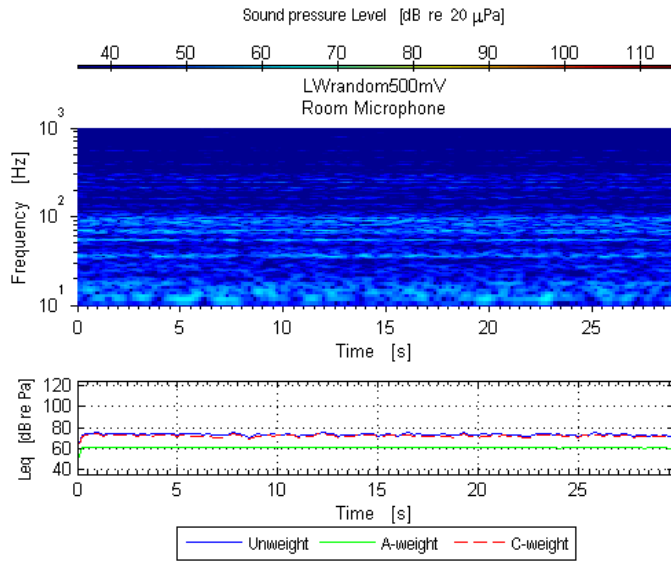


Figure A.76: Room mic measuring random noise, (100 dBC at window)

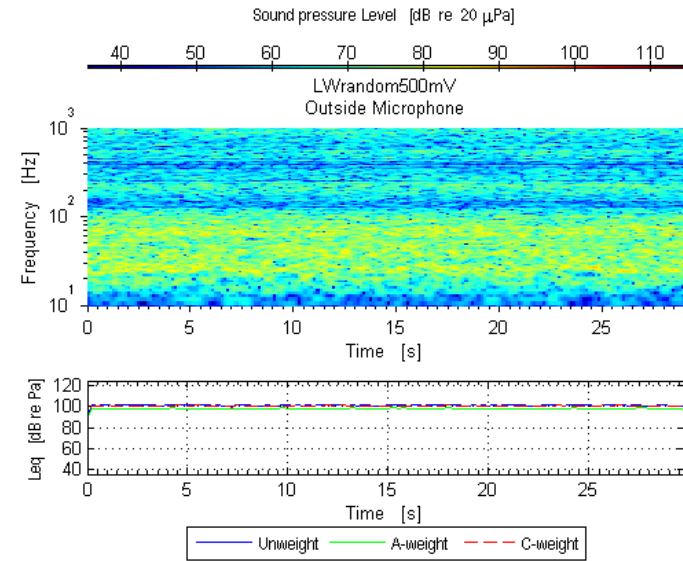


Figure A.77: Outdoor mic measuring random noise, (100 dBC at window)

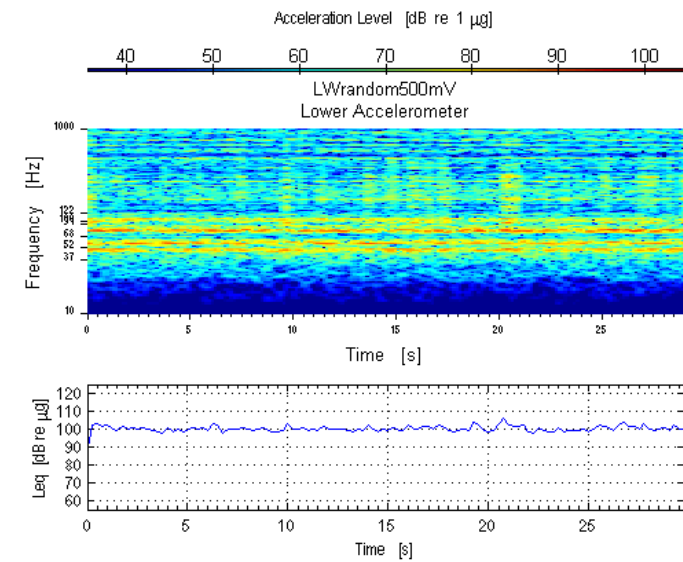


Figure A.78: Accelerometer measuring random noise, (100 dBC at window)

6.1.c Plots of Upper East (UE) window

6.1.c.i Background noise on Upper East (UE) window

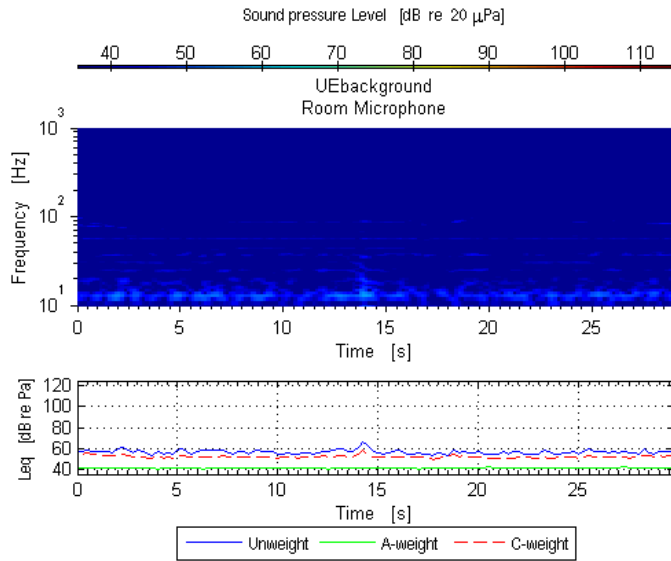


Figure A.79: Room mic measuring background noise

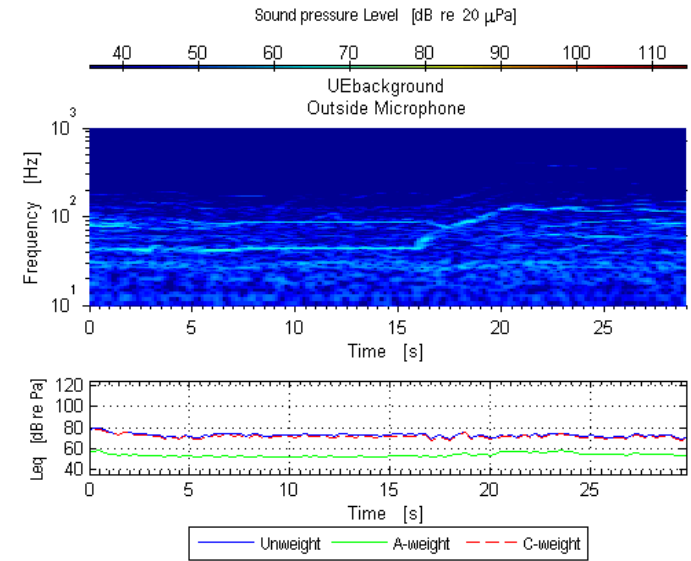


Figure A.80: Outdoor mic measuring background noise

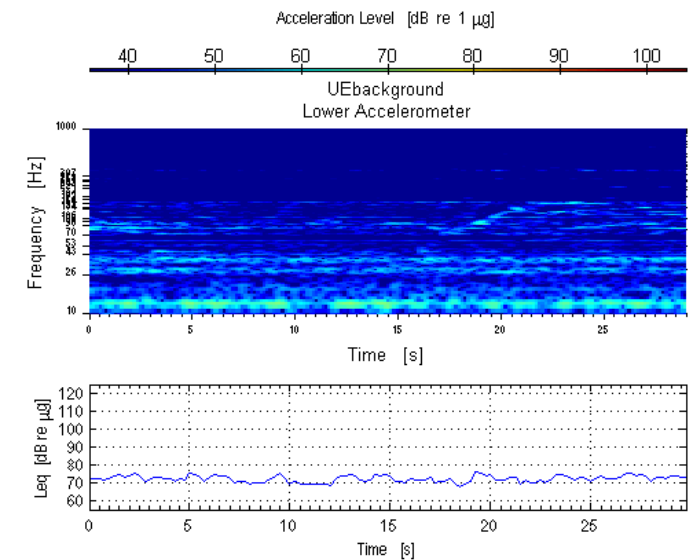


Figure A.81: Accelerometer measuring background noise

6.1.c.ii Aircraft take-off playback, Upper East (UE) window

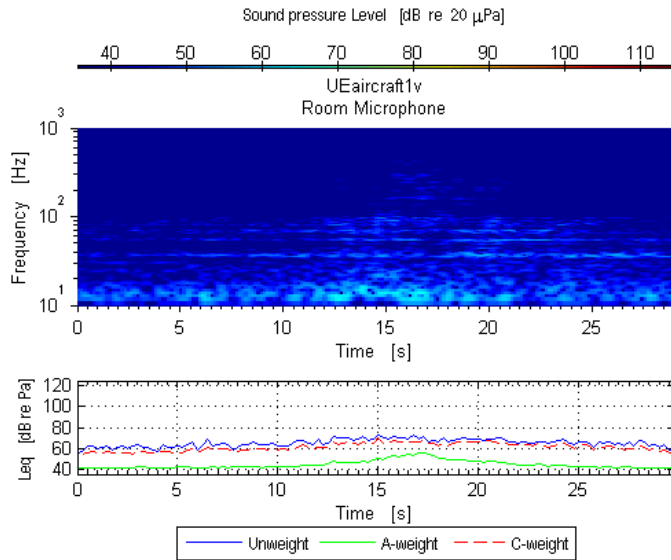


Figure A.82: Room mic measuring aircraft take-off, (70 dBC at window)

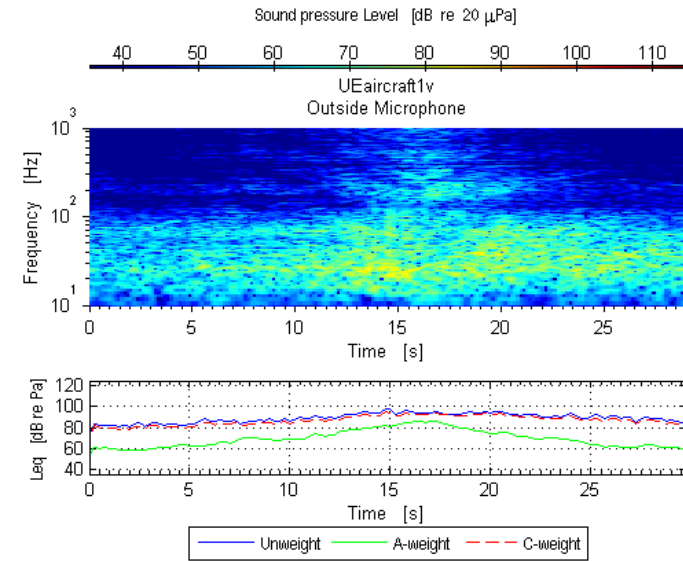


Figure A.83: Outdoor mic measuring aircraft take-off, (70 dBC at window)

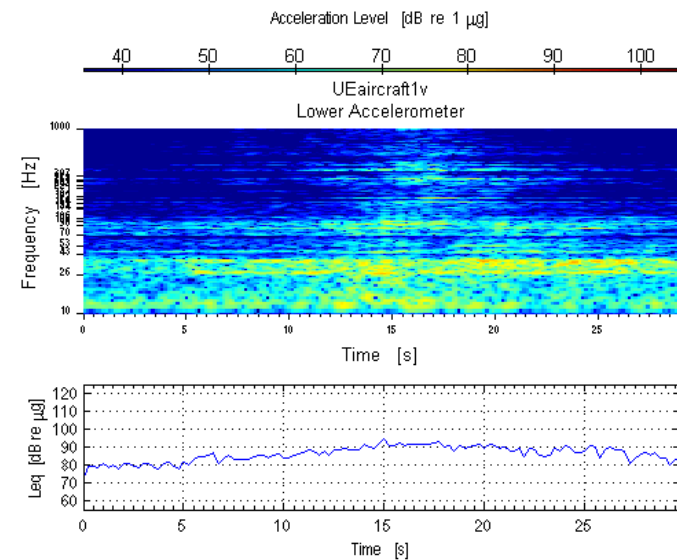


Figure A.84: Accelerometer measuring aircraft take-off, (70 dBC at window)

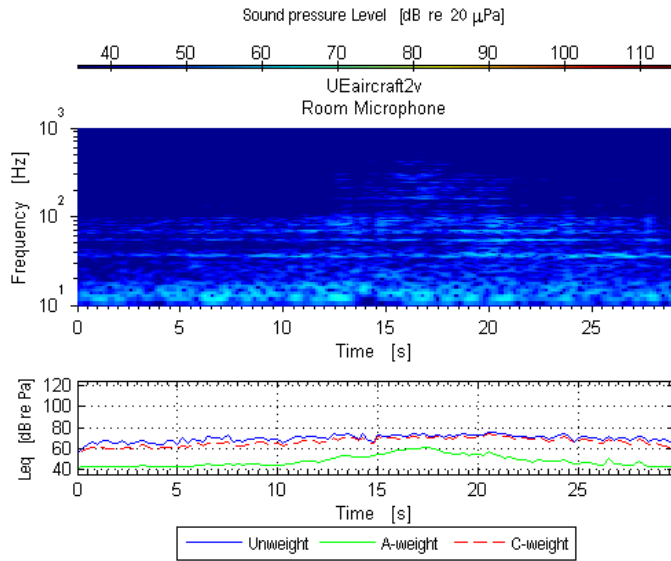


Figure A.85: Room mic measuring aircraft take-off, (80 dBC at window)

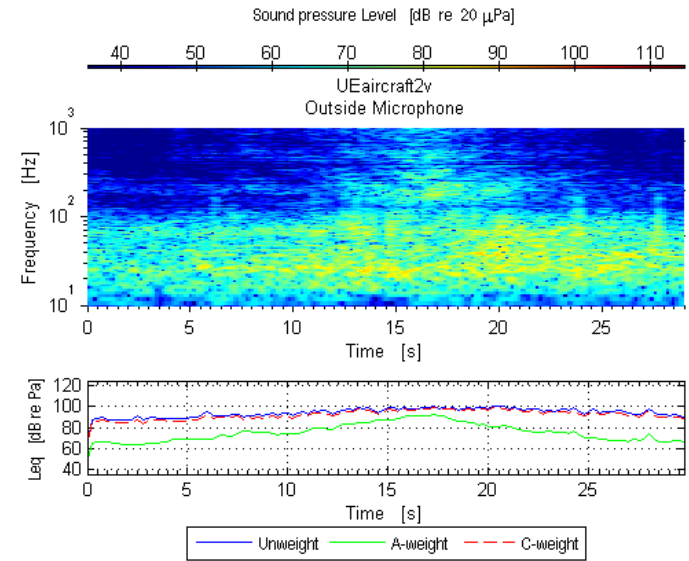


Figure A.86: Outdoor mic measuring aircraft take-off, (80 dBC at window)

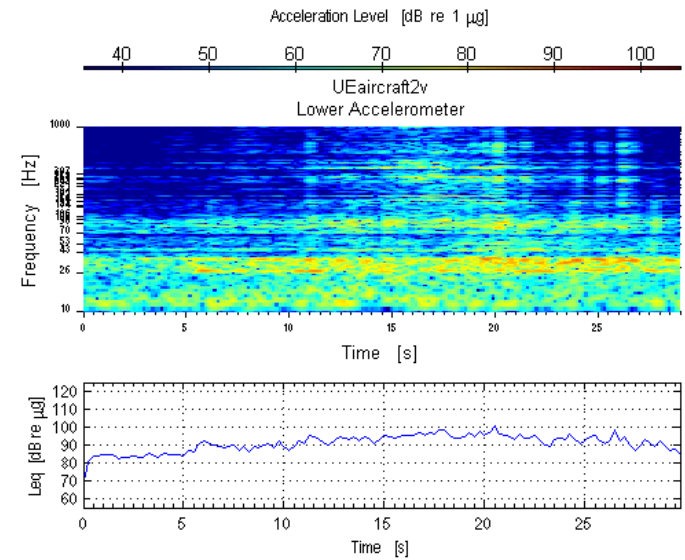


Figure A.87: Accelerometer measuring aircraft take-off, (80 dBC at window)

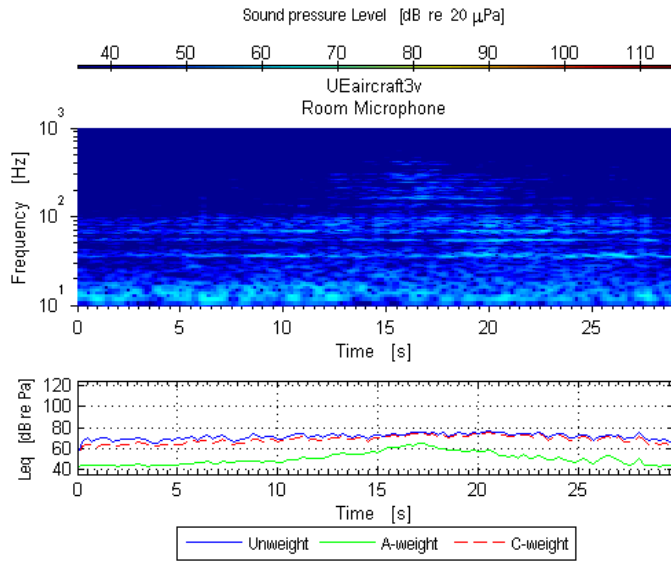


Figure A.88: Room mic measuring aircraft take-off, (90 dBC at window)

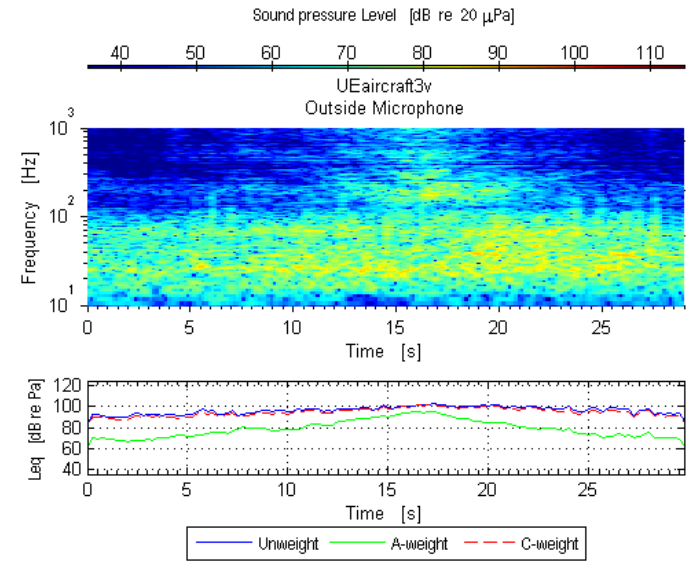


Figure A.89: Outdoor mic measuring aircraft take-off, (90 dBC at window)

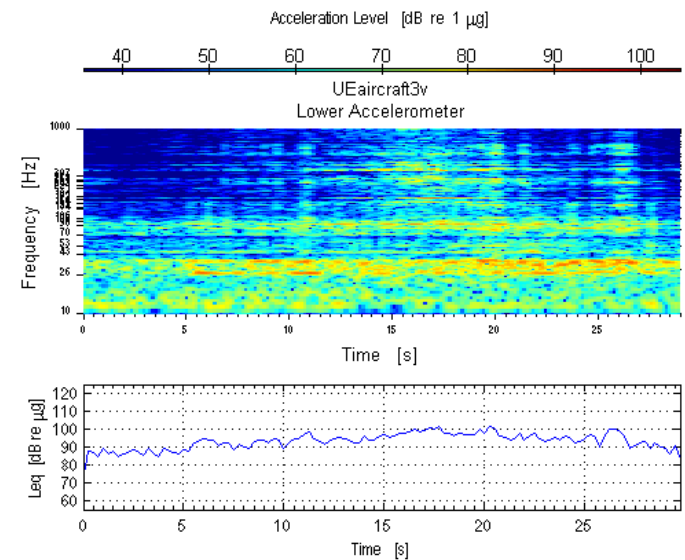


Figure A.90: Accelerometer measuring aircraft take-off, (90 dBC at window)

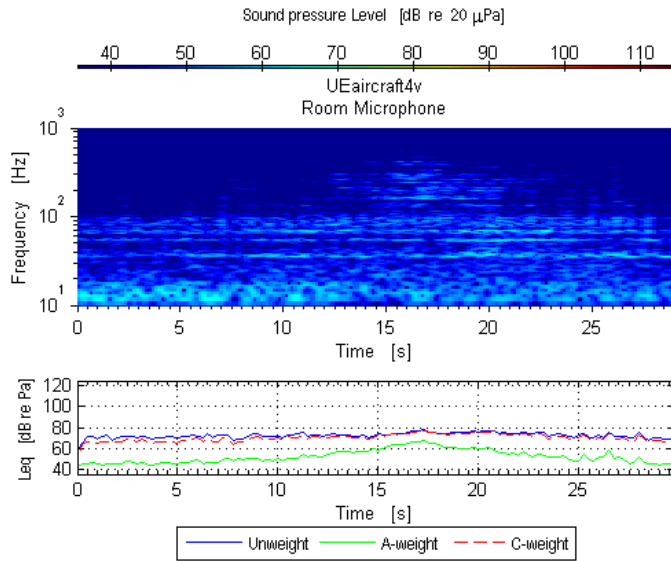


Figure A.91: Room mic measuring aircraft take-off, (100 dBC at window)

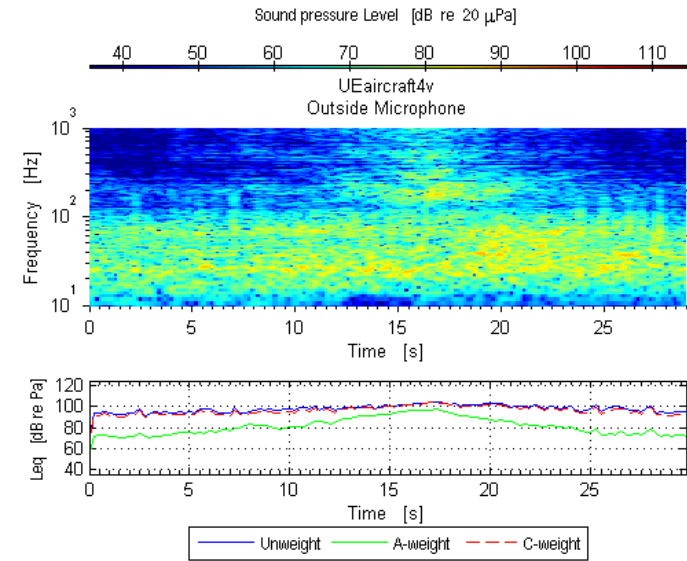


Figure A.92: Outdoor mic measuring aircraft take-off, (100 dBC at window)

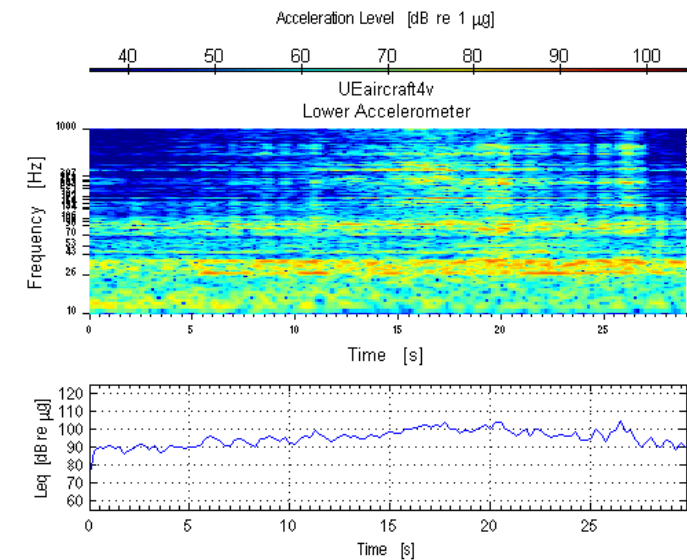


Figure A.93: Accelerometer measuring aircraft take-off, (100 dBC at window)

6.1.c.iii Swept sine, Upper East (UE) window

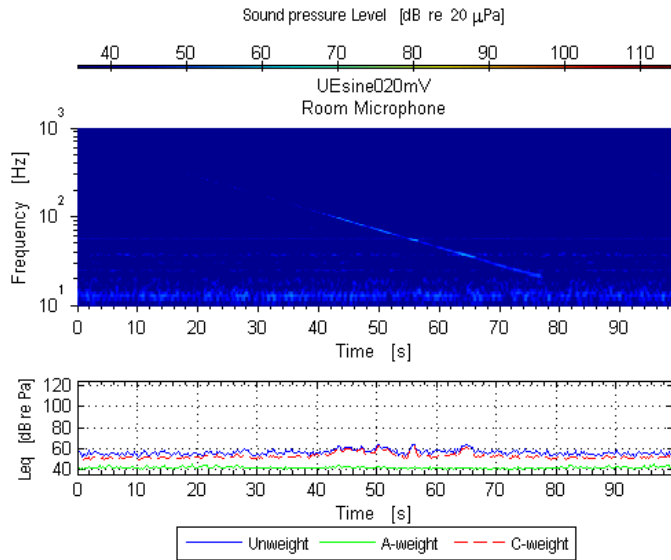


Figure A.94: Room mic measuring swept sine, (70 dBC at window)

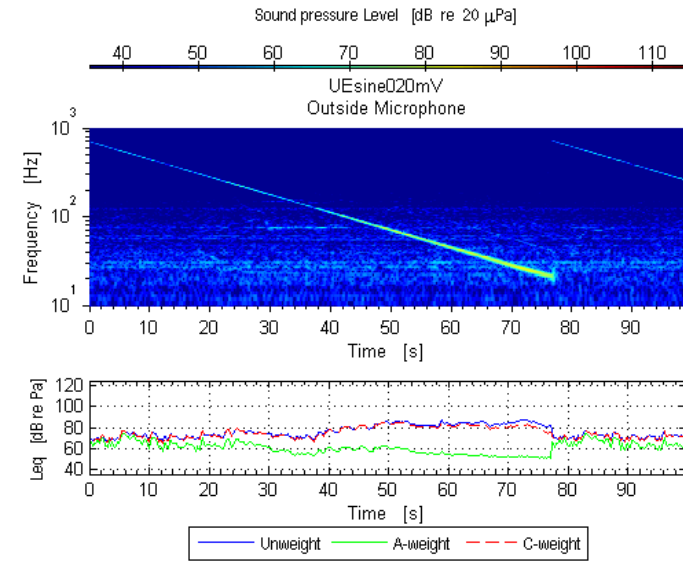


Figure A.95: Outdoor mic measuring swept sine, (70 dBC at window)

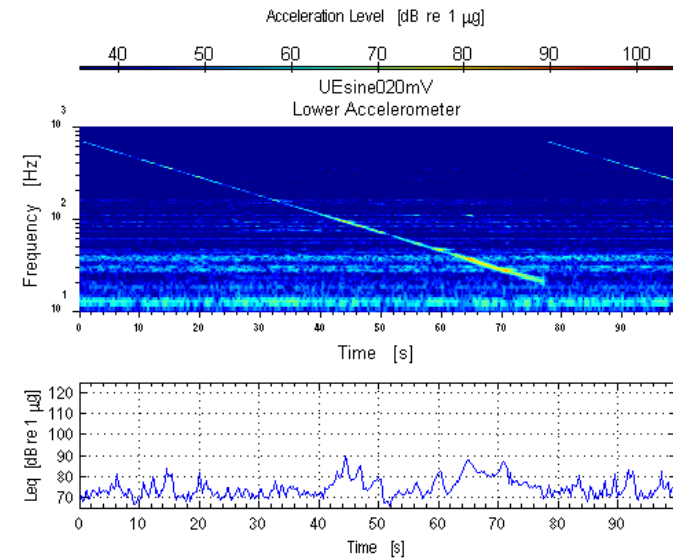


Figure A.96: Accelerometer measuring swept sine, (70 dBC at window)

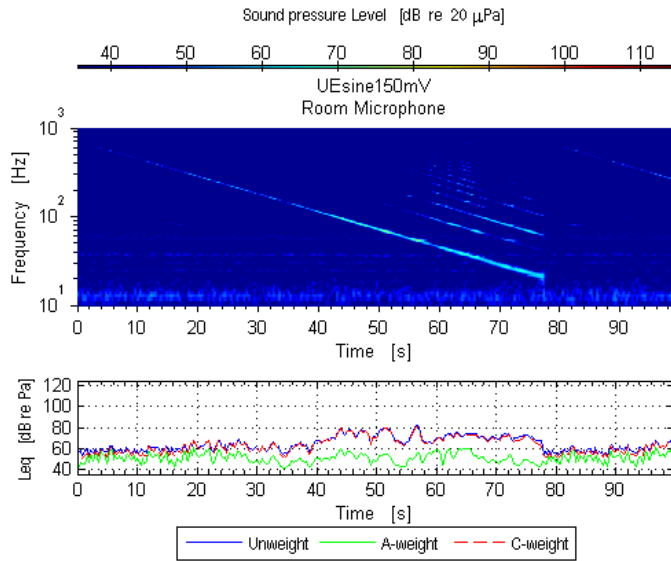


Figure A.97: Room mic measuring swept sine, (80 dBC at window)

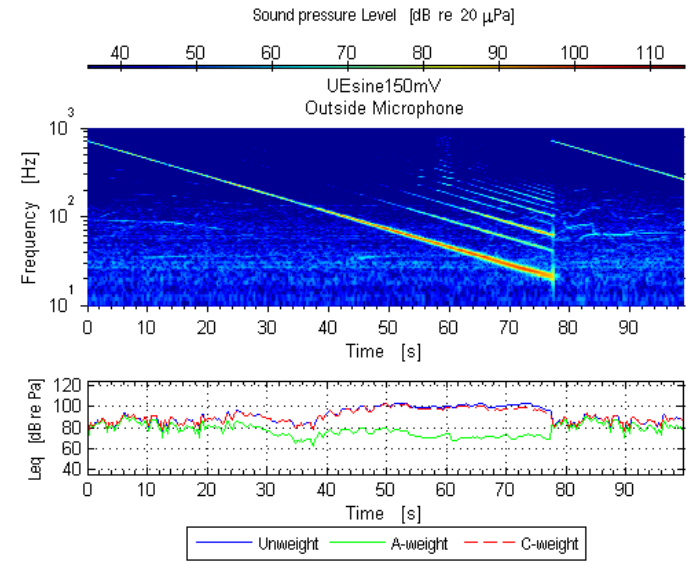


Figure A.98: Outdoor mic measuring swept sine, (80 dBC at window)

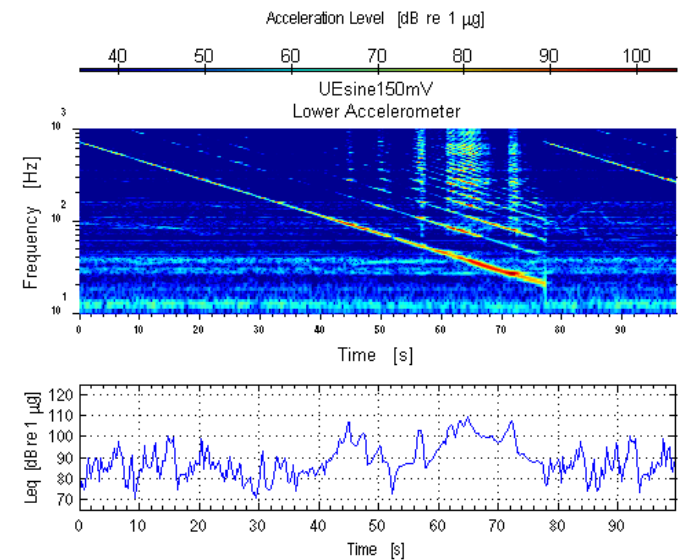


Figure A.99: Accelerometer measuring swept sine, (80 dBC at window)

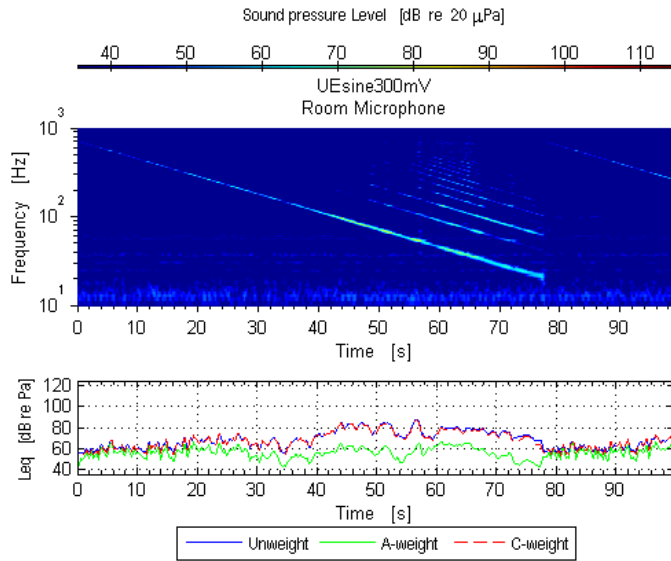


Figure A.100: Room mic measuring swept sine, (90 dBC at window)

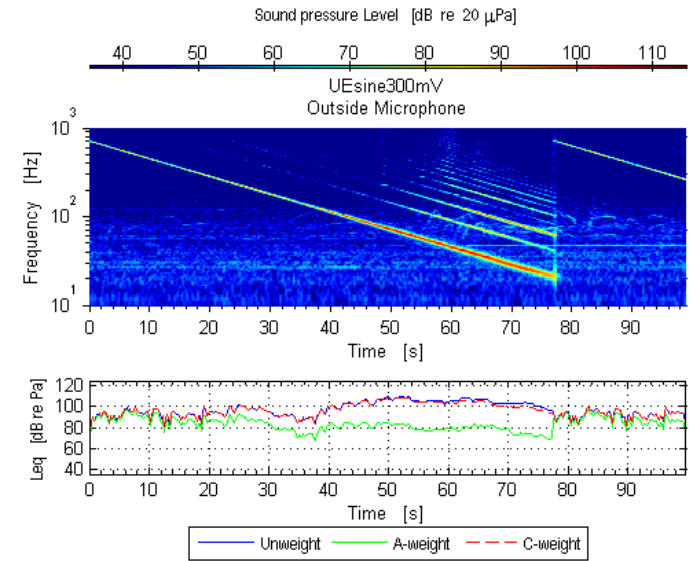


Figure A.101: Outdoor mic measuring swept sine, (90 dBC at window)

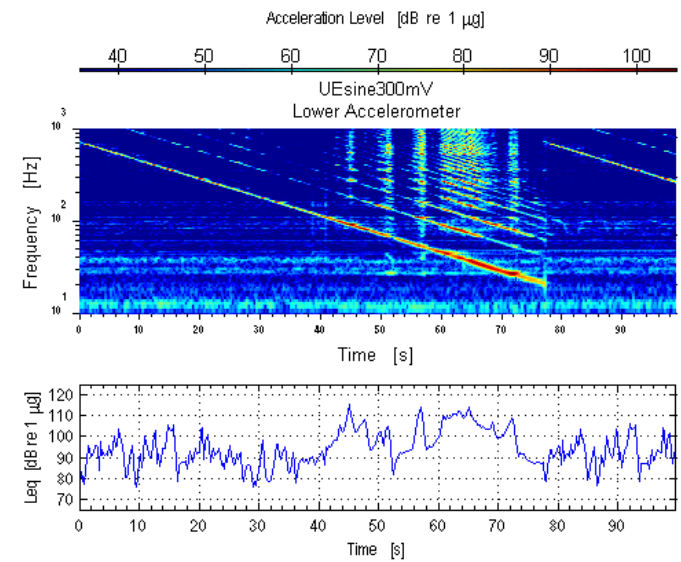


Figure A.102: Accelerometer measuring swept sine, (90 dBC at window)

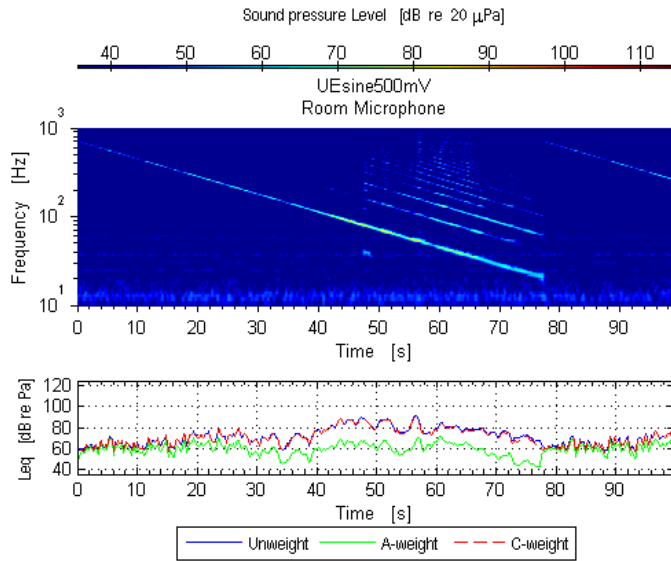


Figure A.103: Room mic measuring swept sine, (100 dBC at window)

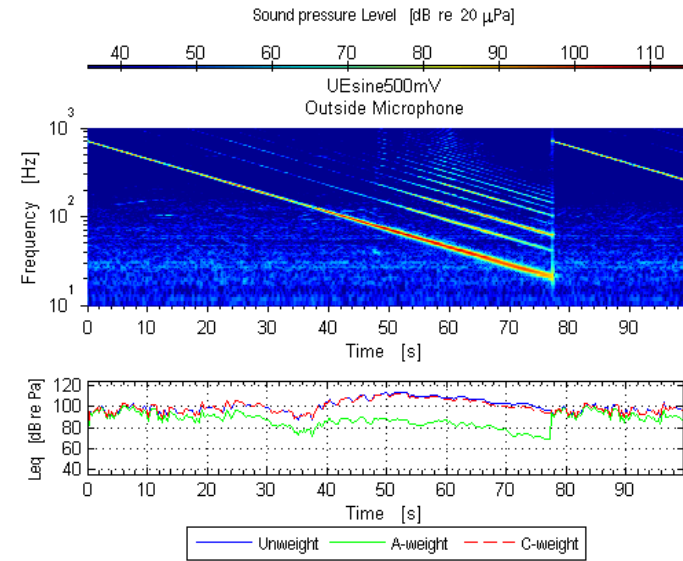


Figure A.104: Outdoor mic measuring swept sine, (100 dBC at window)

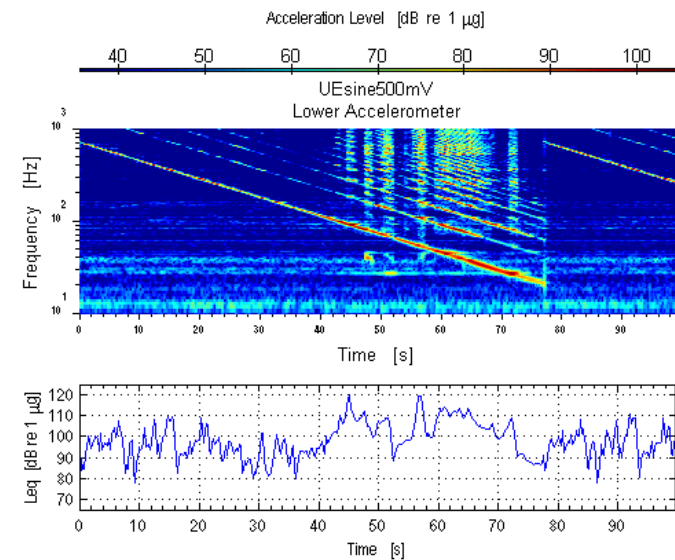


Figure A.105: Accelerometer measuring swept sine, (100 dBC at window)

6.1.c.iv Random noise signal, Upper East (UE) window

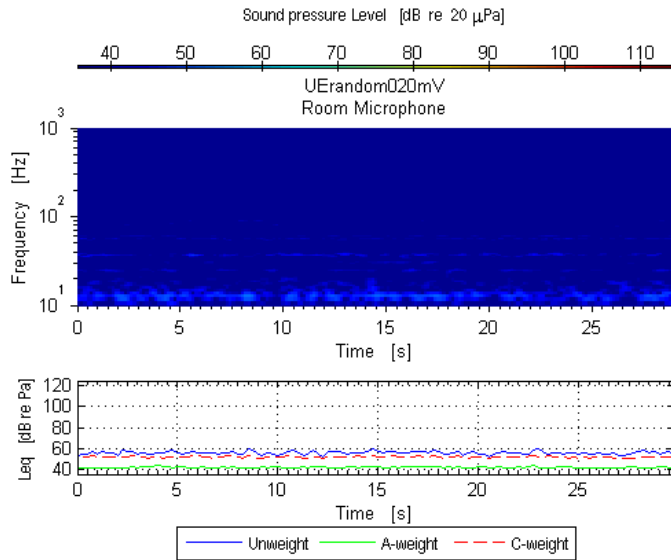


Figure A.106: Room mic measuring random noise, (70 dBC at window)

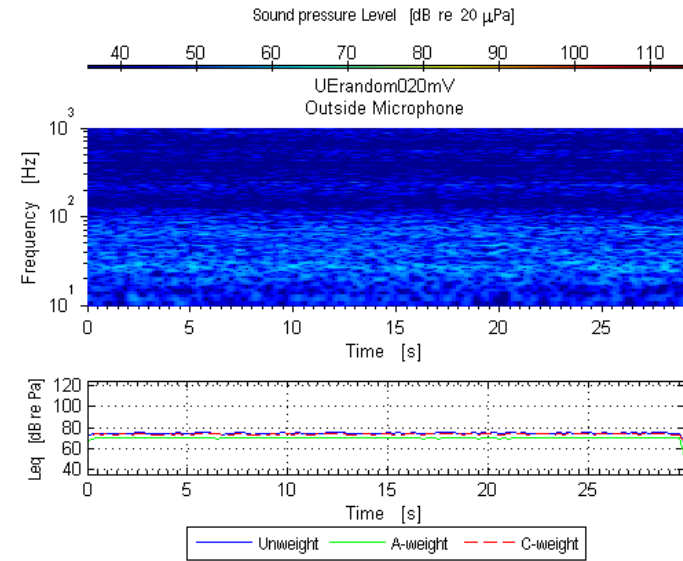


Figure A.107: Outdoor mic measuring random noise, (70 dBC at window)

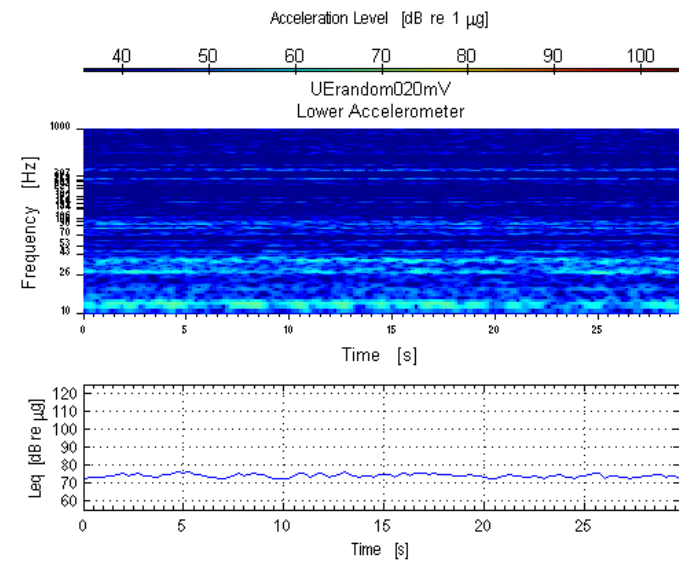


Figure A.108: Accelerometer measuring random noise, (70 dBC at window)

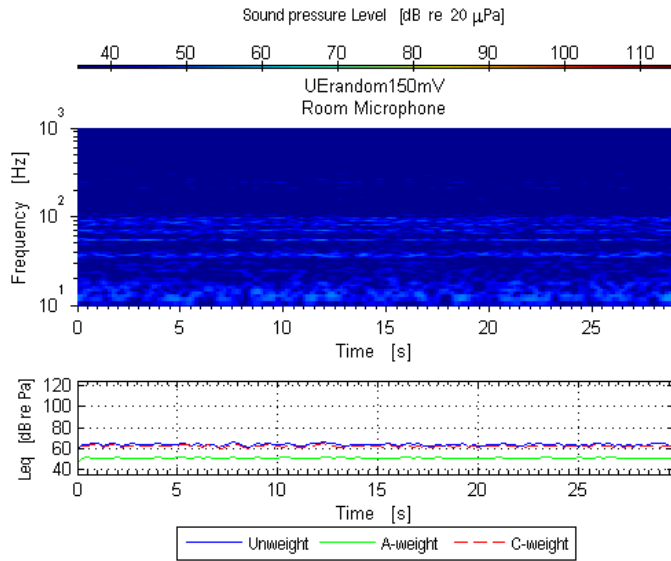


Figure A.109: Room mic measuring random noise, (80 dBC at window)

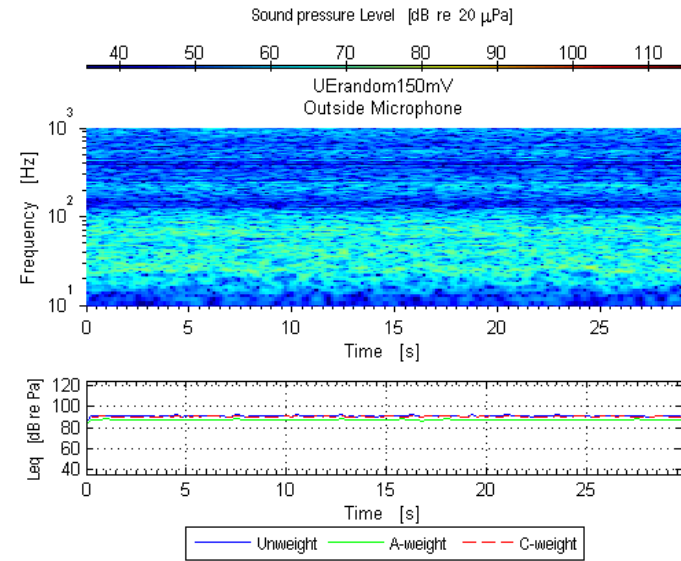


Figure A.110: Outdoor mic measuring random noise, (80 dBC at window)

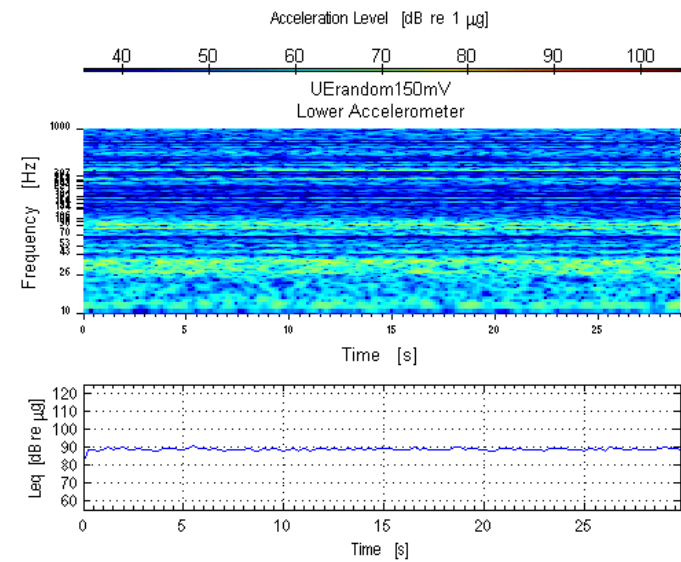


Figure A.111: Accelerometer measuring random noise, (80 dBC at window)

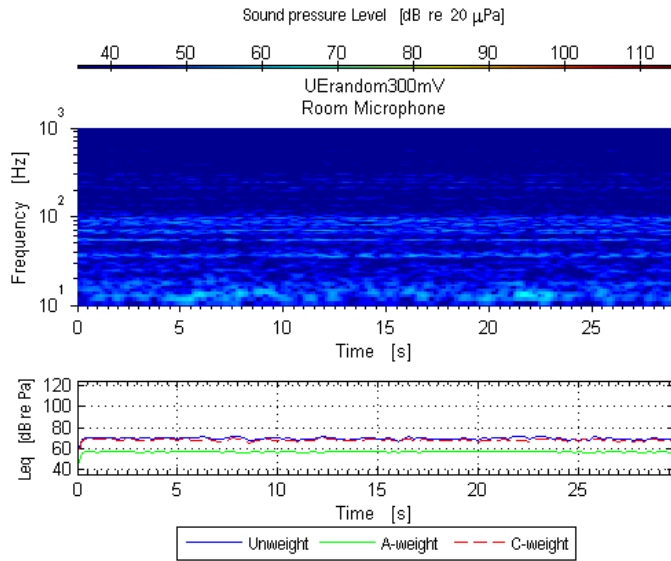


Figure A.112: Room mic measuring random noise, (90 dBC at window)

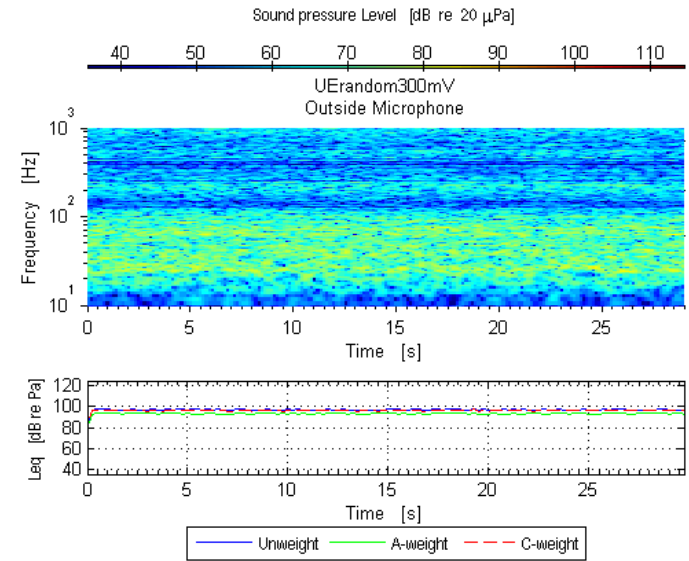


Figure A.113: Outdoor mic measuring random noise, (90 dBC at window)

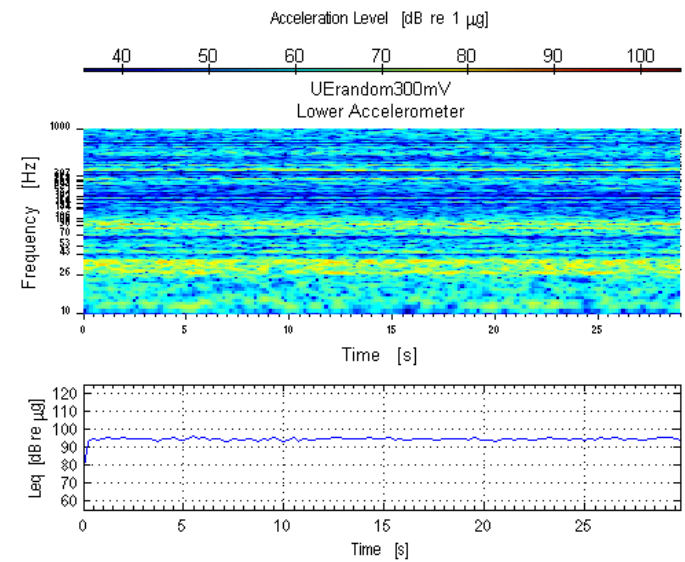


Figure A.114: Accelerometer measuring random noise, (90 dBC at window)

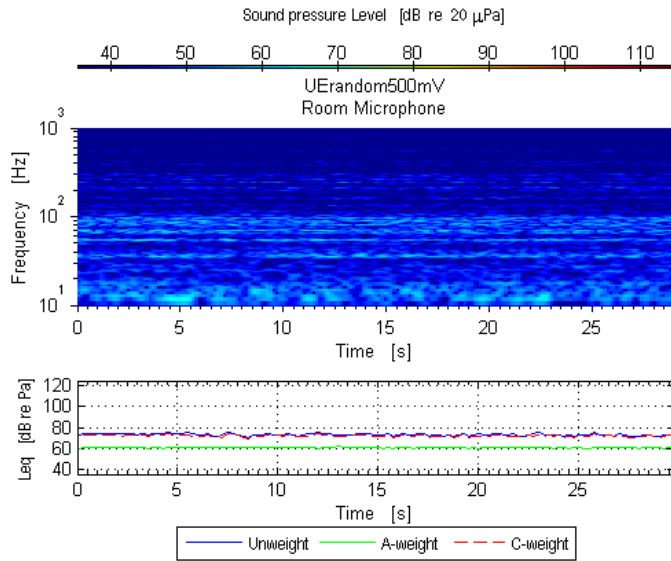


Figure A.115: Room mic measuring random noise, (100 dBC at window)

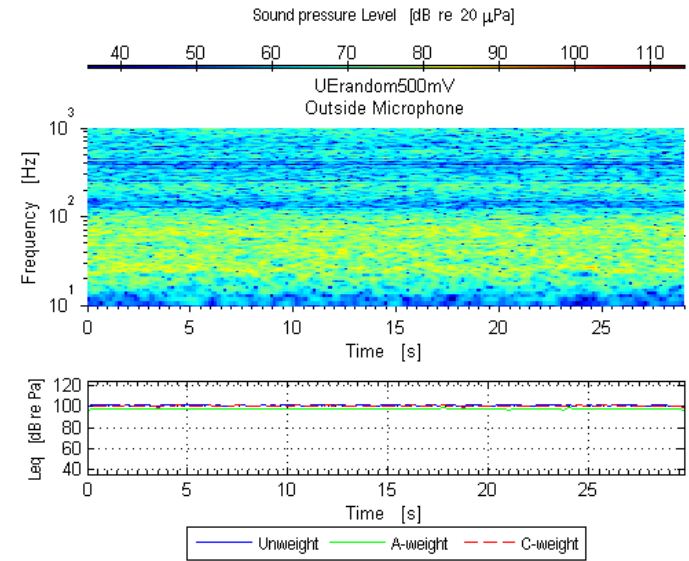


Figure A.116: Outdoor mic measuring random noise, (100 dBC at window)

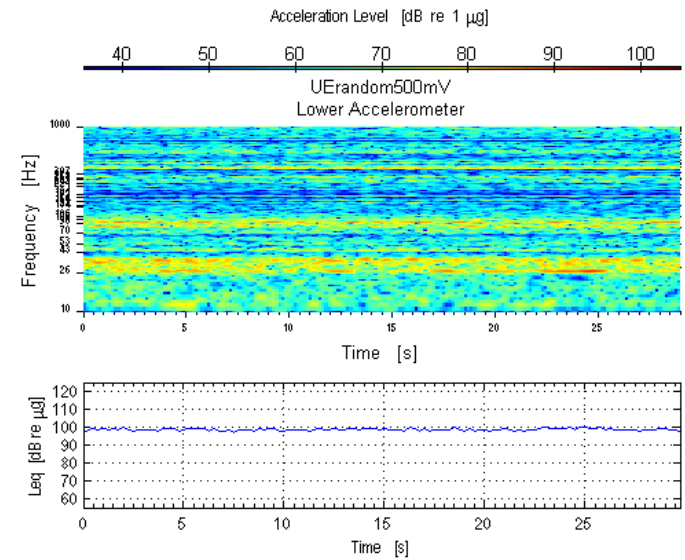


Figure A.117: Accelerometer measuring random noise, (100 dBC at window)

6.1.d Plots of Upper West (UW) window

6.1.d.i Background noise on Upper West (UW) window

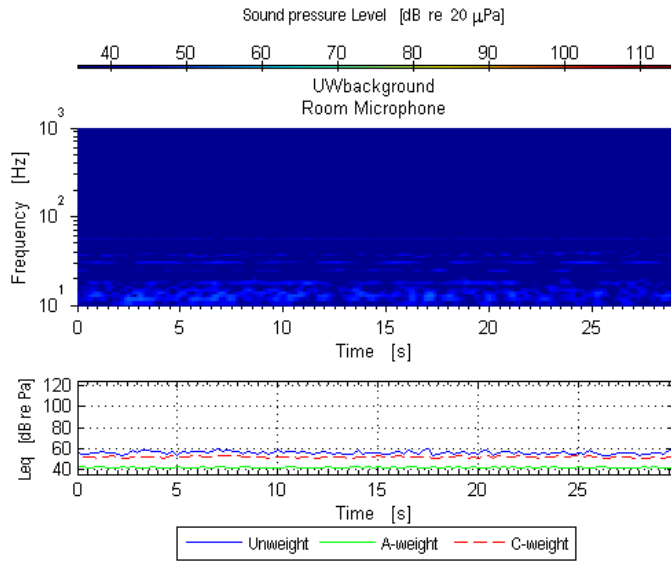


Figure A.118: Room mic measuring background noise

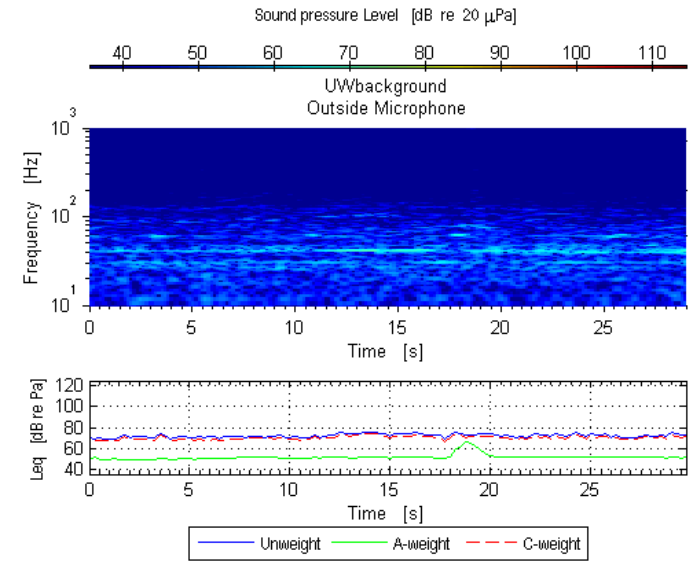


Figure A.119: Outdoor mic measuring background noise

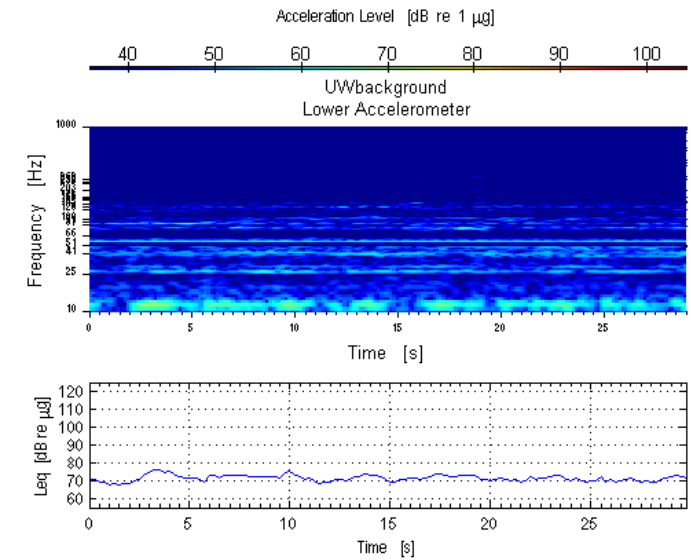


Figure A.120: Accelerometer measuring background noise

6.1.d.ii Aircraft take-off playback, Upper West (UW) window

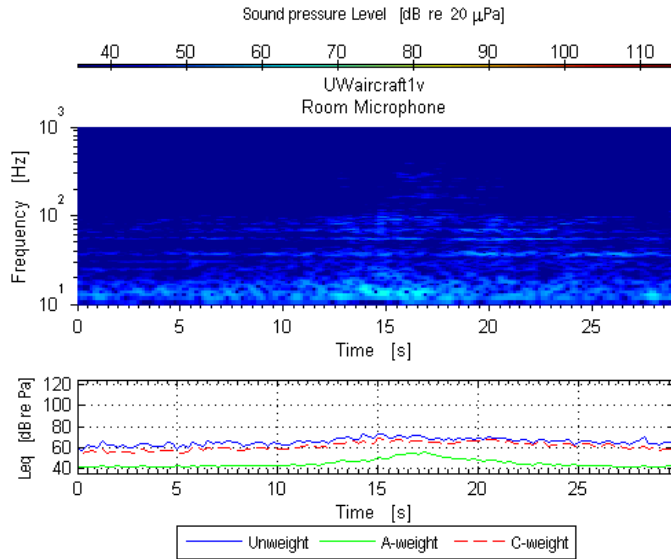


Figure A.121: Room mic measuring aircraft take-off, (70 dBC at window)

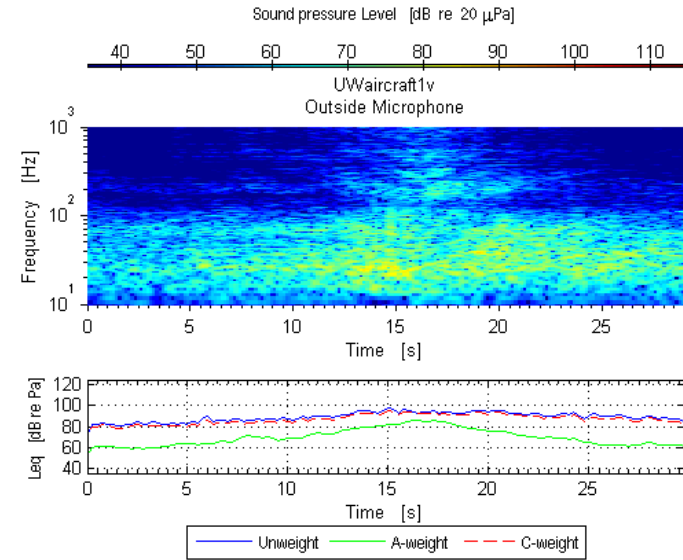


Figure A.122: Outdoor mic measuring aircraft take-off, (70 dBC at window)

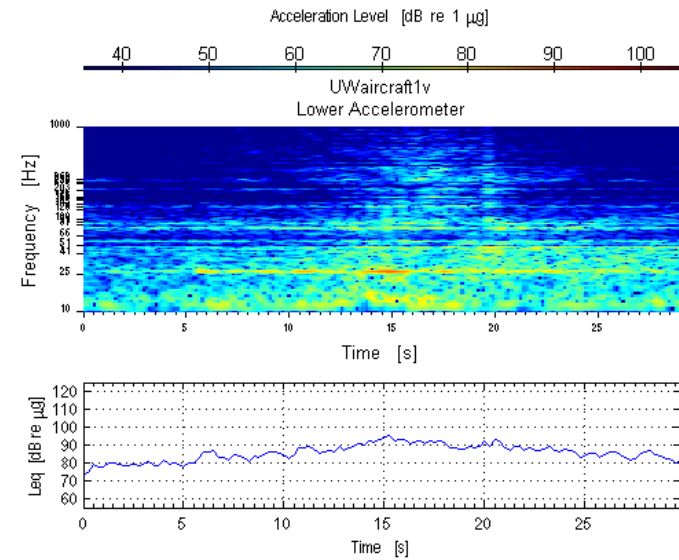


Figure A.123: Accelerometer measuring aircraft take-off, (70 dBC at window)

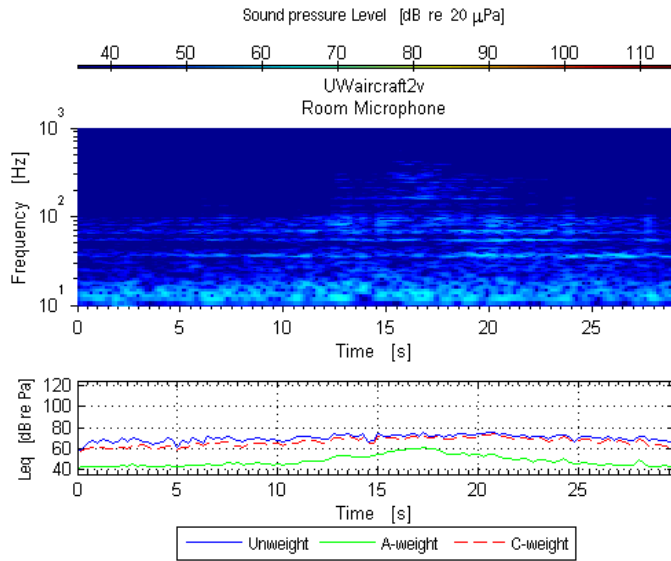


Figure A.124: Room mic measuring aircraft take-off, (80 dBC at window)

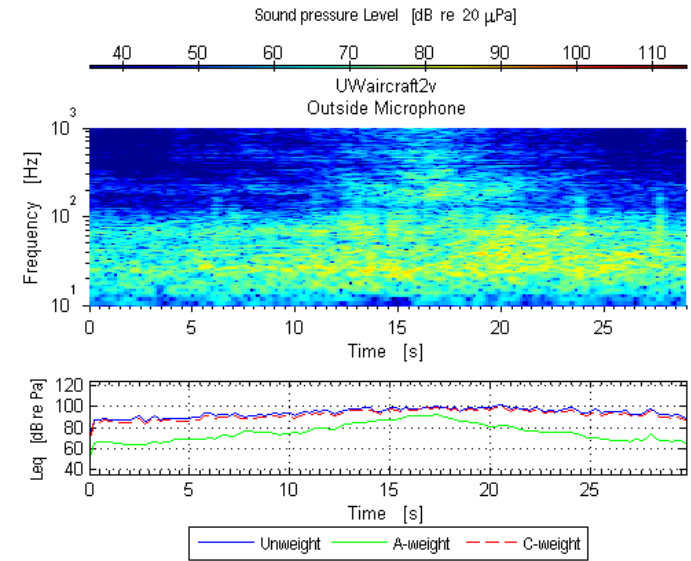


Figure A.125: Outdoor mic measuring aircraft take-off, (80 dBC at window)

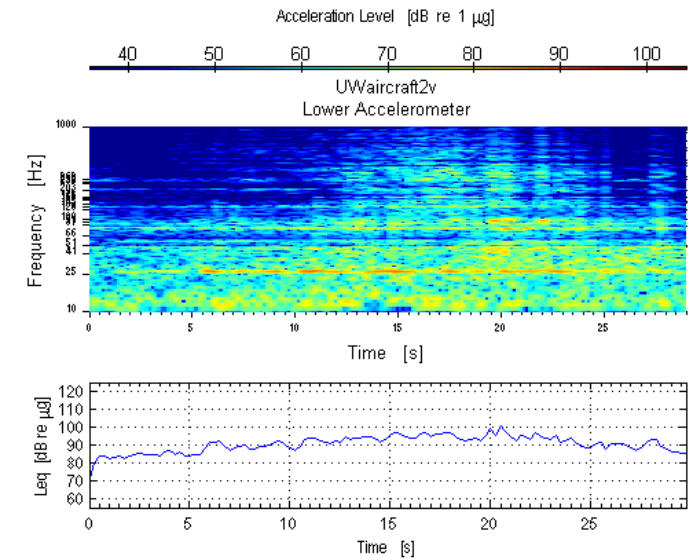


Figure A.126: Accelerometer measuring aircraft take-off, (80 dBC at window)

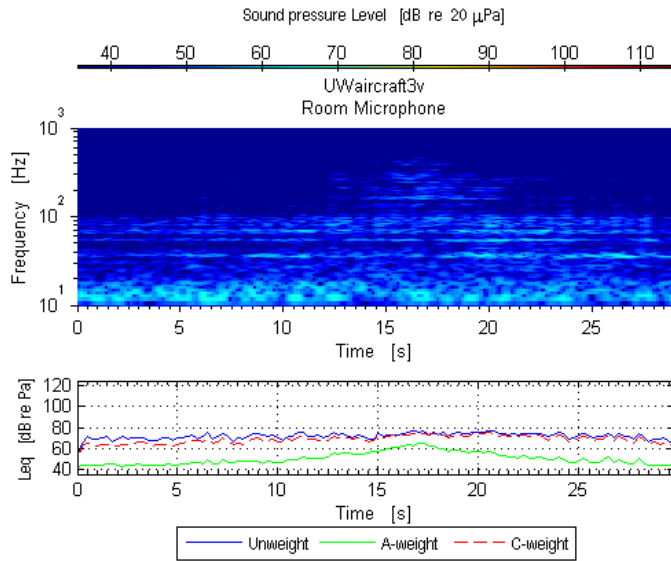


Figure A.127: Room mic measuring aircraft take-off, (90 dBC at window)

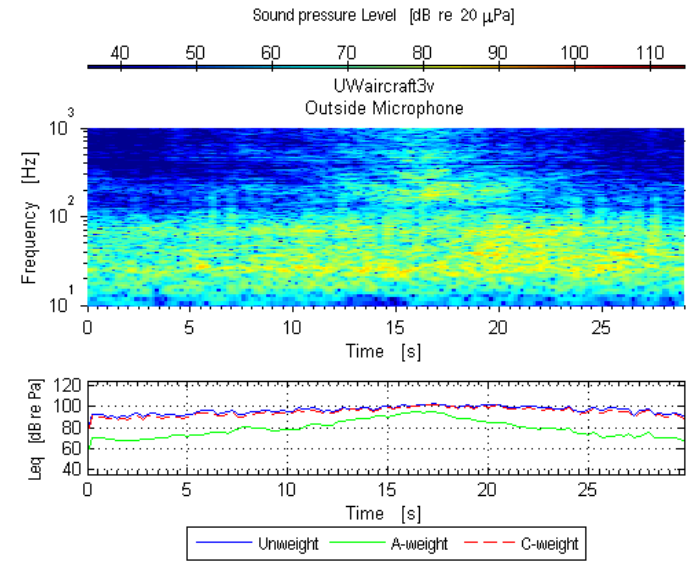


Figure A.128: Outdoor mic measuring aircraft take-off, (90 dBC at window)

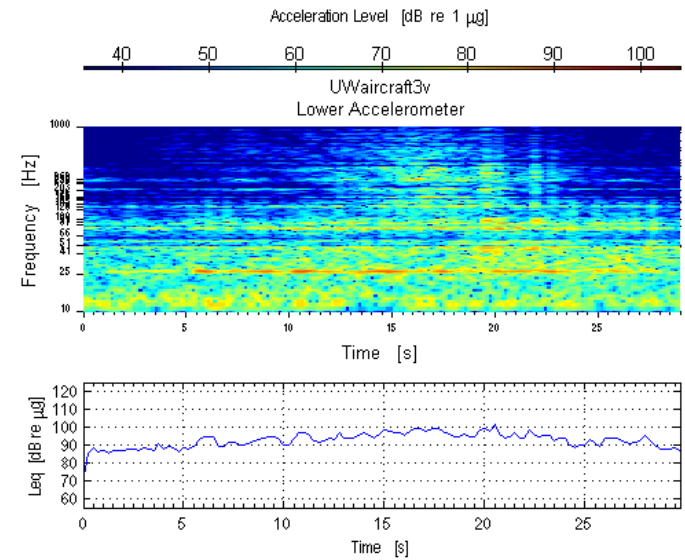


Figure A.129: Accelerometer measuring aircraft take-off, (90 dBC at window)

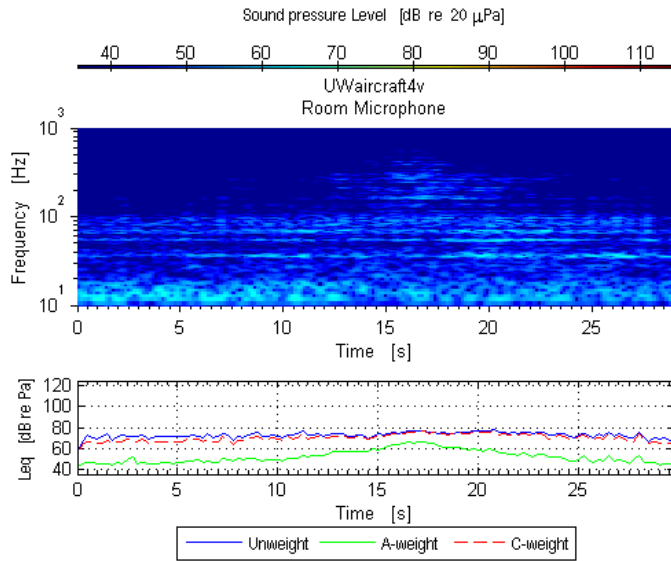


Figure A.130: Room mic measuring aircraft take-off, (100 dBC at window)

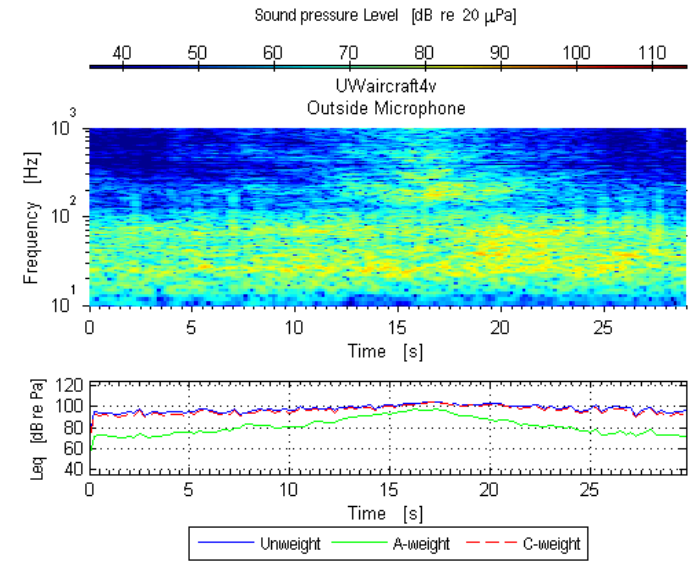


Figure A.131: Outdoor mic measuring aircraft take-off, (100 dBC at window)

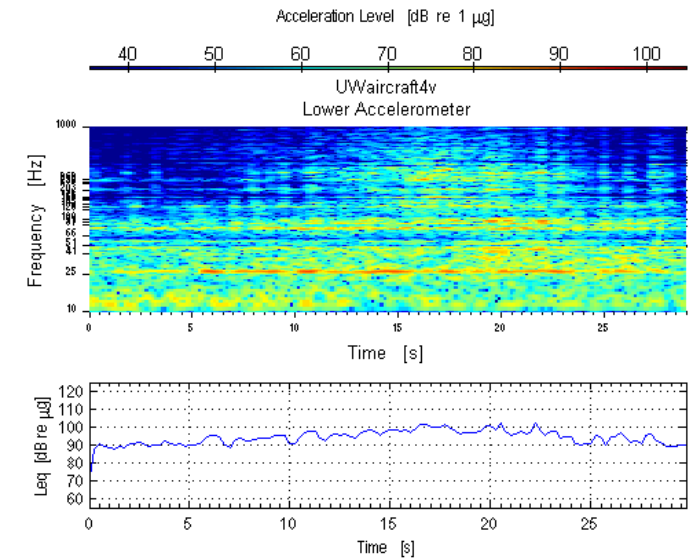


Figure A.132: Accelerometer measuring aircraft take-off, (100 dBC at window)

6.1.d.iii Swept sine, Upper West (UW) window

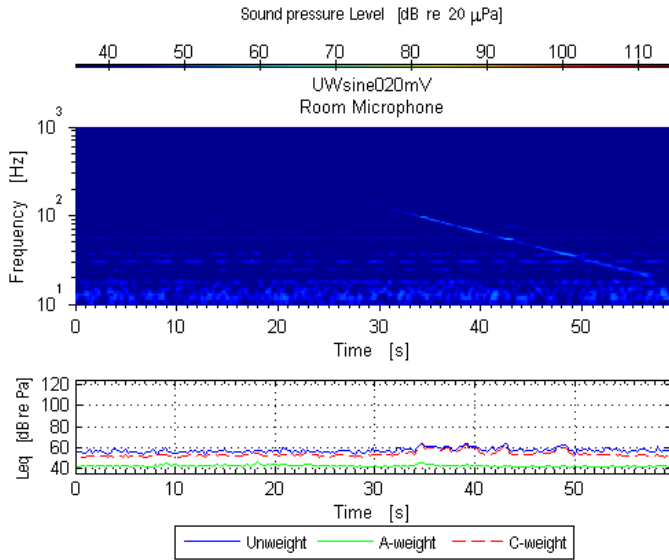


Figure A.133: Room mic measuring swept sine, (70 dBC at window)

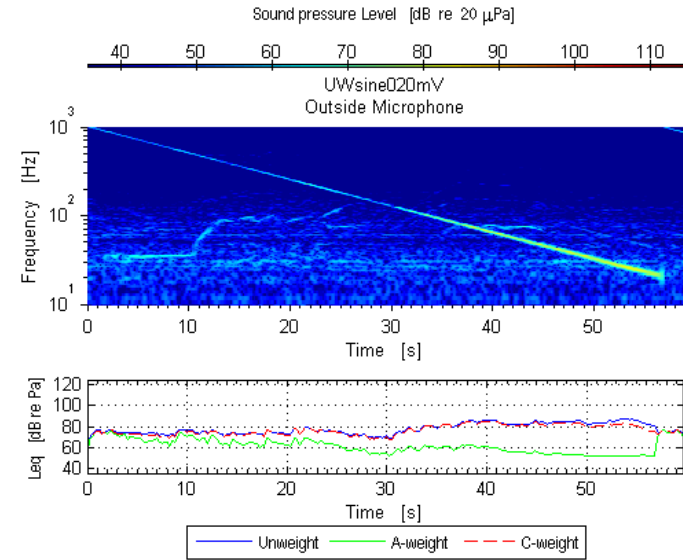


Figure A.134: Outdoor mic measuring swept sine, (70 dBC at window)

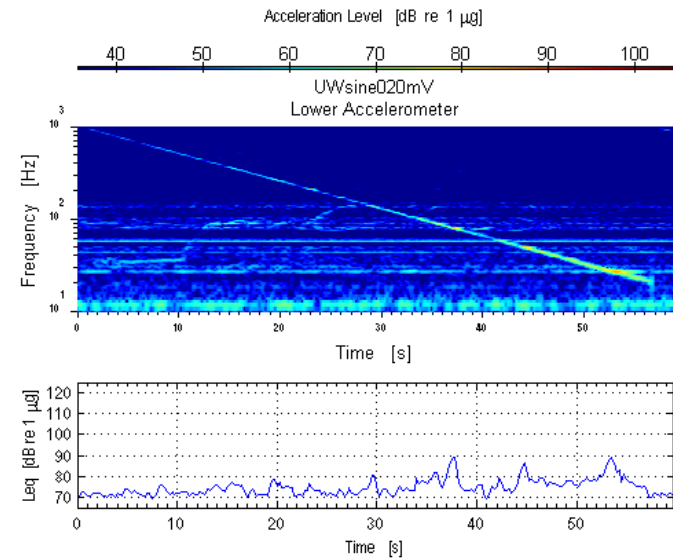


Figure A.135: Accelerometer measuring swept sine, (70 dBC at window)

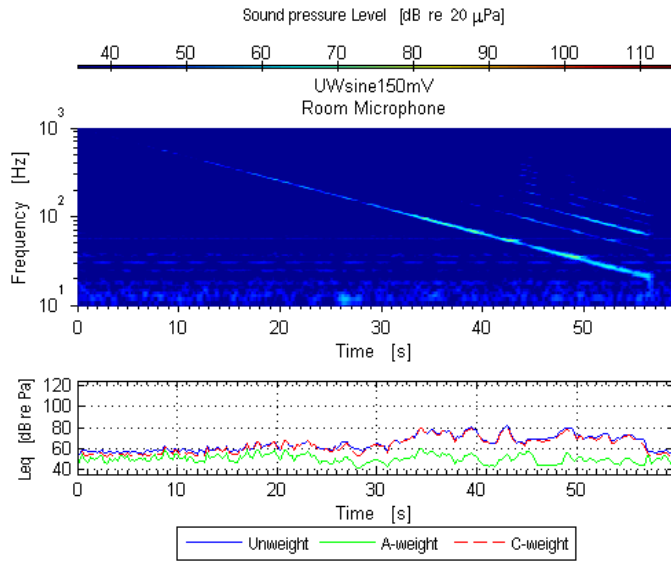


Figure A.136: Room mic measuring swept sine, (80 dBC at window)

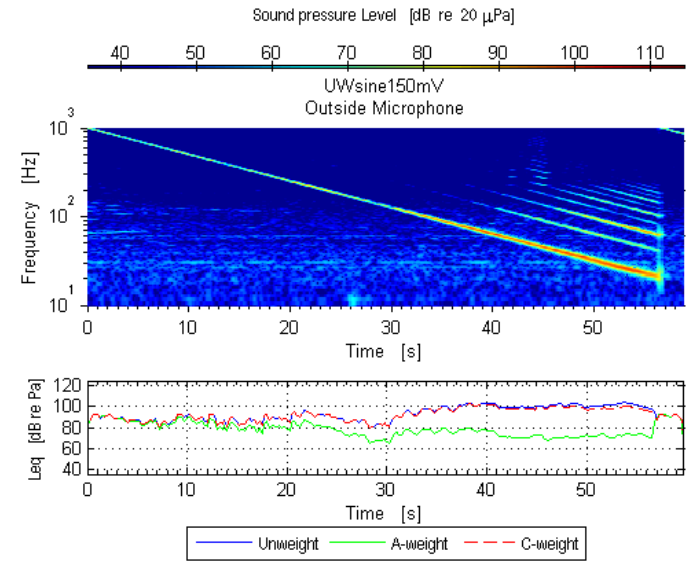


Figure A.137: Outdoor mic measuring swept sine, (80 dBC at window)

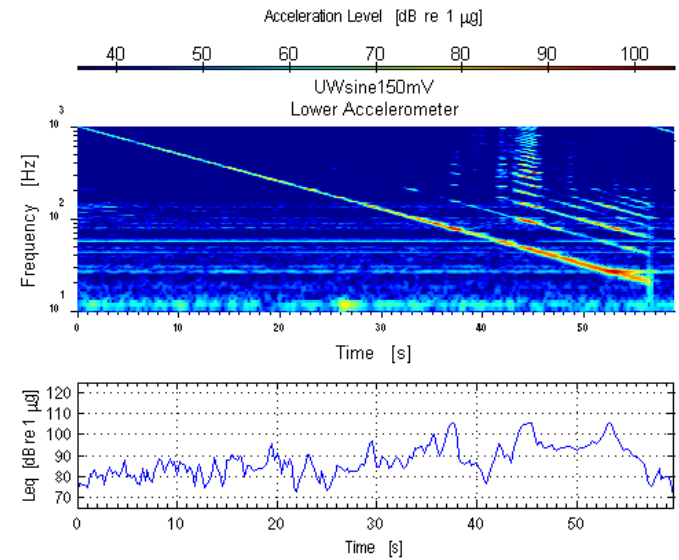


Figure A.138: Accelerometer measuring swept sine, (80 dBC at window)

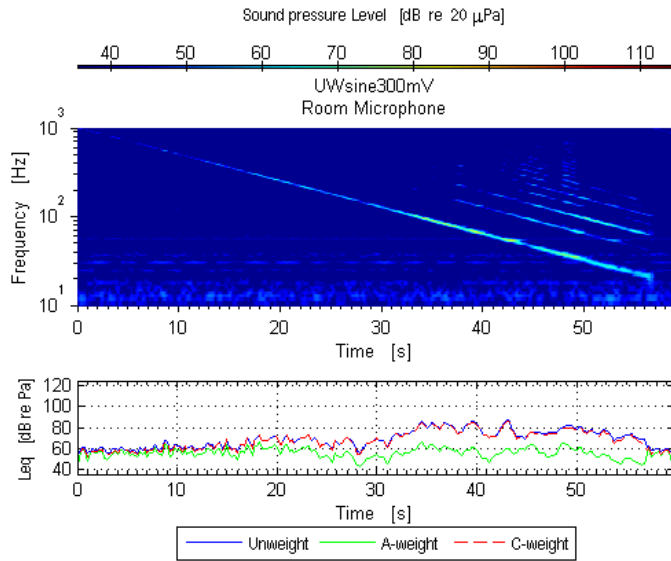


Figure A.139: Room mic measuring swept sine, (90 dBC at window)

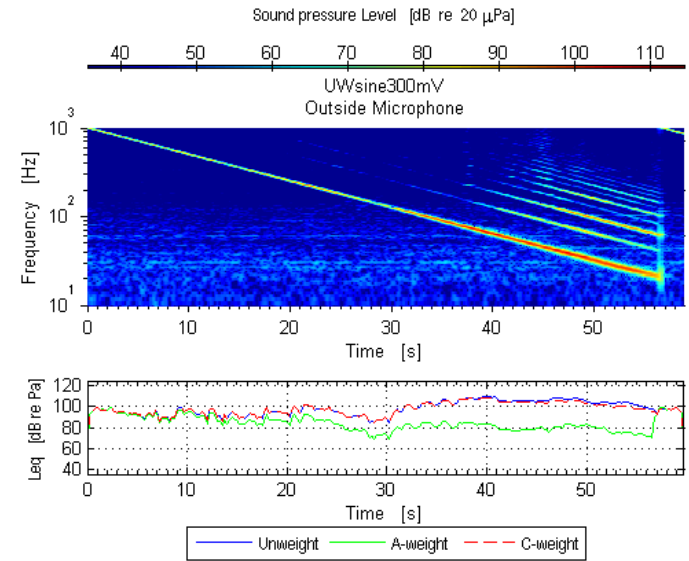


Figure A.140: Outdoor mic measuring swept sine, (90 dBC at window)

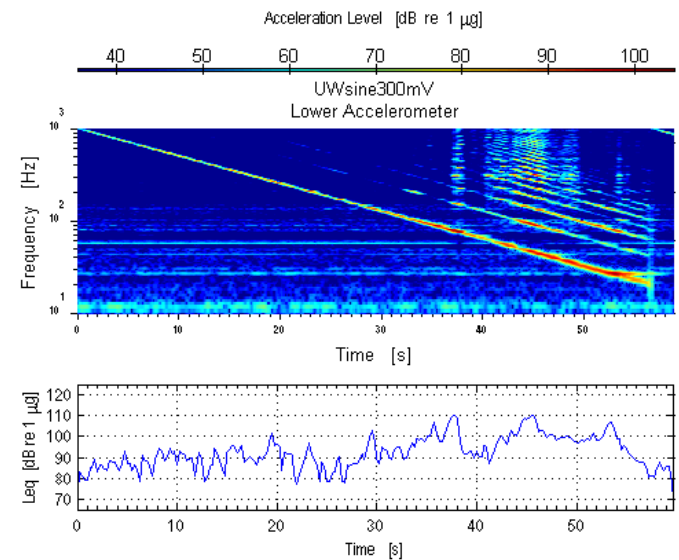


Figure A.141: Accelerometer measuring swept sine, (90 dBC at window)

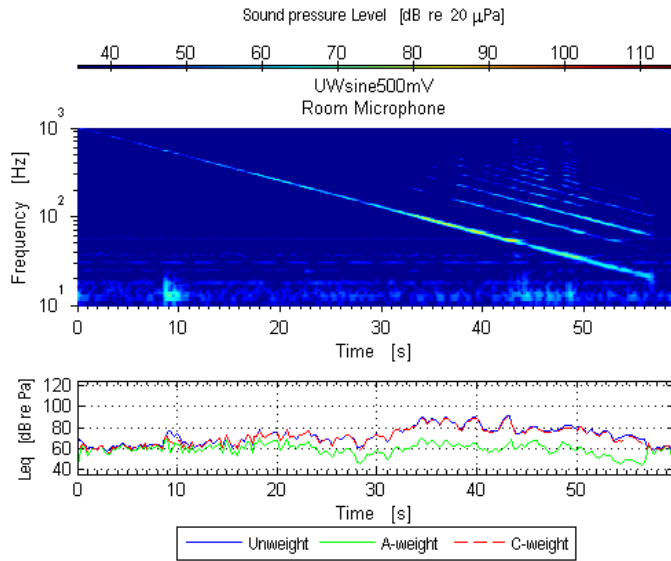


Figure A.142: Room mic measuring swept sine, (100 dBC at window)

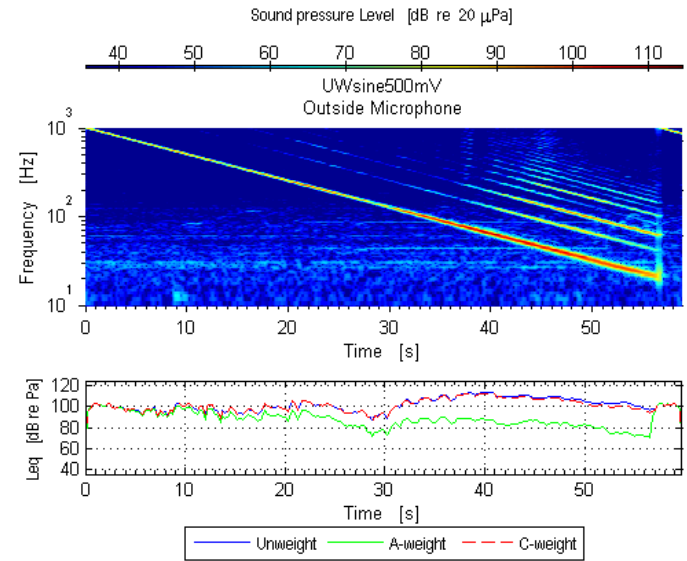


Figure A.143: Outdoor mic measuring swept sine, (100 dBC at window)

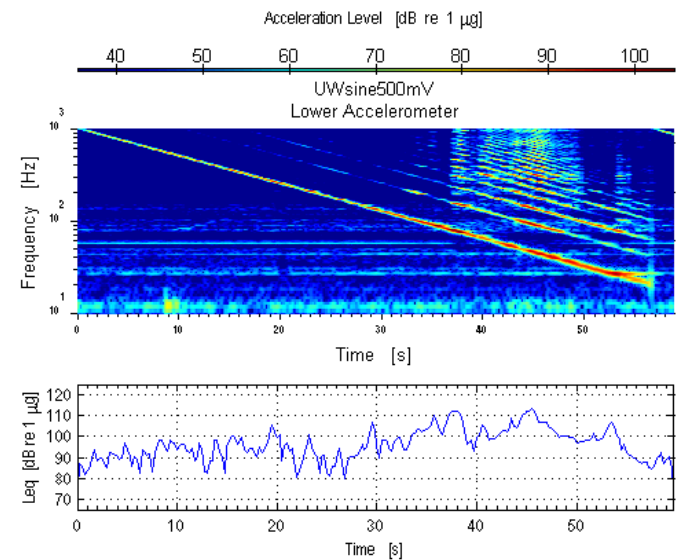


Figure A.144: Accelerometer measuring swept sine, (100 dBC at window)

6.1.d.iv Random noise signal, Upper West (UW) window

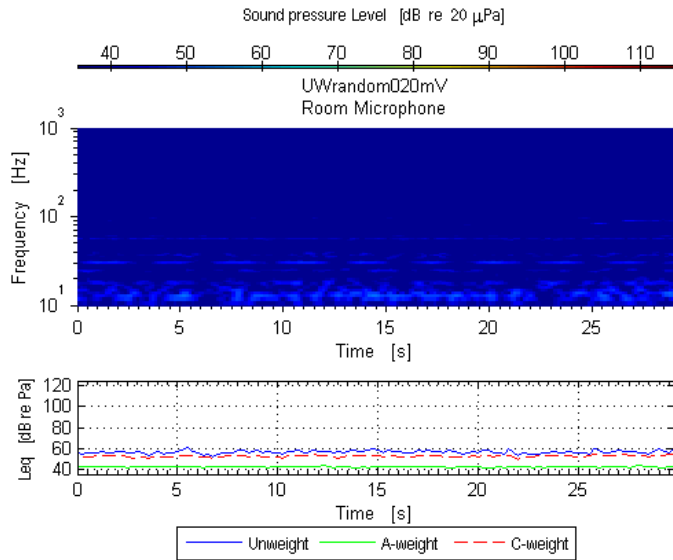


Figure A.145: Room mic measuring random noise, (70 dBC at window)

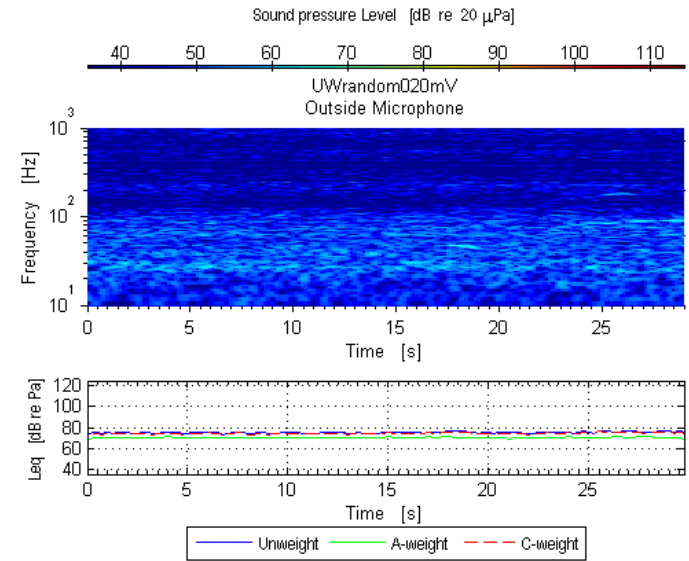


Figure A.146: Outdoor mic measuring random noise, (70 dBC at window)

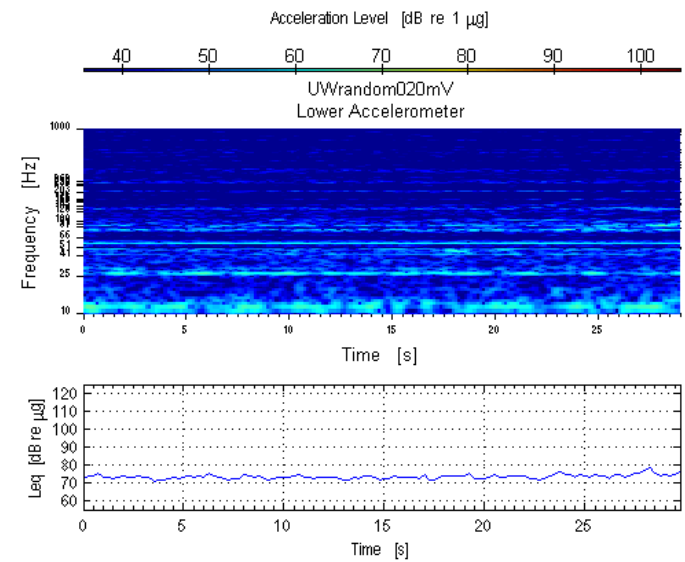


Figure A.147: Accelerometer measuring random noise, (70 dBC at window)

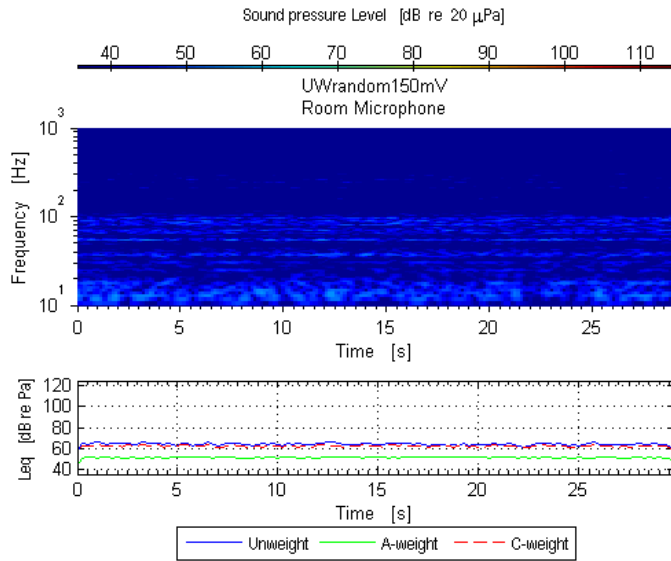


Figure A.148: Room mic measuring random noise, (80 dBC at window)

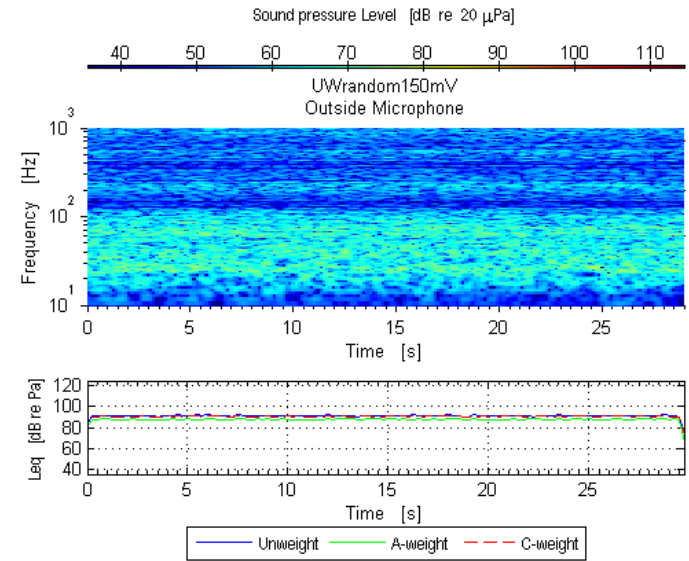


Figure A.149: Outdoor mic measuring random noise, (80 dBC at window)

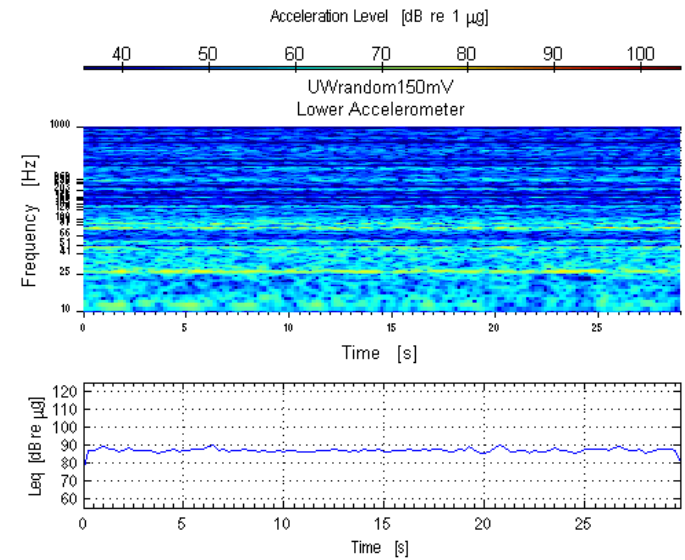


Figure A.150: Accelerometer measuring random noise, (80 dBC at window)

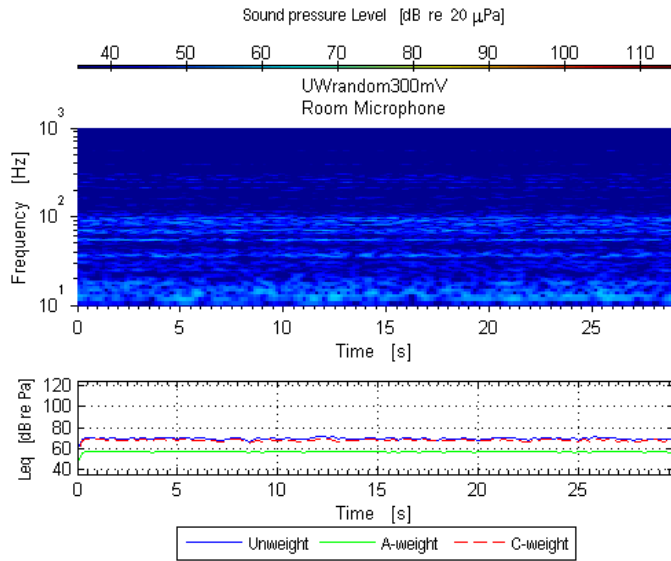


Figure A.151: Room mic measuring random noise, (90 dBC at window)

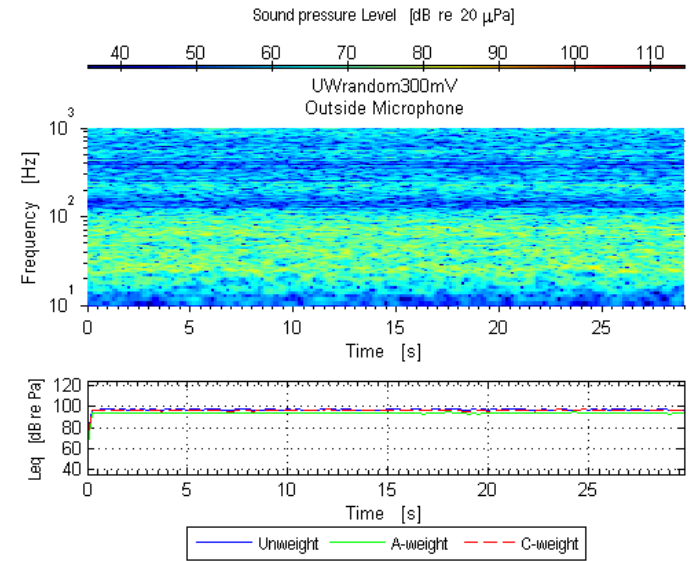


Figure 152: Outdoor mic measuring random noise, (90 dBC at window)

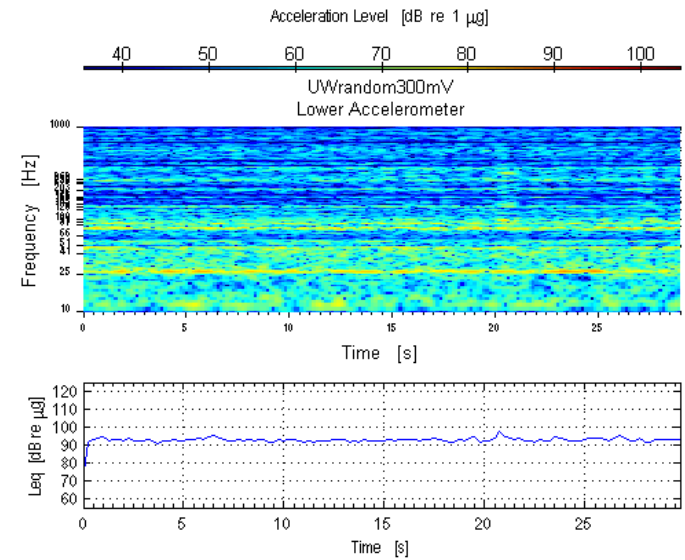


Figure A.153: Accelerometer measuring random noise, (90 dBC at window)

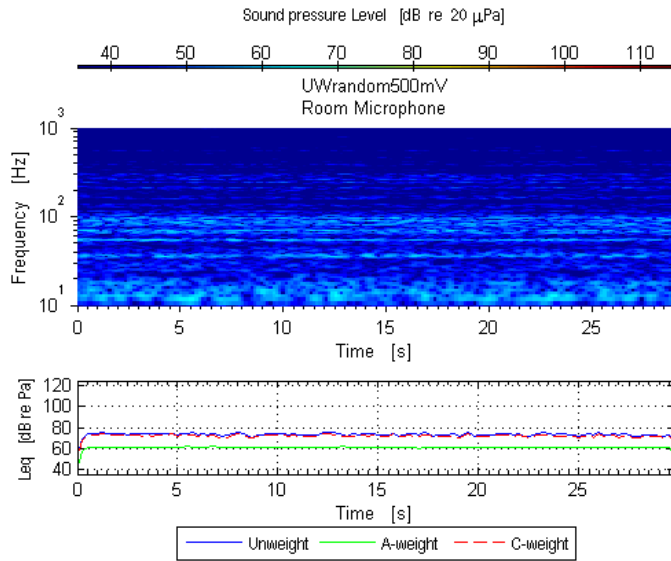


Figure A.154: Room mic measuring random noise, (100 dBC at window)

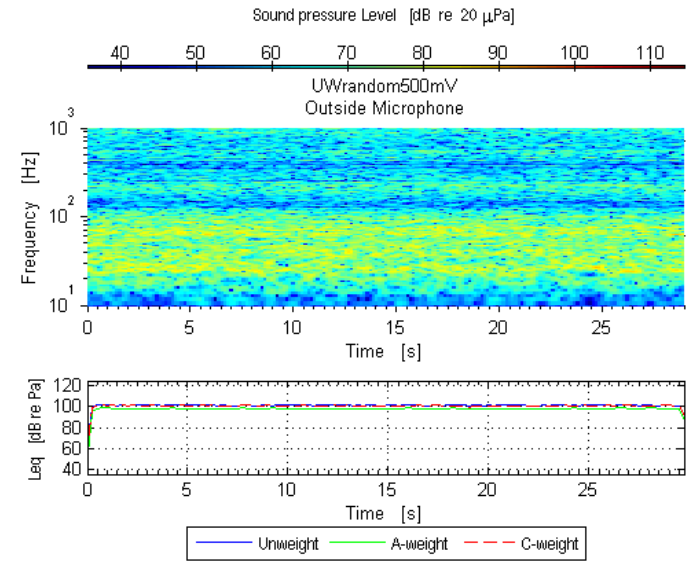


Figure A.155: Outdoor mic measuring random noise, (100 dBC at window)

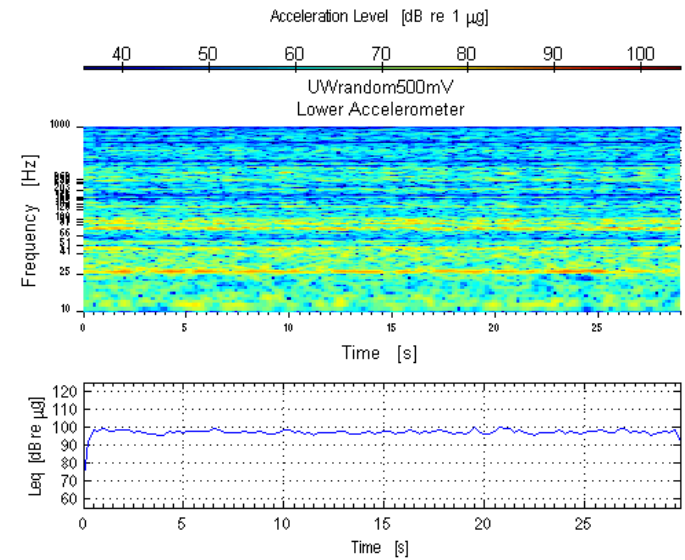


Figure A.156: Accelerometer measuring random noise, (100 dBC at window)

6.2 Appendix B: Measured Window Rattle Thresholds

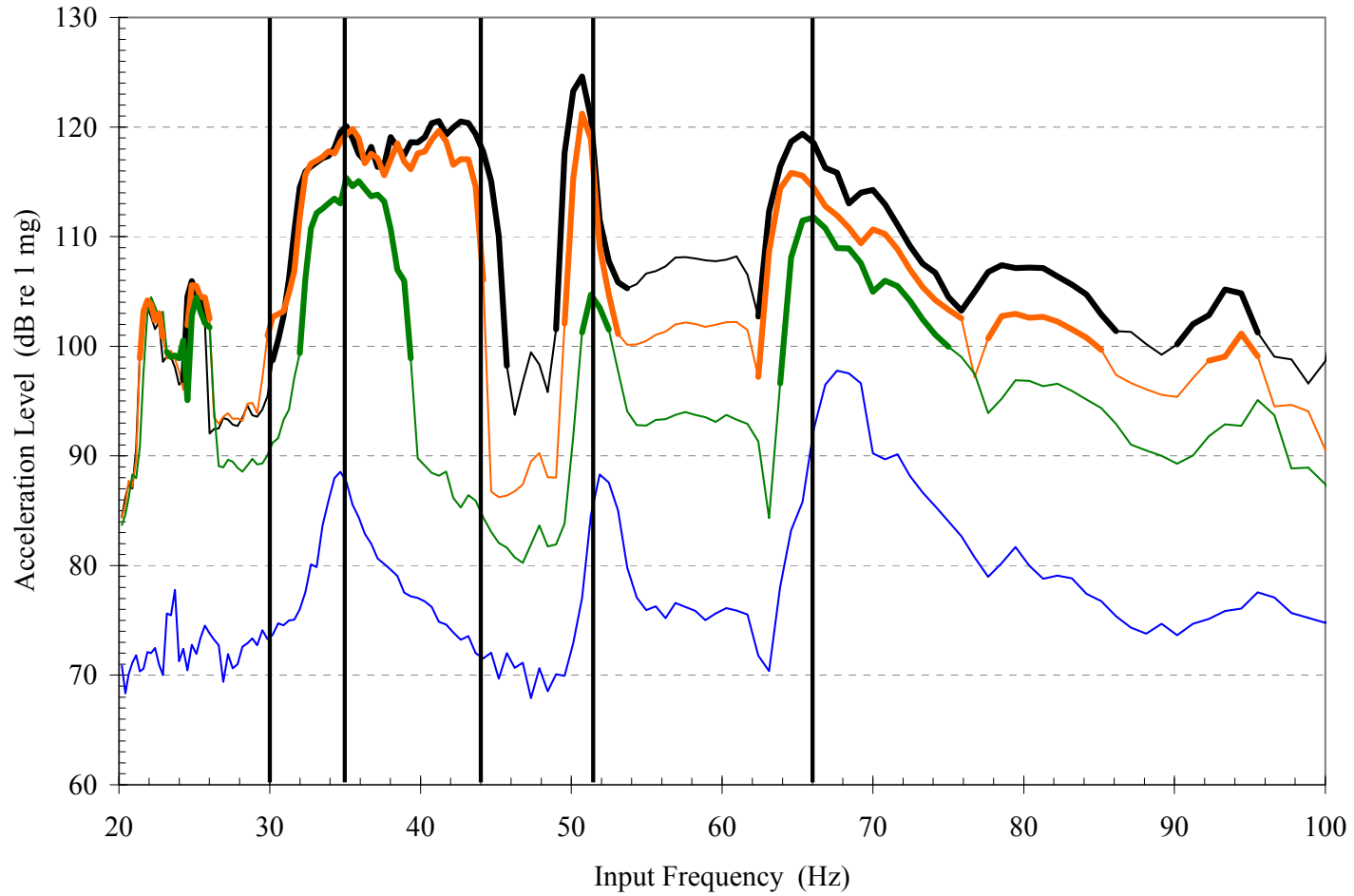


Figure B.1: Response of the lower east window to four swept sine signal strengths; 70 dBC blue, 80 dBC green, 90 dBC orange, 100 dBC black. Bolded line-style indicates input frequencies at which rattle occurred.

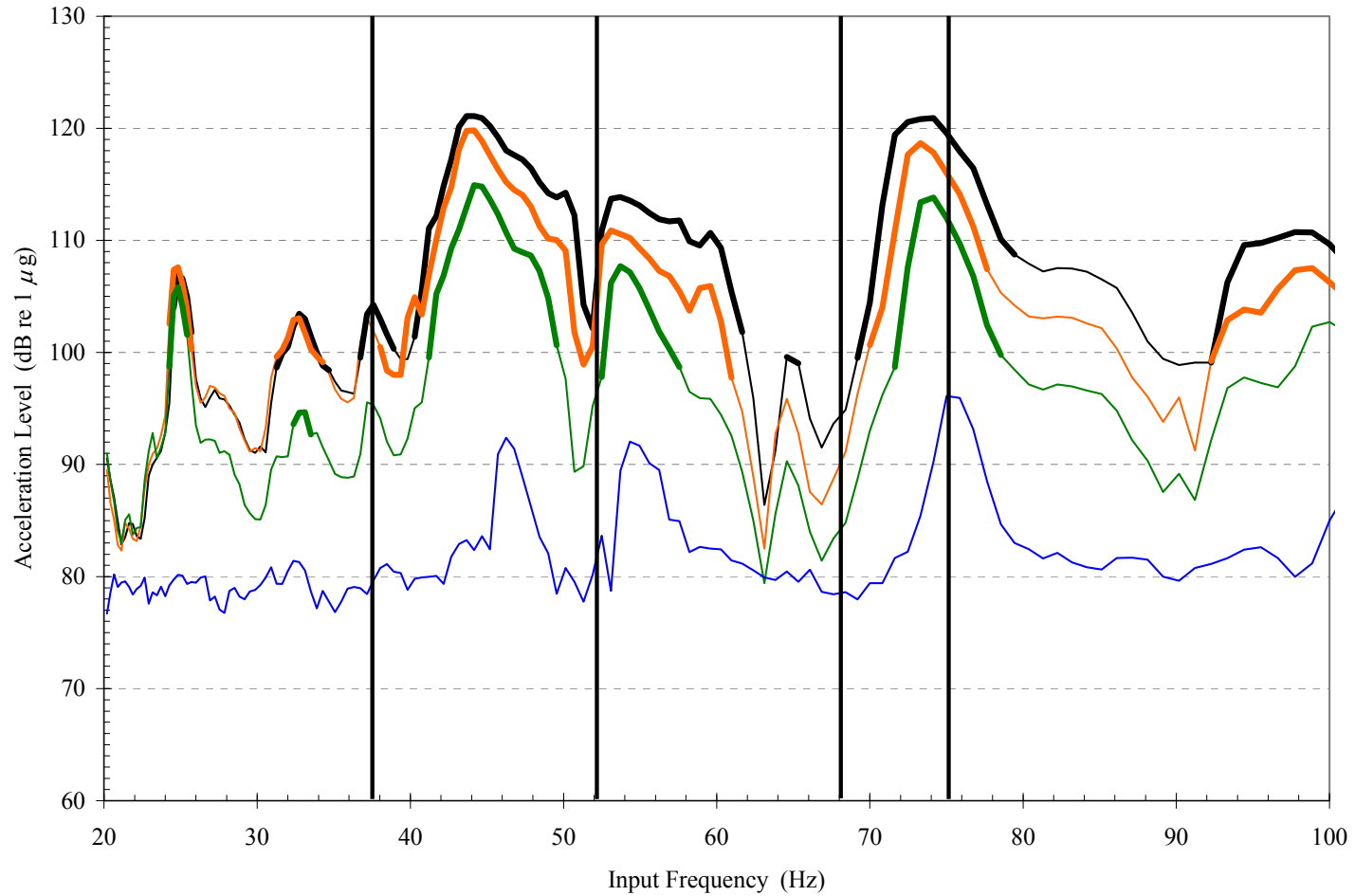


Figure B.2: Response of the lower west window to four swept sine signal strengths; 70 dBC blue, 80 dBC green, 90 dBC orange, 100 dBC black. Bolded line-style indicates input frequencies at which rattle occurred.

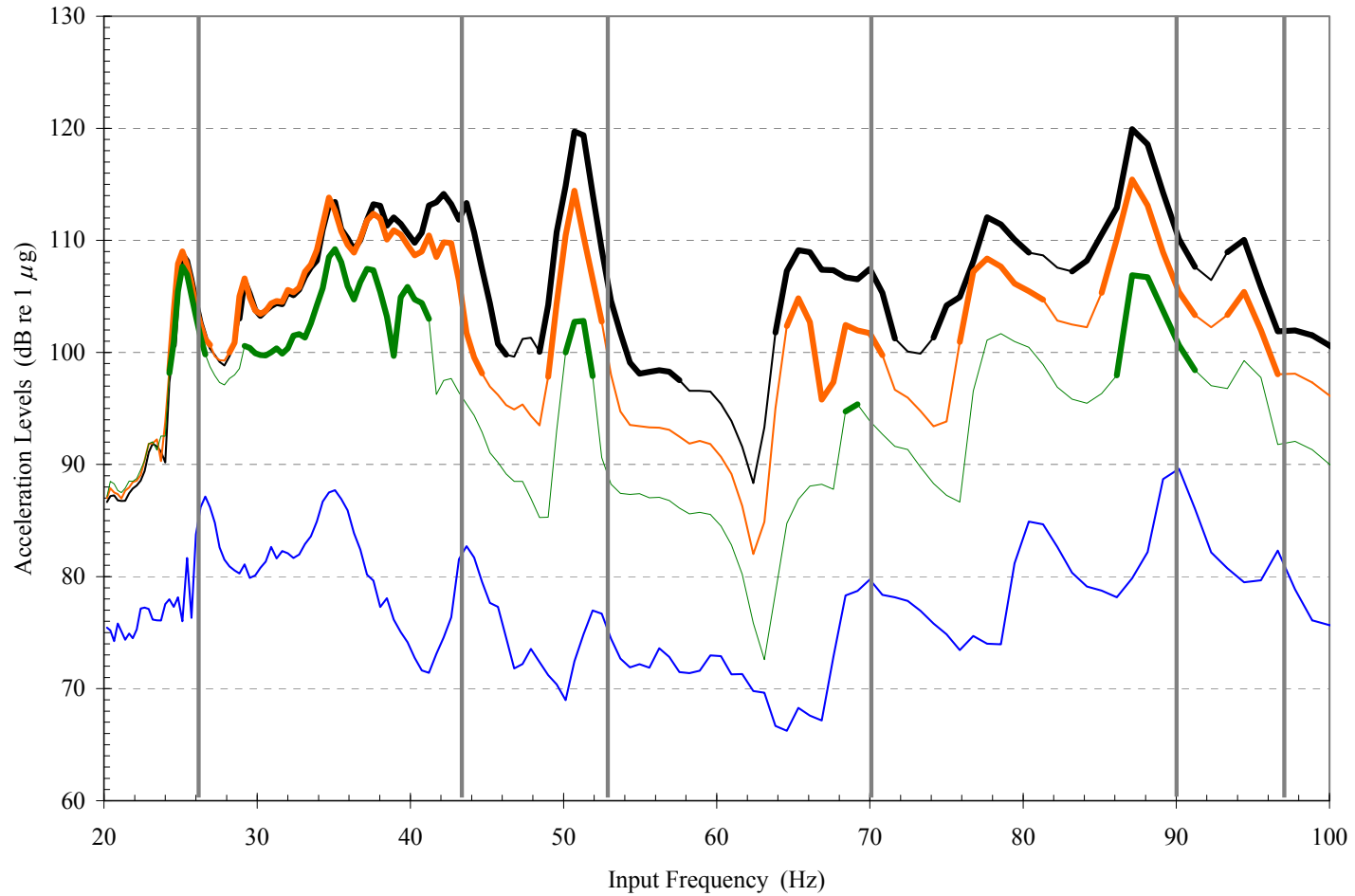


Figure B.3: Response of the upper east window to four swept sine signal strengths; 70 dBC blue, 80 dBC green, 90 dBC orange, 100 dBC black. Bolded line-style indicates input frequencies at which rattle occurred.

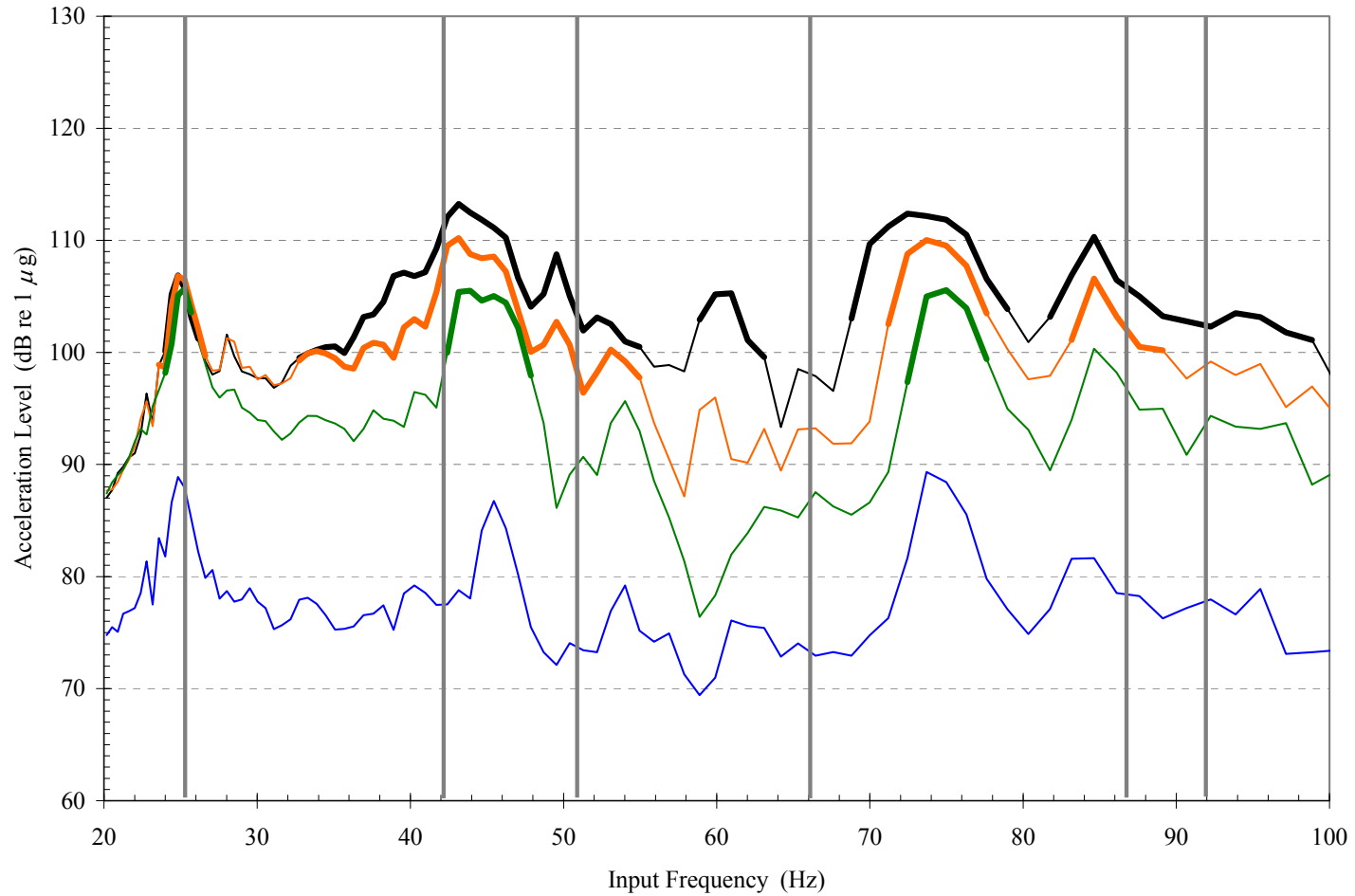


Figure B.4: Response of the upper west window to four swept sine signal strengths; 70 dBC blue, 80 dBC green, 90 dBC orange, 100 dBC black. Bolded line-style indicates input frequencies at which rattle occurred.